Structural and Magnetic Properties of Epitaxial MnSi(111) Thin Films

by

Eric A. Karhu

Submitted in partial fulfilment of the requirements
for the degree of Doctor of Philosophy

at

Dalhousie University
Halifax, Nova Scotia
January 2012

DALHOUSIE UNIVERSITY

DEPARTMENT OF PHYSICS AND ATMOSPHERIC SCIENCE

The undersigned hereby certify that they have read and recommend to the Faculty of Graduate Studies for acceptance a thesis entitled "Structural and Magnetic Properties of Epitaxial MnSi(111) Thin Films" by Eric A. Karhu in partial fulfilment of the requirements for the degree of Doctor of Philosophy.

Dated: January 12, 2012

External Examiner: _____

Research Co-Supervisors: _____

_____

Examining Committee: _____

_____

Departmental Representative: _____

DALHOUSIE UNIVERSITY

DATE: January 12, 2012

AUTHOR: Eric A. Karhu

TITLE: Structural and Magnetic Properties of Epitaxial MnSi(111) Thin Films

DEPARTMENT OR SCHOOL: Department of Physics and Atmospheric Science

DEGREE: PhD CONVOCATION: May YEAR: 2012

_____

Signature of Author

For Äiti and Pappa

Table of Contents

List of Tables

List of Figures

Abstract

MnSi(111) films were grown on Si(111) substrates by solid phase epitaxy (SPE) and molecular beam epitaxy (MBE) to determine their magnetic structures. A lattice mismatch of -3.1% causes an in-plane tensile strain in the film, which is partially relaxed by misfit dislocations. A correlation between the thickness dependence of the Curie temperature (T_C) and strain is hypothesized to be due to the presence of interstitial defects. The in-plane tensile strain leads to an increase in the unit cell volume that results in an increased T_C as large as $T_C = 45$ K compared to $T_C = 29.5$ K for bulk MnSi crystals.

The epitaxially induced tensile stress in the MnSi thin films creates an easy-plane uniaxial anisotropy. The magnetoelastic coefficient was obtained from superconducting quantum interference device (SQUID) magnetometry measurements combined with transmission electron microscopy (TEM) and x-ray diffraction (XRD) data. The experimental value agrees with the coefficient determined from density functional calculations, which supports the conclusion that the uniaxial anisotropy originates from the magnetoelastic coupling.

Interfacial roughness obscured the magnetic structure of the SPE films, which motivated the search for a better method of film growth. MBE grown films displayed much lower interfacial roughness that enabled a determination of the magnetic structure using SQUID and polarized neutron reflectometry (PNR). Out-of-plane magnetic field measurements on MBE grown MnSi(111) thin films on Si(111) substrates show the formation of a helical conical phase with a wavelength of $2\pi/Q = 13.9 \pm 0.1$ nm. The presence of both left-handed and right-handed magnetic chiralities is found to be due to the existence of inversion domains that result from the non-centrosymmetric crystal structure of MnSi. The magnetic frustration created at the domain boundaries explains an observed glassy behaviour in the magnetic response of the films.

PNR and SQUID measurements of MnSi thin films performed in an in-plane magnetic field show a complex magnetic behaviour. Experimental results combined with theoretical results obtained from a Dzyaloshinskii model with an added easy-plane uniaxial anisotropy reveals the existence of numerous magnetic modulated states that do not exist in bulk MnSi. It is demonstrated in this thesis that modulated chiral magnetic states can be investigated with epitaxially grown MnSi(111) thin films on insulating Si substrates, which offers opportunities to investigate spin-dependent transport in chiral magnetic heterostructures based on this system.

List of Abbreviations and Symbols Used

A – spin wave stiffness

a^3 – unit cell volume

$\hat{a}$, $\hat{b}$, and $\hat{c} = \hat{a} \times \hat{b}$ – perpendicular unit vectors describing coordinate frame of helix

AE – anisotropic exchange

AES – Auger electron spectroscopy

AFM – atomic force microscope

a_{MnSi} , a_{Si} – lattice parameters for MnSi and Si

a_{t} – transformation matrix

b – nuclear scattering length

B_1 – magnetoelastic stress coefficient

B_2 – magnetoelastic shear stress coefficient

$\vec{B}_{eff}$ – effective magnetic flux density

c_{11} – coefficient of stiffness resisting strain by stress in same direction

c_{12} – coefficient of stiffness resisting strain by stress in orthogonal direction

c_{44} – coefficient of shear stiffness

c_{ij} – reduced elastic stiffness tensor

c_{ijkl} – elastic stiffness tensor ,

d, d_{Mn} , d_{film} , d_{bulk} – thickness

D_0 – Dzyaloshinskii constant

D_1 – magnetoelastic stress coefficient

D_2 – magnetoelastic shear stress coefficient

D_{XRD} – x-ray detector

DFT – Density functional theory

DM – Dzyaloshinskii-Moriya

DOF – degrees of freedom

e – electron charge

$\vec{E}$ – electric field vector

EELS – electron energy loss spectroscopy

E_g – the effective spin-wave gap

E_S – kinetic energy

F – anisotropic exchange constant

f – scaling factor

f' , f'' – real and imaginary parts of the x-ray scattering factor

F_h – structure factor

FMR – ferromagnetic resonance

f.u. – formula unit

GMR – giant magneto-resistance

g – electron g-factor

g_n – nuclear Landé factor

g_{ref} – inverse distance between the (000) spot and one of the Si {220} spots

H_{app} – applied field

H_{C1} – critical field between helical and conical phase

H_{C2} – critical field between conical and ferromagnetic phase

H_α, H_β – critical fields in MnSi thin films in an applied transverse field

H_D – saturation field for a bulk cubic helimagnet

H_{Demag} – demagnetizing field

HRTEM – high resolution TEM

$H_{||}$ – parallel component of the applied field H_{app} along the $\hat{c}$ axis

$\hbar$ – Planck constant/2π

I – intensity

K_0 – effective stiffness due to competition between DM and direct exchange interactions

$K_{1,eff} - SFQ^2 / g\mu_B a^3$

k, k_{in}, k_r, k_{tr}, – k-vector, incident k-vector, reflected k-vector, transmitted k-vector

k^+, k^- – up-spin and down-spin neutron k-vectors, respectively

$$k_0 = \left|\vec{k}_{in}\right| = \left|\vec{k}_r\right| = \left|\vec{k}_{tr}\right| / n_1$$

$$k_1 = \left|\vec{k}_{tr}\right|$$

K_m – stray field term

K_u – uniaxial anisotropic constant

L – cubic invariant

LEED – low energy electron diffraction

M – magnetization magnitude

$\vec{M}$ – magnetization vector

$\hat{m}$ – unit vector along direction of magnetization

MBE – molecular beam epitaxy

MCA – magnetocrystalline anisotropy

ML – monolayer

M_r – remanent magnetization

M_{sat} – saturation magnetization

M_T – scaling factor

M_{XRD} - monochromator

m_0 – magnetic moment

m_e – electron mass

m_n – neutron mass

n – integer number

n_0, n_1 – index of refraction

$\hat{n}$ – unit vector indicating direction of uniaxial anisotropy

p_c – critical pressure

PES – photoemission spectroscopy

PNR – polarized neutron reflectivity

$\vec{Q}$ – propagation vector

Q – magnitude of propagation vector

q, q_c, q_z – scattering vector, critical scattering vector, z-component of scattering vector

QL – quadlayer

R – reflectivity

r – reflected amplitude

R(+ +), R(− −) – non-spin-flip reflectivities

R(+ –), R(− +) – spin-flip reflectivities

r_e – Thomson scattering length

RHEED – reflection high energy electron diffraction

r_{icc} – interface correlation coefficient

r_S – distance from origin

RT – room temperature

S – unit cell spin

$\vec{S}$ – spin

$S1$ – $S5$ – x-ray diffractometer slits

SADP – selected area diffraction pattern

SLD – scattering length density

S_M – magnetic viscosity

SPE – solid phase epitaxy

SQUID – superconducting quantum interference device

STM – scanning tunnelling microscopy

STT – spin transfer torque

S_{XRD} – x-ray source

T – temperature

t – transmitted amplitude

T_C – Curie temperature

T_C (n) – Curie temperature as a function of the number of monolayers

T_C (∞) – Curie temperature at the thick film limit

TEM – transmission electron microscope

T_{min} – minimum temperature

T_{max} – temperature where broadening in the $M(T)$ data curve due to finite size observed.

TRM – thermoremanent magnetization

u_{Mn}, u_{Si} – basis vector parameters for Mn and Si atoms

UHV – ultra-high vacuum

V – volume

V_S – potential energy

w_{ae} – anisotropic exchange energy density

w_{dm} - Dzyaloshinskii-Moriya interaction energy density

w_{el} – elastic energy density

w_{ex} – ferromagnetic exchange energy density

w_{me} – magnetoelastic energy density

w_{tot} – total energy density

w_{uni} – uniaxial MCA energy density

w_Z – Zeeman energy density

XPS – x-ray photoelectron spectroscopy

XRR – x-ray reflectometry

XRD – x-ray diffraction

α – cone angle, angle of magnetic moment with respect to the a–b plane

α_k, where $k = 1,2,3$ – directional cosines

β – critical exponent

Δg – inverse distance between fine structure's center spot and outer ring of spots

$\varepsilon_1', \varepsilon_2', \varepsilon_{\|}$ – in-plane strains

ε_3' $\varepsilon_{\perp}$ – out-of-plane strain

$\varepsilon_{ij}, \varepsilon_{kl}, \varepsilon_i, \varepsilon_j$ – symmetric strain tensors

ϕ – azimuthal angle

θ – angle between $\boldsymbol{H}_{\text{app}}$ and $\vec{Q}$,

θ_{A} – polar angle

θ_0 – angle of incidence

θ_1 – angle of refraction

θ_c – critical angle

κ – bulk modulus

λ – wavelength

μ_0 – permeability of free space

μ_1 – amplitude of 14-nm harmonic of the spin density wave

μ_2 – amplitude of second harmonic of the spin density wave

μ_{B} – Bohr magneton

μ_{bulk} – moment of bulk MnSi

μ_n – nuclear magneton

ρ – scattering length density

ρ_{r} – resistivity

ρ_m – molecular number density of the material

ρ_e – electron density

σ – standard deviation

σ_P – Pauli spin matrices

σ_{R} – interface roughness

σ_{L}, σ_{H} – interface roughness, lower boundary and upper boundary respectively

τ_{w} – wait time

τ – time

φ – angle between magnetization vector and axis of anisotropy

χ_{HF} – high-field susceptibility

ψ – angle of magnetization with respect to film normal

ψ_S – wave function

Ω – sample alignment angle

Acknowledgements

I would like to thank my supervisor Prof. Theodore L. Monchesky for all his help and support for allowing me to present this work. I would also like to thank my co-supervisor Prof. Michael D. Robertson (Acadia University) for his help and for allowing me to accompany him to McMaster University to observe HRTEM imaging performed on the MnSi thin film samples. I would like to thank Dr. Christian Maunders at McMaster University for the HRTEM imaging of the MnSi films. I would also like to thank my advisory committee: Prof. Richard A. Dunlap, Prof. Kevin C. Hewitt and Prof. Michael D. Robertson. In addition, I would like to thank my colleagues, Samer Kahwaji and Zeynel Bayindir, for their assistance in the lab, Prof. Manfred H. Jericho for the AFM images, and Prof. Michael D. Robertson and his students, Krista Raffel, Emily Machan, Cathryn Parsons and Matthew Bluteau, for all their hard work imaging the MnSi thin film samples with TEM and their analysis of the images. I would like to thank Dr. Helmut Fritzsche at the National Research Council Canada Canadian Neutron Beam Centre, Dr. Brian J. Kirby and Dr. Charles F. Majkrzak at the NIST Center for Neutron Research for their help with the PNR study. I also want to thank Dr. U. K. Rößler and Prof. A. N. Bogdanov at the Leibniz Institute for Solid State and Materials Research for their theoretical input and thank Andy George and Kevin Borjel for their help in building and fixing the various pieces of equipment needed to keep the experiments running.

Chapter 1 – Introduction

Magnetic thin film research has been instrumental in advancing the emerging field of spintronics, which uses the spin as well as the charge of an electron to manipulate and transmit information. The field of spintronics began with the discovery of giant magnetoresistance (GMR) by Grünberg *et al*. [1] and independently by Fert *et al*. [2]. Both research groups were investigating magnetic multilayer structures consisting of Fe and Cr and observed changes in electrical resistance dependent on the magnetic alignment of adjacent ferromagnetic layers. When the spins in the ferromagnetic layers were aligned parallel to each other, a low resistance was measured, and when the spins were aligned anti-parallel, a high resistance was observed.

Electrical currents have also been shown to change the magnetic structure of a material. This process, which is complementary to GMR, is known as spin transfer torque (STT). STT experiments are conducted with the current perpendicular to a magnetic trilayer structure that consists of two ferromagnetic layers separated by a non-magnetic spacer layer. The exchange splitting in a ferromagnet creates a difference in the density of states at the Fermi level of a ferromagnetic material. It is these electrons that are important for conduction, and since they are spin-polarized, so is the current. As current flows from one ferromagnetic layer, through a spacer layer, and into a second ferromagnetic layer, the angular momentum is transferred to the second layer by the spin-polarized current. If the current polarization is not parallel to the second layer's magnetization, the current will exert a torque on the magnetization, transfer its angular momentum and cause a precession or switching of this layer [3, 4].

Combinations of thin film structures consisting of ferromagnetic, antiferromagnetic and/or non-magnetic materials have resulted in the observation of domain wall movement by electric current [5], current induced switching of domains in multilayer devices [6] and spin valve switching [7]. Spin valves consist of two magnetic layers separated by a non-magnetic conductor. The magnetic layers are either uncoupled or weakly coupled with one of the layers being magnetically soft and the other layer magnetically hard. By introducing an external field to the system, a change in the angle between the moments of the two magnetic layers can be observed [8]. Grollier *et al*. studied the domain wall movement in a spin valve structure of Co/Cu/Permalloy and observed spin valve switching due to current-induced domain wall motion. When the current was reversed in zero-field, the domain wall movement also reversed direction [7]. Spin transfer torque has been shown to induce the reversal of magnetic structures by precession, with fast switching times (less then 1 nanosecond), which are predicted to be useful in magnetic memory devices or high speed signal processing [9]. Magnetic heterostructures consisting of multiple layers have also been shown to behave like a nanoscale motor [10]. Magnetic motors were shown to convert energy generated by a direct current into high frequency magnetic rotations that were predicted to be useful as microwave generators and resonators [10]. Although the majority of magnetic thin film research has been performed using collinear magnetic structures, there has been a growing interest in the study of non-collinear magnetic structures including helical magnetic structures, which provide new opportunities in the field of spintronics.

MnSi has a helical magnetic structure and there are a number of predictions for spin-dependent electron transport in helical magnetic thin film heterostructures. The

study of the relationship between spiral magnetic order and dissipationless spin transport demonstrated the possibility of dissipationless spin currents [11]. Spin-transfer-torque-induced rotation of the helical order parameter has also been predicted in bulk metals with a helical spin density wave [12]. A helical magnetic structure consists of a series of planes of spins, where the spins in each layer align ferromagnetically with all other spins in that plane, while consecutive planes assemble to create a spiral along a direction given by the propagation vector $\vec{Q}$, where, $\hat{a}$, $\hat{b}$, and $\hat{c} = \hat{a} \times \hat{b}$ are perpendicular unit vectors that describe the coordinate frame of the helix ($\hat{c}$ is parallel to the propagation vector $\vec{Q}$), as shown in Fig.1.1. The wavelength of the helical modulation is $2\pi / Q$. The STT

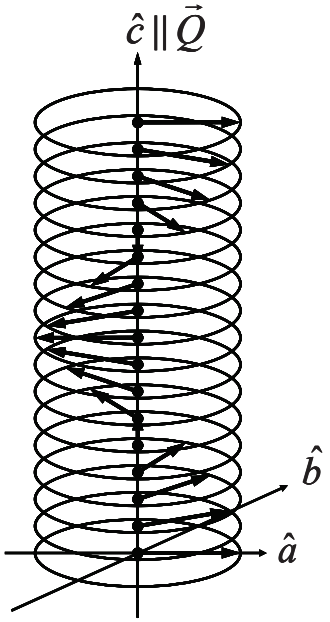

Figure 1.1. Helical phase in zero-field with the propagation vector $\vec{Q}$ parallel to the $\hat{c}$ - axis parallel.

induced in a helical structure is a bulk effect that rotates the entire helix about the pitch axis [13]. A rigid rotation of the helix is predicted above a critical current and a current driven oscillator with the velocity of helix rotation dependent on the magnitude of the current flow and the magnetic anisotropy is one example of an application of STT in a helical magnetic structure [13].

Jonietz *et al*. have also recently demonstrated spin-transfer torque in bulk MnSi crystals in the skyrmion phase [14]. Skyrmions are stable topological magnetic textures described as a magnetic vortex in which the directions of the magnetic moments in the skyrmion cover 4π steradians and the magnetization at the centre of the vortex is twisted anti-parallel to the edges of the vortex [15]. The direct observation of a skyrmion lattice, which can be described as consisting of a series of "stable magnetic knots" [15], has been observed in $Fe_{0.5}Co_{0.5}Si$ [16] and in bulk MnSi [17 – 19]. Heterostructures based on MnSi thin films therefore provide a system that can be used to search for these effects and explore some of the theoretical predictions mentioned above.

1.1 Bulk MnSi

Bulk MnSi has a B20 crystal structure with a lattice parameter of $a_{MnSi} = 0.4561$ nm at room temperature (RT) [20]. A B20 crystal structure can be described as a distorted cubic rock salt structure consisting of two sets of basis vectors, (u, u, u), (1/2 + u, 1/2 - u, -u), (-u, 1/2 + u, 1/2 - u), and (1/2 - u, -u, 1/2 + u), where $u_{Mn} = 0.137$ and $u_{Si} = 0.845$ [21] and there is no inversion symmetry present in the crystal. An inversion symmetry operation transforms the basis vectors given above into

(-u, -u, -u), (1/2 - u, 1/2 + u, u), (u, 1/2 - u, 1/2 + u), and (1/2 + u, u, 1/2 - u), and creates a crystal that is a mirror image of the former crystal. A lattice with $u_{\mathrm{Mn}} = 0.137$ and $u_{\mathrm{Si}} = 0.845$ is referred to as a right-handed helix, while $u_{\mathrm{Mn}} = 1 - 0.137 = 0.863$ and $u_{\mathrm{Si}} = 1 - 0.845 = 0.155$ defines a left-handed helix. A ball and stick representation of the clockwise rotation of a right-handed helix and the counter-clockwise rotation of a left-handed helix are shown in Fig. 1.2 (a) and (b), respectively. The B20 structure shown in Fig. 1.2 (c) and (d) consists of alternating layers of Mn and Si atoms that repeat every 12 layers. Four layer sections (quadlayers) are organized in an *ABCABCABC*... sequence, the same sequence as a face-centered cubic structure [22]. Each quadlayer (QL) consists of a layer with a high density of Mn (dense), a layer with a low density of Si (sparse), followed by a sparse Mn layer and a dense Si layer with the high density and low density layers having three and one atom per unit cell of MnSi(111), respectively, as shown in Fig. 1.2 (c) and (d) [23, 24].

MnSi is a weak itinerant ferromagnet with a moment $\mu_{\mathrm{bulk}} = 0.39\ \mu_{\mathrm{B}}$/Mn below the Curie temperature $T_{\mathrm{C}} = 29.5$K, where μ_{B} is the Bohr magneton [25]. There are 4 Mn atoms per unit cell and the unit cell spin S is,

$$S = (4\ \mathrm{Mn}\ /\ \mathrm{cell}) \times (0.39 \mu_{\mathrm{B}}/\mathrm{Mn}) \times (0.5\hbar/\mu_{\mathrm{B}}) \approx 0.8\hbar/\mathrm{cell}. \qquad (1.1)$$

MnSi is sensitive to both applied magnetic fields [26] and pressure [27, 28]. At ambient pressure, neutron scattering experiments on bulk MnSi have shown that in zero-field the magnetic structure in bulk MnSi consists of four left-handed helical domains oriented along the four <111> cube diagonals [29, 30]. At temperatures well below T_{C} and in an applied field H_{app} oriented parallel to the [111] direction, both neutron scattering

[28 – 31] and susceptibility measurements [32] determined that the applied external field

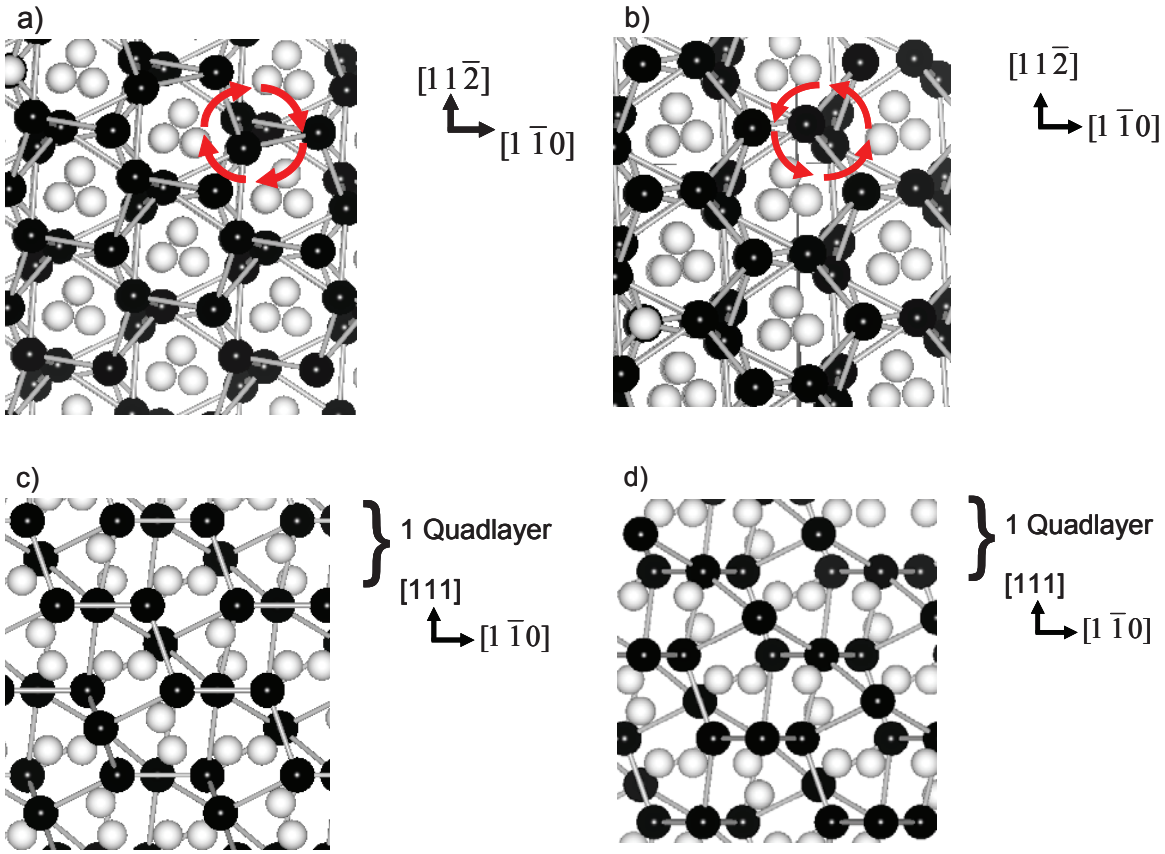

Figure 1.2. Ball and stick model for MnSi. The white balls and black balls represent Si and Mn, respectively. A right-handed helix is shown in a) and c) with position coordinates u_{Mn} = 0.137 and u_{Si} = 0.845. By looking into the page of Fig. 1.2 (a), one can see the Mn atoms in consecutive planes stack with a right-handed twist, as shown by the arrows. b) and d) show a left-handed helix with position coordinates u_{Mn} = 0.863 and u_{Si} = 0.155. A perpendicular side view of a MnSi(111) thin film c) and d) shows the B20 MnSi quadlayer structure.

aligns the domains along the field direction at $H_{C1} \approx 0.1$ T, above which a conical phase forms. When H_{app} is not parallel to the propagation vector $\vec{Q}$, $\vec{Q}$ rotates in the field direction. The conical spin density wave can be described by:

$$\hat{m}(\vec{r}) = \hat{c}\sin(\alpha) + \hat{a}\cos(\vec{Q}\cdot\vec{r}) + \hat{b}\sin(\vec{Q}\cdot\vec{r}), \tag{1.2}$$

where, $\hat{a}$, $\hat{b}$, and $\hat{c}$ are defined on p. 3 and the cone angle α is the angle of the moments with respect to the *a*-*b* plane, as shown in Fig. 1.3. The cone angle α, continues to increase with increasing field up to a critical field $H_{C2} \approx 0.6$ T, above which a field-induced ferromagnetic state appears [29, 31]. The helical wavelength $2\pi/Q$ = 18 nm remains largely unchanged over this range of fields [29, 31] and a skyrmion phase has also been identified at temperatures just below T_C [17 – 19, 33]. A magnetic phase diagram of bulk MnSi at ambient pressure is shown in Fig. 1.4 [33].

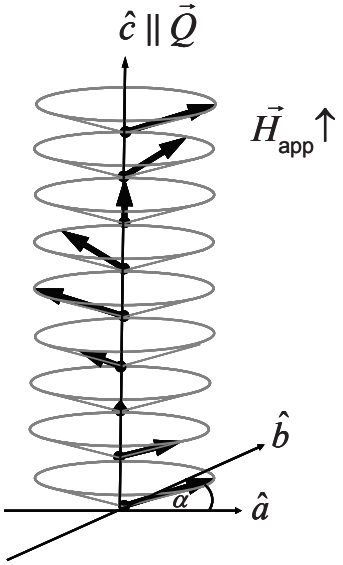

Figure 1.3. Conical phase due to an external field, $\vec{H}_{app}$, applied along the $\hat{c}$-axis.

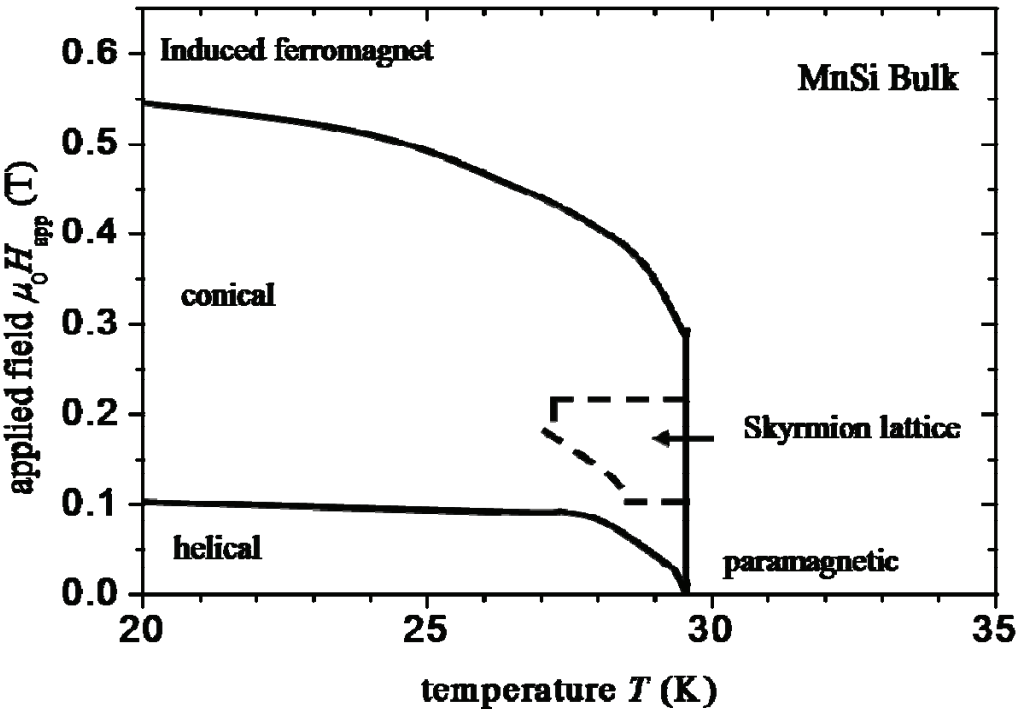

Figure 1.4. Magnetic phase diagram of bulk MnSi. At low temperatures, three phases are observed and below 0.1 T, a helical phase exists. Between 0.1 – 0.6 T, the moments are canted in the direction of the field forming a conical phase. Above 0.6 T, there is field induced ferromagnetic order. Just below T_C a skyrmion lattice can exist over a narrow range of applied field (adapted from Ref. [33]).

Plumer and Walker [34] used mean field theory to show how magnetic anisotropy and an external magnetic field affect the rotation of the propagation vector $\vec{Q}$ in an applied magnetic field. In the <100> or <110> directions, the reorientation of Q, which occurs with a second-order-like transition, creates a small deviation from a linear

behaviour below $H_{C1} \simeq 0.15$ T in the $M-H$ loop [25, 34, 35]. Although the model used by Plumer and Walker fits well with Hansen's experimental data [36] on bulk MnSi, it does not fit the thin film data presented in Chapter 4.

The helical magnetic structure of bulk MnSi is due to a hierarchy of interactions [34, 37, 38]. The dominant ferromagnetic exchange energy density,

$$w_{ex} = -\frac{AS}{2M_{\text{sat}}^2 a^3}\vec{M}\cdot\nabla^2\vec{M}, \tag{1.3}$$

where A is the spin wave stiffness, a^3 is the unit cell volume, $\vec{M}$ is the magnetization vector, $M_{\text{sat}} = \left|\vec{M}\right| = Sg\mu_B / a^3$ is the saturation magnetization and $g = 1.95$ is the g-factor for MnSi [39]. The ferromagnetic order that would be produced by exchange is destabilized by the weaker Dzyaloshinskii-Moriya (DM) interaction,

$$w_{dm} = \frac{SD_0}{M_{\text{sat}}{}^2 a^3}\vec{M}\cdot\left(\nabla\times\vec{M}\right), \tag{1.4}$$

where D_0 is the Dzyaloshinskii constant, and is present due to the lack of inversion symmetry in its crystal structure. For bulk MnSi, $A \simeq 0.50$ meV nm^2 [30, 31, 37] and SD_0 = 0.18 meV nm [40]. At ambient pressure, the competing ferromagnetic exchange and DM interactions produce a helical magnetic ground state with spins oriented perpendicular to a propagation vector $\vec{Q}$. The direction of the helix is determined by a weaker anisotropic exchange (AE) interaction,

$$w_{ae} = \frac{S^2 F Q^2 L}{4a^3}\cos^2\alpha, \tag{1.5}$$

where F is a constant that in bulk MnSi equals 0.11 meV nm^2 [40]. The cubic invariant, $L = \sum_{i=1}^{3}\hat{c}_i^2\left(\hat{a}_i^2 + \hat{b}_i^2\right)$, describes the anisotropy. L = 0, 1/2 and 2/3 when $\vec{Q}$ points along the

<100>, <110> and <111> directions, respectively. The AE interaction orients the helical magnetic ground state along the <111> directions when $F < 0$, as is the case for MnSi, and along <100> when $F > 0$. Fig. 1.5 shows a three dimensional plot of the anisotropic exchange energy as a function of polar and azimuthal angles.

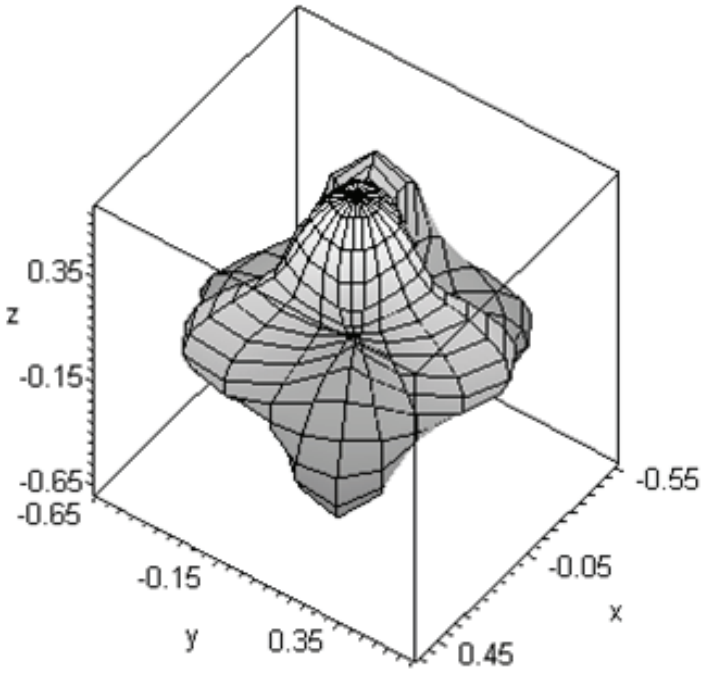

Figure 1.5. Anisotropic exchange energy as a function of direction for F < 0.

The wavelength of the propagation vector can be determined by inserting Eq. (1.2) into $w_{ex} + w_{dm} + w_{ae}$, which gives the total energy density,

$$w_{tot} = \frac{1}{a^3}\left(\frac{SAQ^2}{2} - S^2 D_0 Q + \frac{S^2 F Q^2 L}{4}\right)\cos^2\alpha\,. \tag{1.6}$$

By minimizing the total energy density with respect to Q, one obtains:

$$\frac{dw_{tot}}{dQ} = SAQ - S^2 D_0 + \frac{S^2 FQL}{2} = 0, \tag{1.7}$$

and

$$Q = \frac{SD_0}{A + \frac{SFL}{2}}, \tag{1.8}$$

where $Q \approx 0.35$ nm^{-1} for bulk MnSi crystal.

The Zeeman energy density $w_z = -\mu_0 M_{sat} \cdot H_{app}$ for a helix in a magnetic field, H_{app} is given by

$$w_z = -\mu_0 M_{sat} H_{||} \sin\alpha, \tag{1.9}$$

where $H_{||}$ is the component of the applied field H_{app} parallel to the $\hat{c}$-axis. In the case of MnSi, $w_{tot} = w_{ex} + w_{dm} + w_{ae} + w_z$ as a function of the cone-angle is [38],

$$w_{tot} = \frac{1}{a^3}\left(\frac{SAQ^2}{2} - S^2 D_0 Q + \frac{S^2 FQ^2 L}{4}\right)\cos^2\alpha - \mu_0 M_{sat} H_{||} \sin\alpha . \tag{1.10}$$

Minimizing Eq. (1.10) with respect to Q gives the pitch of the helix, assuming that Q is independent of H.

The critical field H_{C2}, is determined by minimizing Eq. (1.10) with respect to the cone angle α. When the applied field is along the [111] direction, which gives

$$\mu_0 H_{app} = \frac{\sin\alpha}{M_{sat}}\left(SAQ^2 + \frac{S^2 FQ^2 L}{2} - 2S^2 D_0 Q\right). \tag{1.11}$$

By substituting Eq. (1.8) into Eq. (1.11), one obtains,

$$\mu_0 H_{C2} = \frac{-H_{app}}{\sin\alpha} = \frac{S}{M_{sat}}\left(AQ^2 + \frac{SFQ^2}{3}\right). \tag{1.12}$$

When H_{app} is not parallel to [111], minimizing Eq. (1.10) with respect to α gives,

$$\mu_0 H_{C2} = \frac{-H_{app}\cos\theta}{\sin\alpha} = \frac{S}{M_{sat}}\left(AQ^2 + \frac{SFQ^2L(\theta)}{2}\right). \tag{1.13}$$

where θ is the angle between $\vec{Q}$ and [111].

Recently there has also been interest in exploring the sensitivity of bulk MnSi with respect to applied pressure. At ambient pressures, MnSi is well described by Fermi liquid theory, which predicts a $\rho_r \propto T^2$ dependence, where ρ_r is the resistivity and T is the temperature. However, under hydrostatic pressure, the Curie temperature T_C decreases with increasing pressure up to a critical pressure of p_c = 1.46 GPa and above this critical pressure long-range magnetic order disappears [41]. Just above p_c, the direction of the helix changes from the [111] orientation to the [110] direction and partial magnetic order is observed [27, 42]. The onset of partial magnetic order coincides with non-Fermi liquid behaviour in which the resistivity varies as $T^{3/2}$, and recent experiments suggest that the non-Fermi liquid behaviour may indicate the existence of a skyrmion lattice [17–19, 33].

1.2 Thin Film MnSi

Although a great deal of research has been performed on the magnetic and pressure dependence of bulk MnSi, the magnetic properties of MnSi thin films are largely unexplored, which is part of the motivation behind this thesis. Thin film helical magnets on insulating substrates serve as the starting point for creating ferromagnet-helical magnet heterostructures in order to explore spin-dependent transport in chiral systems. In addition, other non-collinear magnetic structures such as skyrmions are sensitive to strain and anisotropy. Molecular beam epitaxy (MBE) provides a way to control these

parameters and stabilize the skyrmion phase. While Pfleiderer has demonstrated STT in bulk in the skyrmion phase [14], it is more desirable to investigate this in thin films where measurements can be performed on both the helical and skyrmion phases, and currents can be more easily controlled with appropriate engineering of the films. MnSi is a good candidate because of the extensive characterization in bulk, and it has been shown that MnSi grows well on Si(111), an ideal substrate for electron transport studies [24, 43 – 51].

In order to grow epitaxial MnSi thin films, a suitable substrate with a lattice constant similar to that of MnSi was found. Although Si(111) is a good substrate for growth of epitaxial MnSi thin films, and a number of research groups have previously detailed the growth of MnSi on Si [24, 43 – 51], little research has been performed on the magnetic properties of MnSi thin films [52, 53]. The Si(111) substrate with a lattice parameter of a_{Si} = 0.5431 nm, has a lattice mismatch between MnSi(111) and Si(111) that is $[a_{MnSi} - a_{Si}\cos(30^{o})]/a_{MnSi}$ = -3.1% for an epitaxial relationship $MnSi[1\bar{1}0]||Si[11\bar{2}]$ [46], as shown in Fig. 1.6. This lattice mismatch induces an in-plane tensile strain in the film. Uniaxial strain is predicted to stabilize the skyrmion phase [54], which offers an opportunity to increase the temperature range over which this phase is stable by engineering the structure with MBE. Epitaxial induced tensile strain in MnSi thin films provides a means to investigate pressure-induced changes in the magnetic structure, since pressure-induced changes to the lattice constant of only a few tenths of a percent were sufficient to create new magnetic phases in bulk MnSi and ultimately destroy the magnetic order [27]. Finite-size effects can also cause changes in the magnetic structure in thin-film MnSi heterostructures [55]. In addition, Si provides an

insulating substrate for future transport studies. Furthermore, I have shown in this thesis that the propagation vector in zero magnetic field points along the surface normal with the magnetic moment in the plane of the film, which is the ideal geometry for STT experiments.

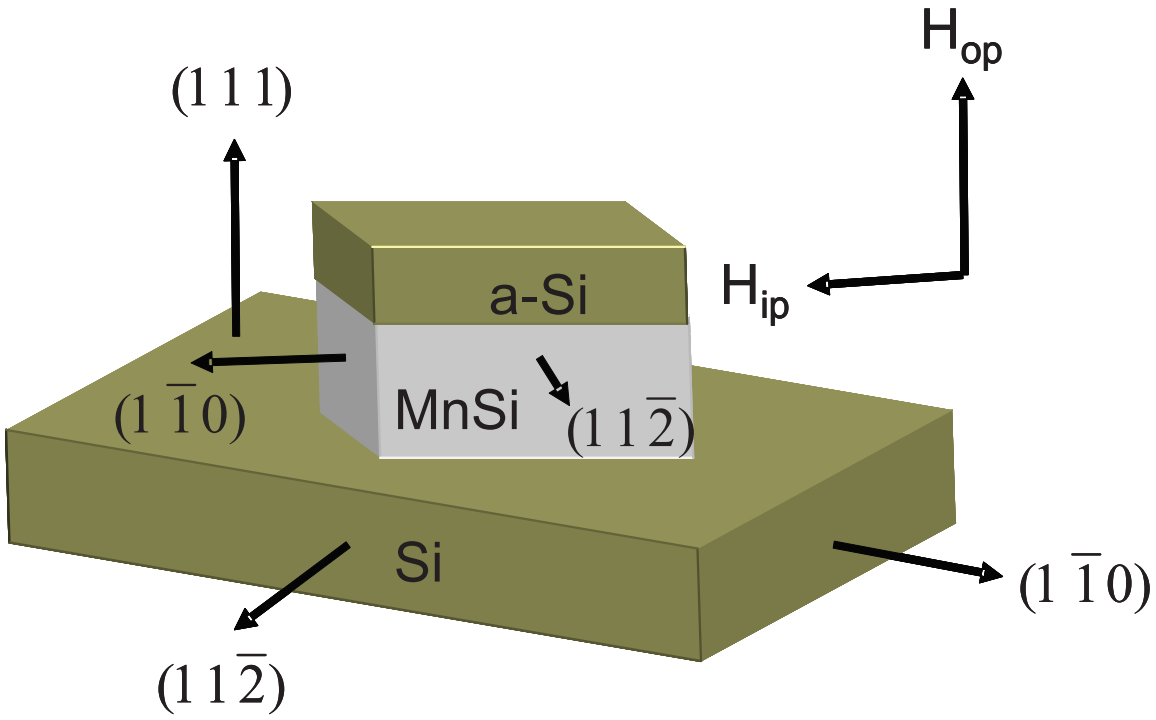

Figure 1.6. A diagram of the epitaxial relationship $MnSi[1\bar{1}0]\|Si[11\bar{2}]$ for MnSi(111) on a Si(111) substrate [46]. The lattice mismatch for this geometry is -3.1%.

In ferromagnetic materials, in the absence of an external magnetic field, the magnetization vector orients itself along certain crystallographic directions known as "easy" directions. Magnetocrystalline anisotropy (MCA) is the energy required to rotate the magnetization from the "easy" direction into the "hard" direction and is due to spin-

orbit coupling. For thin films, the broken symmetry at the interfaces and epitaxially induced strain can create a uniaxial anisotropy in a cubic magnet [8, 56].

The uniaxial MCA energy density is expressed as,

$$E_{uni} = K_u \cos^2 \varphi , \tag{1.14}$$

where K_u is the uniaxial anisotropy constant and φ is an angle between the magnetization vector and the axis of the anisotropy. For $K_u > 0$, the anisotropy is of the easy-plane type, whereas for $K_u < 0$ it is of the easy-axis type.

In the case of MnSi thin films, a uniaxial anisotropy was found with a hard axis along the [111] direction and for a field applied along this axis, φ can be expressed in terms of the cone angle, $\varphi = \frac{\pi}{2} - \alpha$. For thin films, the effect of the demagnetizing field $H_{\text{Demag}} = -M_{\text{sat}} \sin(\alpha)$ (see Appendix A1) also needs to be considered with $Q \| [1\,1\,1]$. The addition of K_u and H_{Demag} changes Eq (1.10) into the following:

$$\begin{aligned} w_{\text{tot}} = {} & \frac{\cos^2 \alpha}{a^3}\left(\frac{SAQ^2}{2} - S^2 D_0 Q + \frac{S^2 F Q^2 L}{4}\right) \\ & + \left(\frac{2K_u}{M_{\text{sat}}} + \frac{\mu_0 M_{\text{sat}}^2}{2}\right)\sin^2 \alpha + \mu_0 M_{\text{sat}} H_{||} \sin \alpha . \end{aligned} \tag{1.15}$$

Following the same procedure as shown for bulk MnSi, the field dependence of the cone angle α in the presence of the uniaxial anisotropy and demagnetizing energy with stray field in the [111] direction becomes:

$$\mu_0 H_{C2}^{[111]} = \frac{2K_0}{M_{\text{sat}}} + \frac{K_{1,\text{eff}}}{3M_{\text{sat}}} + \frac{2K_u}{M_{\text{sat}}} + \mu_0 M_{\text{sat}} , \tag{1.16}$$

where $K_0 = \frac{1}{2}\frac{AQ^2}{g\mu_B}M_{\mathrm{sat}}$, is the effective stiffness due to the competition between the DM and direct exchange interactions and $K_{1,eff} = \frac{SFQ^2}{g\mu_B a^3}$. In the $[1\,\bar{1}\,0]$ direction [38, 40],

$$\mu_0 H_{C2}^{[1-10]} = \frac{2K_0}{M_{\mathrm{sat}}} + \frac{K_{1,\mathrm{eff}}}{4M_{\mathrm{sat}}} - \frac{K_u}{M_{\mathrm{sat}}} - \frac{K_m}{M_{\mathrm{sat}}} \tag{1.17}$$

where $K_{\mathrm{m}} = \frac{\mu_0 M_{\mathrm{sat}}^2}{2Qd}\left(1-\exp\left(-Qd\right)\right)$ is the stray field contribution (see Appendix A2).

In order to understand the correlation between the mechanical stress and the magnetic anisotropy for the MnSi thin films, the elastic energy density w_{el} for a cubic film is considered,

$$w_{el} = \frac{1}{2}c_{ijkl}\varepsilon_{ij}\varepsilon_{kl}, \tag{1.18}$$

where c_{ijkl} is the elastic stiffness tensor and ε_{ij} and ε_{kl} are the symmetric strain tensors. The high symmetry of the crystal enables a simplification of the elastic stiffness and strain tensors, which are conventionally expressed in the Voigt notation, where the indices in the tensor notation: 11, 22, 33, 23/23, 13/31, 12/21 can be replaced by the Voigt notation: 1, 2, 3, 4, 5, 6, respectively [57]. This simplifies the elastic energy density notation and Eq. (1.18) can be expressed as,

$$w_{el} = \frac{1}{2}c_{ij}\varepsilon_i\varepsilon_j. \tag{1.19}$$

For a cubic crystal structure, only three independent stiffness coefficients are required and the elastic stiffness tensor is reduced to:

$$c_{ij} = \begin{pmatrix} c_{11} & c_{12} & c_{12} & 0 & 0 & 0 \\ c_{12} & c_{11} & c_{12} & 0 & 0 & 0 \\ c_{12} & c_{12} & c_{11} & 0 & 0 & 0 \\ 0 & 0 & 0 & c_{44} & 0 & 0 \\ 0 & 0 & 0 & 0 & c_{44} & 0 \\ 0 & 0 & 0 & 0 & 0 & c_{44} \end{pmatrix} \tag{1.20}$$

and the energy density for a cubic lattice can be written as,

$$w_{el} = \frac{1}{2}c_{11}\left(\varepsilon_1^2 + \varepsilon_2^2 + \varepsilon_3^2\right) + c_{12}\left(\varepsilon_1\varepsilon_2 + \varepsilon_2\varepsilon_3 + \varepsilon_3\varepsilon_1\right) + \frac{1}{2}c_{44}\left(\varepsilon_4^2 + \varepsilon_5^2 + \varepsilon_6^2\right), \tag{1.21}$$

in the basis of the cubic axes. Transformations of the strain tensor from the frame of the cubic axes to the coordinate frame of the film (denoted by a prime) are represented by,

$$\varepsilon_{ij}' = a_t^T \varepsilon_{ij} a_t, \tag{1.22}$$

where a_t is the transformation matrix [57],

$$a_t = \begin{pmatrix} \frac{1}{\sqrt{2}} & \frac{-1}{\sqrt{2}} & 0 \\ \frac{1}{\sqrt{6}} & \frac{1}{\sqrt{6}} & \frac{-2}{\sqrt{6}} \\ \frac{1}{\sqrt{3}} & \frac{1}{\sqrt{3}} & \frac{1}{\sqrt{3}} \end{pmatrix}, \text{ and } a_t^T = \begin{pmatrix} \frac{1}{\sqrt{2}} & \frac{1}{\sqrt{6}} & \frac{1}{\sqrt{3}} \\ \frac{-1}{\sqrt{2}} & \frac{1}{\sqrt{6}} & \frac{1}{\sqrt{3}} \\ 0 & \frac{-2}{\sqrt{6}} & \frac{1}{\sqrt{3}} \end{pmatrix}. \tag{1.23}$$

The relationship between the strains in these two bases is given by,

$$\varepsilon_{ij} = \begin{pmatrix} \frac{1}{2}\varepsilon_1' + \frac{1}{6}\varepsilon_2' + \frac{1}{3}\varepsilon_3' & -\frac{1}{2}\varepsilon_1' + \frac{1}{6}\varepsilon_2' + \frac{1}{3}\varepsilon_3' & \frac{1}{3}\left(-\varepsilon_2' + \varepsilon_3'\right) \\ -\frac{1}{2}\varepsilon_1' + \frac{1}{6}\varepsilon_2' + \frac{1}{3}\varepsilon_3' & \frac{1}{2}\varepsilon_1' + \frac{1}{6}\varepsilon_2' + \frac{1}{3}\varepsilon_3' & \frac{1}{3}\left(-\varepsilon_2' + \varepsilon_3'\right) \\ \frac{1}{3}\left(-\varepsilon_2' + \varepsilon_3'\right) & \frac{1}{3}\left(-\varepsilon_2' + \varepsilon_3'\right) & \frac{2}{3}\varepsilon_2' + \frac{1}{3}\varepsilon_3' \end{pmatrix}, \tag{1.24}$$

where ε_1' and ε_2' are the in-plane strains and ε_3' is the perpendicular strain. Substitution of Eq. (1.24) into Eq. (1.21) gives,

$$w_{el} = \frac{1}{2}c_{11}\left(\left(\frac{1}{2}\varepsilon_1' + \frac{1}{6}\varepsilon_2' + \frac{1}{3}\varepsilon_3'\right)^2 + \left(\frac{1}{2}\varepsilon_1' + \frac{1}{6}\varepsilon_2' + \frac{1}{3}\varepsilon_3'\right)^2 + \left(\frac{2}{3}\varepsilon_2' + \frac{1}{3}\varepsilon_3'\right)^2\right) + c_{12}\left(\left(\frac{1}{2}\varepsilon_1' + \frac{1}{6}\varepsilon_2' + \frac{1}{3}\varepsilon_3'\right)^2 + 2\left(\frac{1}{2}\varepsilon_1' + \frac{1}{6}\varepsilon_2' + \frac{1}{3}\varepsilon_3'\right)\left(\frac{2}{3}\varepsilon_2' + \frac{1}{3}\varepsilon_3'\right)\right) + \frac{1}{2}c_{44}\left(\left(\frac{2}{3}\left(-\varepsilon_2' + \varepsilon_3'\right)\right)^2 + \left(\frac{2}{3}\left(-\varepsilon_2' + \varepsilon_3'\right)\right)^2 + \left(2\left(-\frac{1}{2}\varepsilon_1' + \frac{1}{6}\varepsilon_2' + \frac{1}{3}\varepsilon_3'\right)\right)^2\right). \quad (1.25)$$

By minimizing the energy density with respect to the perpendicular strain ε_3', the ratio of perpendicular strain to in-plane strain is determined for a film in the [111] orientation [57],

$$\frac{\varepsilon_3'}{\varepsilon_1' + \varepsilon_2'} = \frac{\varepsilon_\perp}{2\varepsilon_\parallel} = -\frac{c_{11} + 2c_{12} - 2c_{44}}{c_{11} + 2c_{12} + 4c_{44}}. \quad (1.26)$$

The mechanical strain in a MnSi thin film induced by the substrate affects the magnetic anisotropy of the film. The phenomenological magnetoelastic energy density for a cubic material is described in terms of the direction cosines α_k between the orientation of the magnetization and the crystal axes,

$$w_{me} = B_1\left(\varepsilon_1\alpha_1^2 + \varepsilon_2\alpha_2^2 + \varepsilon_3\alpha_3^2\right) + B_2\left(\varepsilon_4\alpha_2\alpha_3 + \varepsilon_5\alpha_1\alpha_3 + \varepsilon_6\alpha_1\alpha_2\right) + \ldots \quad (1.27)$$

where B_1 is the magnetoelastic stress coefficient and B_2 is the magnetoelastic shear coefficient. This can be expressed in terms of the coordinate frame of a (111) film by substitution of Eq. (1.24) into Eq. (1.27):

$$w_{me} = B_1\left(\left[\frac{1}{2}\varepsilon_1' + \frac{1}{6}\varepsilon_2' + \frac{1}{3}\varepsilon_3'\right]\alpha_1^2 + \left[\frac{1}{2}\varepsilon_1' + \frac{1}{6}\varepsilon_2' + \frac{1}{3}\varepsilon_3'\right]\alpha_2^2 + \left[\frac{2}{3}\varepsilon_2' + \frac{1}{3}\varepsilon_3'\right]\alpha_3^2\right) + B_2\left(\left[\frac{1}{3}\left(-\varepsilon_2' + \varepsilon_3'\right)\right]\alpha_2\alpha_3 + \left[\frac{1}{3}\left(-\varepsilon_2' + \varepsilon_3'\right)\right]\alpha_1\alpha_3 + \left[-\frac{1}{2}\varepsilon_1' + \frac{1}{6}\varepsilon_2' + \frac{1}{3}\varepsilon_3'\right]\alpha_1\alpha_2\right). \quad (1.28)$$

Since the strains in a MnSi(111) film along $[1\,\bar{1}\,0]$ and $[1\,1\,\bar{2}]$ are expected to be the same, $\varepsilon_1' = \varepsilon_2' = \varepsilon_{||}$, and the equation can be written as,

$$\begin{aligned} w_{me} &= B_1\left(\left[\frac{2}{3}\varepsilon_{||}+\frac{1}{3}\varepsilon_{\perp}\right]\left[\alpha_1{}^2+\alpha_2{}^2+\alpha_3{}^2\right]\right) \\ &+B_2\left(\left[\frac{1}{3}\left(-\varepsilon_{||}+\varepsilon_{\perp}\right)\right]\left[\alpha_2\alpha_3+\alpha_1\alpha_3+\alpha_1\alpha_2\right]\right) \\ &=\frac{B_2}{3}\left(\varepsilon_{\perp}-\varepsilon_{||}\right)\left(\frac{3}{2}\cos^2\theta-\frac{1}{2}\right). \end{aligned} \tag{1.29}$$

From Eq. (1.29), one can see that the magnetoelastic stress contribution is isotropic and is therefore dropped from the final expression for the energy density. The magnetoelastic coupling therefore gives rise to a uniaxial MCA and a comparison between Eq. (1.29) and Eq. (1.14) gives,

$$K_u = \frac{B_2\left(\varepsilon_{\perp}-\varepsilon_{||}\right)}{2}. \tag{1.30}$$

Helical and conical phases are not the only stable phases. To predict the magnetic state of the system, it is important to consider the total energy density functional, $w(\vec{M})$. Other possible solutions can then be found by minimizing the total energy density W,

$$\begin{aligned} W &= \int w\left(\vec{M}\right)\,dr \\ &= \int\ (-\frac{AS}{2M_{\mathrm{sat}}^2a^3}\vec{M}\cdot\nabla^2\vec{M}+\frac{SD_0}{M_{\mathrm{sat}}{}^2a^3}\vec{M}\cdot\left(\nabla\times\vec{M}\right) \\ &+\frac{K_u}{M_{\mathrm{sat}}^2}\left(\vec{M}\cdot\hat{n}\right)^2-\mu_0\vec{H}\cdot\vec{M}-\frac{1}{2}\mu_0\vec{H}_{Demag}\cdot\vec{M})dV. \end{aligned} \tag{1.31}$$

Four possible solutions [58] for a film with uniaxial anisotropy are shown in Fig. 1.7.

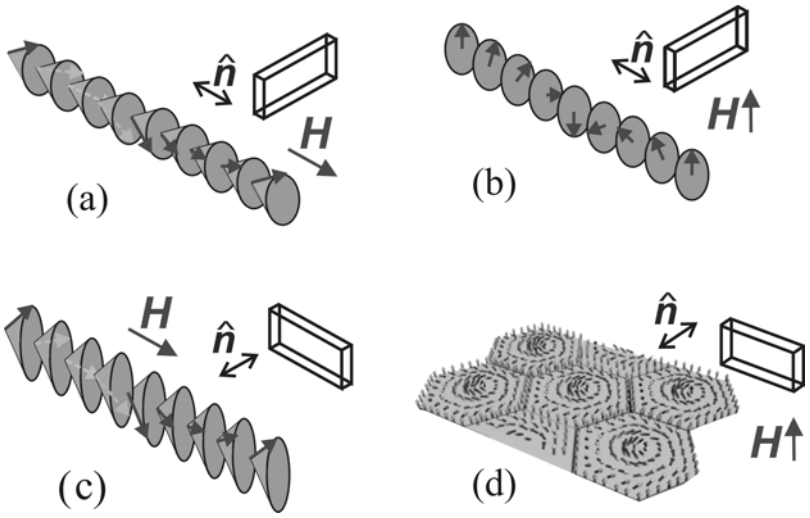

Figure 1.7. Four possible solutions of Eq. (1.31) for cubic helimagnetic thin films with in-plane magnetization where (a) is a conical phase in an applied field parallel to the film normal, (b) is a helicoid phase, which is a helix distorted by the applied field perpendicular to the propagation vector $\vec{Q}$, (c) is an elliptically distorted conical phase formed in a strong in-plane magnetic field and (d) is a hexagonal Skyrmion lattice with elliptical distortions due to the affect of an uniaxial anisotropy with the unit vector $\hat{n}$ indicating the direction of the uniaxial anisotropy. (Courtesy of Dr. U. K. Rößler and Prof. A. N. Bogdanov, Leibniz Institute for Solid State and Materials Research)

1.3 Growth Properties of MnSi Thin Films Grown by SPE on Si(111)

Since the lattice constant of Si(111) is similar to that of epitaxial MnSi films, various research groups have explored the growth properties of epitaxial MnSi thin films on Si(111) in order to generate smooth defect free thin films [24, 43 – 51]. Solid phase epitaxy (SPE) studies by various research groups have reported a variety of temperature dependant phases when amorphous Mn is deposited at RT on a Si(111) substrate and then

annealed. MnSi formation has been observed over temperatures ranging between 350 – 520 ºC [43 – 47, 49]. Lian and Chen [59] reported the formation of a $MnSi_{1.7}$ phase at temperatures greater than 600 ºC and Ctistis *et al*. observed a Mn_5Si_3 phase formation at a temperature of 325 ºC [60]. High quality epitaxial MnSi thin films grown by depositing alternating layers of Si and Mn at RT and then annealing at temperatures between 200 – 300 ºC have also been reported [48, 50, 51].

Evans *et al*. [43] performed *in-situ* scanning tunnelling microscopy (STM) and low energy electron diffraction (LEED) studies on depositions of Mn on Si(111) at RT. They observed the formation of 3D islands with a minimum thickness of 0.4 nm and a $\sqrt{3}\times\sqrt{3}$ surface terminated reconstruction when less than 0.4 nm of Mn was deposited at RT and annealed at temperatures ranging from 325 ºC to 450 ºC. Deposition of 0.4 nm of Mn at RT and annealing at 350 ºC resulted in almost complete coverage of the Si(111) substrate with a $\sqrt{3}\times\sqrt{3}$ superstructure. However, small holes with a minimum depth of 0.4 nm were observed, which when combined with the observed minimum height of the 3D islands, provided an indication that there was a minimum stable thickness for the $\sqrt{3}\times\sqrt{3}$ over-layer.

Shivaprasad *et al*. performed electron energy loss spectroscopy (EELS), Auger electron spectroscopy (AES) and low energy electron diffraction (LEED) measurements to determine that the $\sqrt{3}\times\sqrt{3}$ phase corresponded to the formation of MnSi [44]. A MnSi B20 structure showing a (1 x 1) MnSi unit cell similar in size to $\sqrt{3}\times\sqrt{3}$ Si(111) unit cell is shown in Fig 1.8.

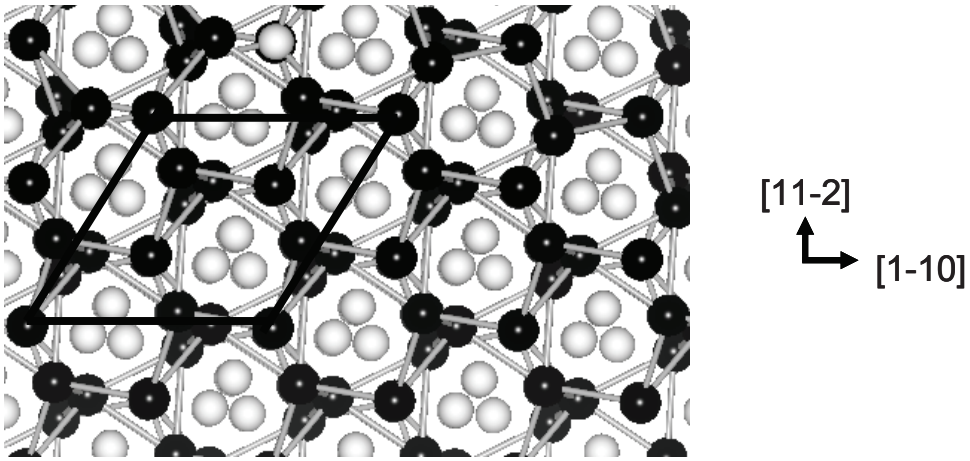

Figure 1.8. Top view of ball and stick model of a MnSi B20 structure showing the MnSi(111) unit cell, which is closely lattice matched to Si(111). The black balls represent Mn atoms and the white balls Si atoms.

Nagao *et al*. [45] offered an explanation for MnSi formation on Si(111) and proposed a mechanism for $\sqrt{3}\times\sqrt{3}$ island formation. From STM imaging, they showed that the structure of the silicide islands changed depending on the level of Mn coverage, annealing time and annealing temperature after deposition on a wafer at RT. As the Mn atoms impinge on the Si(111) surface, they weakly adsorb and form small clusters that keep the (7 x 7) morphology of the clean Si(111) substrate. During the annealing process, the clusters grow laterally into one another and the larger clusters begin to react with the Si(111) surface defects and form $\sqrt{3}\times\sqrt{3}$ islands.

Photoemission spectroscopy (PES) employed by Kumar *et al*. [47] determined the electronic structure of Mn thin films. Metal-silicon reaction was reported to occur between one monolayer (ML) of Mn and the Si(111) substrate at RT, which lead to the formation of MnSi at the interface. By depositing 2 – 5 ML of Mn on the Si(111) substrate and annealing to 400 ºC, a metallic phase was created and PES analysis

suggested that annealing at 400 ºC leads to an almost complete reaction between Mn and Si to form MnSi. STM images of the surface found that MnSi islands grew laterally to completely cover the Si surface leaving small areas of bare Si. A hexagonal network of dislocations in the silicide film resulted from the lattice mismatch between the Si and the silicide growth. STM images also showed evidence of deep holes as well as flat areas on the film surface. Kumar *et al*. proposed that the holes act as local strain relief or the formation of the holes was required to further supply Si in the silicide reaction [47]. PES analysis also determined that a Si over-layer formed on the MnSi thin film [47].

Density functional theory (DFT) calculations performed by Hortamani *et al*. [23] found that the Si(111) surface was compatible with the formation of a B20 MnSi structured thin film and the addition of a Si capping layer enhanced the stability of the film. Hortamani *et al*. also predicted that the Mn atoms at the MnSi/Si interfaces would produce a large magnetic moment.

In order to resolve the problem of inhomogeneities in SPE thin film growth, Magnano *et al*. [48] co-deposited 2 ML Mn and 2 ML Si at RT on Si(111). After they annealed the sample at 200 ºC for 10 minutes, they compared the sample with a SPE grown film formed from a 3 ML deposition of Mn at RT annealed at 350ºC for 10 minutes. LEED images provided evidence of a sharper pattern with the co-deposited growth indicating a more ordered film than films grown by SPE.

A high quality B20 structure was confirmed by *in-situ* STM images by Higashi *et al.* in which they deposited 1.5 ML of Si followed by 3 ML Mn and another 1.5 ML Si [24]. This deposition, annealed at 250º C for 5 minutes, produced atomically flat surfaces with 2% of the surface covered by holes. Higashi *et al*. compared this film to a series of

SPE grown samples with varying thicknesses of 1.5, 3 and 5 ML. The 1.5 ML annealed samples generated 2D islands with a minimum height of 2 QL by reacting with the Si(111) substrate and 1 QL heights were observed only after the formation of 2 QL islands suggesting that 2 QL is the minimum thickness for initial epitaxial growth. Density functional theory [23] shows that MnSi will not form a wetting layer on Si(111). Island growth is expected for thicknesses up to 3 ML and in the case of a 3 ML deposition of Mn, there is not enough Si at the surface to react completely with the deposited Mn. Therefore in order for the MnSi reaction to continue, holes are generated on the Si(111) surface around the 2 QL islands. The generated holes are even deeper in the case of 5 ML and the MnSi layer is no longer flat due to collapsed regions in the substrate caused by the removal of Si. By depositing 3 ML of Si and 3 ML of Mn, the Mn can react with the deposited Si instead of reacting with the substrate and creating holes. This thickness was found to generate higher quality films due to a 3 ML thickness being equivalent to a thickness of 2 quadlayers.

Although there has been a large amount of research on the magnetic and pressure dependence of bulk MnSi, the magnetic properties of MnSi thin films have only recently been explored. Magneto-optic Kerr effect measurements performed on MnSi films showed evidence of magnetic order on the SPE grown MnSi thin films, but an accurate determination of T_C was hampered by the low signal-to-noise ratio in the measurements [52]. However, Magnano *et al*. [53] recently reported a measurement of $T_C \sim 30$ K, for Ag/24nm MnSi/Si(111), which they associate with helical magnetic order. They observed a second magnetic transition at $T_C > 300$ K, which they suggest is due to a ferromagnetic phase at the MnSi/substrate interface. The result of this thesis contests this

claim and points to the Ag/MnSi interface of their samples as an origin of the ferromagnetic behaviour.

Chapter 2 – Experimental Techniques

In this chapter, the sample preparation and calibration procedures are described. A brief description of the x-ray diffraction (XRD), x-ray reflectometry (XRR) and polarized neutron reflectometry (PNR) techniques used to investigate the MnSi thin films are discussed. Finally, a discussion of superconducting quantum interference device (SQUID) magnetometry is presented.

2.1 Sample Preparation

MnSi thin films were prepared on both high ($> 5000\,\Omega\cdot\mathrm{cm}$) and low ($1 - 20\,\Omega\cdot\mathrm{cm}$) resistivity boron doped Si(111) wafers ± 0.5º. The wafers were degreased in acetone and methanol ultrasonic baths for 10 minutes, rinsed in de-ionized water, placed into a 70 ºC solution of ammonium hydroxide, hydrogen peroxide, and de-ionized water in a ratio of 1:2:10 for 10 minutes. The wafers were rinsed a second time, and were blown dry with dry nitrogen and immediately loaded into an ultra high vacuum (UHV) VG-V80 SiGe molecular beam epitaxy chamber with the base pressure of the system less than 5×10^{-9} Pa. A silicon oxide layer on the surface of the wafer was desorbed by heating the substrate from a temperature of 600 ºC to a temperature of 800 ºC in approximately 5 minutes. The temperature was then held at 800 ºC for one hour and then cooled to a temperature of 600 ºC at a rate of less than 1 ºC/s. At 600 ºC, a 20-nm Si buffer layer was deposited before cooling the substrate to RT at a rate less than 1 ºC/s. Reflection high energy electron diffraction (RHEED) observation [61] of the substrate performed *in-situ* with a KSA400 analytical RHEED system at an energy of 12 kV shows a (7 × 7) reconstruction that is consistent with a high purity surface (Fig. 2.1 (a)). An

atomic force microscope (AFM) measurement of the substrate provided an estimate of the roughness of the wafer surface. The RMS roughness of the wafer surface was determined to be between 0.3 – 0.5 nm after wafer cleaning, oxide removal and placing a 20-nm buffer layer on the surface. An *ex-situ* AFM image of the wafer, with a native oxide layer is shown in Fig. 2.2.

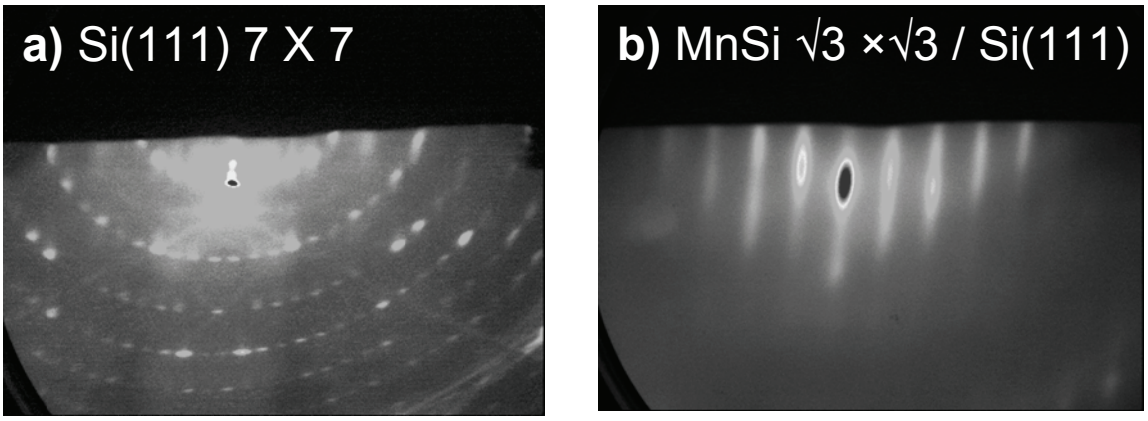

Figure 2.1. RHEED images of a) Si(111) wafer after oxide removal. The (7 × 7) reconstruction is consistent with a high quality surface. b) After annealing MnSi on a Si(111) substrate, a (√3 × √3) reconstruction is visible for a RHEED beam along the <110> direction. The RHEED pattern indicates a relatively smooth single crystal epitaxial layer.

Two methods were used to grow epitaxial MnSi thin films: solid phase epitaxy and molecular beam epitaxy. For the SPE growths, an amorphous layer of Mn deposited onto a Si(111) substrate at RT was annealed until a MnSi thin film formed. For MBE grown films, a 0.5-nm Mn layer was deposited onto a Si(111) substrate at RT and the sample was annealed at 400 ºC until the formation of a 1.0-nm thick MnSi(111) crystal film occurred [47, 50]. This was followed by co-deposition of Mn and Si onto this MnSi(111) film until the targeted film thickness was achieved. A thin amorphous Si over-

layer with a thickness of either 6 nm or 20 nm was added at RT protected the thin films from oxidation.

The MnSi thin films were grown under RHEED observation until a characteristic ($\sqrt{3} \times \sqrt{3}$) surface reconstruction [24] [43] [44] appeared (Fig. 2.1 (b)) that signalled the formation of MnSi.

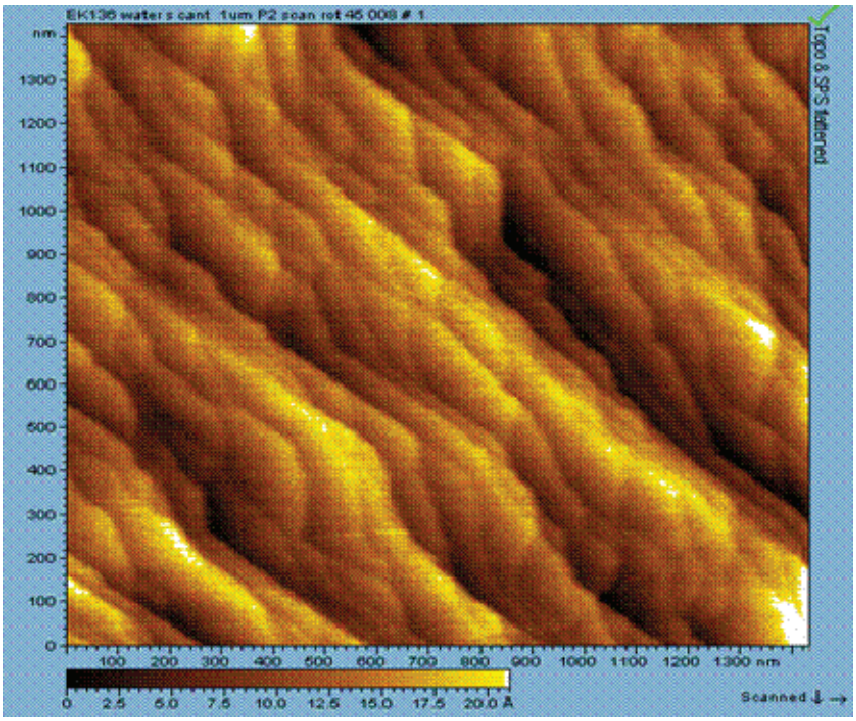

Figure 2.2. An *ex-situ* AFM image of a typical Si(111) wafer used as a substrate to grow MnSi films. (Courtesy of Prof. M. H. Jericho, Dalhousie University)

2.2 Calibration of Growth

The thickness of the SPE grown MnSi films was determined by measuring the amount of Mn deposited onto the Si(111) substrates. This was achieved by measuring the Mn flux rate with a home-built flux monitor that consisted of a Bayard-Alpert-type

ionization gauge. The flux monitor was calibrated with a series of Mn thin film samples with thicknesses ranging between 10 – 20 nm, grown at rates from 0.05 nm/min to 0.4 nm/min on room temperature Si(111) substrates. A thin protective layer of amorphous Si with a thickness of either 6 nm or 20 nm was then added at RT. The thickness of the deposited Mn, d_{Mn}, was measured using x-ray reflectometry (XRR) in order to calibrate the Mn flux rate. A quartz oscillator measured the thickness of the deposited Si.

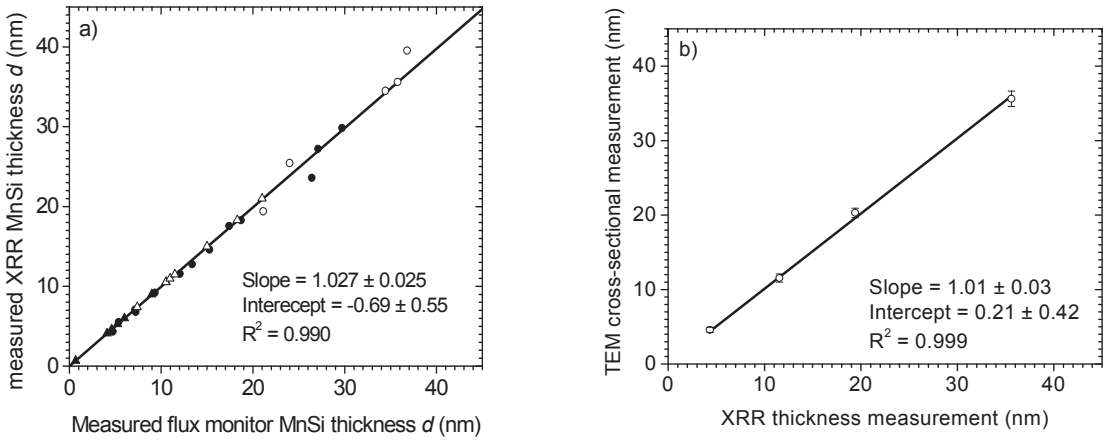

Figure 2.3. a) Measured XRR MnSi thickness as a function of measured flux monitor MnSi thickness. SPE samples are represented by triangular symbols and MBE grown samples are shown as circular symbols. Open circles are samples with high concentrations of $MnSi_{1.7}$ precipitates and open triangles are samples with a large interface roughness, b) Cross-sectional transmission electron microscope thickness measurements as a function of XRR thickness measurements. Fit to both sets of data shown by solid line.

In Fig. 2.3 (a), the MnSi thickness determined from XRR is compared to the thickness obtained from the flux monitor. There is good agreement between the flux and XRR measurements for nearly all of the samples. The discrepancy in some of the SPE

grown samples is due to interface roughness that exists in the thicker samples making the XRR thickness measurements difficult to analyze. In the case of the MBE samples, samples with a high amount of $MnSi_{1.7}$ precipitates also make it difficult to analyze the XRR data. Cross-sectional transmission electron microscopy (TEM) thickness measurements of several MnSi thin films are in excellent agreement with thickness measurements performed by XRR as shown in Fig. 2.3 (b).

2.3 X-ray Diffraction

X-ray diffraction is a non-destructive technique that provides information about the chemical composition and the crystallographic structure of a material. X-rays are scattered by the electron distribution in the sample and the elastically scattered x-rays carry information about the crystal structure [62]. In Fig. 2.4, the incident rays are

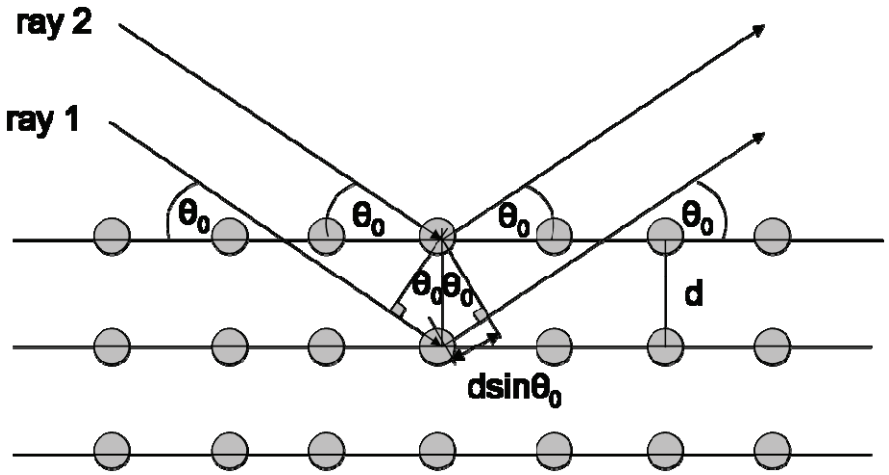

Figure 2.4. Illustration of Bragg's Law. The angle θ_0 is the angle of the incident beam with respect to the atomic planes {Adapted from [22]}.

scattered from the atomic planes of a crystal, with a spacing *d* [22]. The path difference between ray 1 and ray 2 reflected from adjacent planes of atoms is $2d\sin\theta_0$ where θ_0 is measured with respect to the surface of the plane. Constructive interference occurs when the path length difference is equal to an integer, *n*, number of wavelengths, λ, known as Bragg's law:

$$2d\sin\theta_0 = n\lambda\,. \tag{2.1}$$

By varying the angle θ_0, the Bragg condition can be satisfied for different *d*-spacings in polycrystalline materials. Plotting the angular positions and intensities of the resultant diffraction peaks provides information about the chemical composition and the crystallographic structure of the material being analyzed.

Measurements were performed with Cu (K_α) radiation produced from a Siemens D500 diffractometer equipped with a diffracted beam monochromator. A schematic of the experimental setup for XRD is shown in Fig. 2.5. A source of monochromatic x-rays of wavelength λ irradiates a sample at an angle of incidence θ_0 and a detector records the reflected intensity at an angle $2\theta_0$. Slits *S1* and *S2* control the beam width and divergence. *S3* is an anti-scatter slit and slits *S4* and *S5* are the monochromator slits. For a $\theta_0 - 2\theta_0$ scan, the source is fixed and the sample is rotated in concert with the detector to ensure that the detector always measures at an angle of reflection equal to the angle of incidence.

In order to align the crystallographic planes of the sample with the source and detector, a rocking curve measurement is performed. For a rocking curve measurement, the source θ_0 and detector $2\theta_0$ are fixed according to known diffraction peaks of either

the Si(111) or Si(222) substrate planes. The sample angle Ω is scanned to align crystallographic planes with the source and detector. The Si peaks also serve as an accurate internal calibration standard for the MnSi(111) peaks.

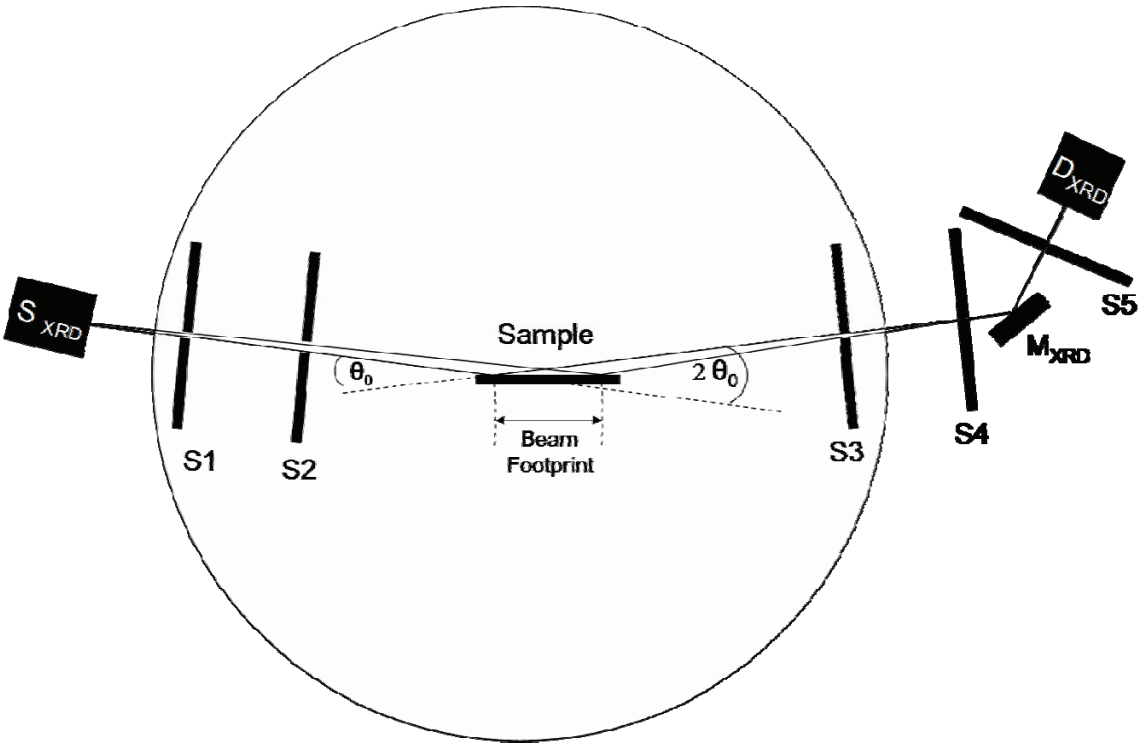

Figure 2.5. Schematic representation of XRD and XRR setups where S_{XRD} is the x-ray source, $S1$ and $S2$ are the incident beam slits, $S3$ is an anti-scatter slit, $S4$ and $S5$ are the monochromator slits, M_{XRD} is the monochromator and D_{XRD} is the detector.

In analyzing the MnSi thin films, $\theta_0 - 2\theta_0$ scans measured between 10º and 80º determined whether the MnSi thin film had a single crystalline structure or contained other silicides of manganese. The shift of the MnSi(111) peak [62] with respect to the bulk MnSi(111) diffraction peak at $2\theta_0 = 34.05$º [20], gave the out-of-plane compressive

strain $\varepsilon_{\perp}$ created by the lattice mismatch between MnSi and Si. The out-of-plane strain is,

$$\varepsilon_{\perp} = \frac{d_{film} - d_{bulk}}{d_{bulk}}, \tag{2.2}$$

where d_{film} is the *d*-spacing of the film and d_{bulk} is the *d*-spacing of the bulk MnSi. On either side of the MnSi(111) peak, Kiessig fringes are typically observed, which arise from the finite thickness of the film. With thicker films, the distance between the fringes becomes smaller until only a shoulder on either side of the Bragg peak can be resolved. The thin film thickness can be determined by analyzing these fringes [63], which provides useful information for fitting the XRR data, as described in the next section. Using kinematical scattering theory, Boulle *et al*. derived an analytical expression that describes the XRD profile of a single epitaxial thin film with interfacial roughness. For films where different regions of the film scatter coherently, the diffracted intensity has the following form,

$$I(q_z) = \frac{|F_h|^2 \exp\left(-q_z^2 \sigma_L^2\right)}{q_z^2} \times \left\{ \begin{array}{l} 1 + \exp\left[-q_z^2\left(\sigma_L^2 + \sigma_U^2 - 2r_{icc}\sigma_L\sigma_U\right)\right] \\ -2\exp\left(-\frac{1}{2}q_z^2\left(\sigma_L^2 + \sigma_U^2 - 2r_{icc}\sigma_L\sigma_U\right)\right)\cos\left(q_z d\right) \end{array} \right\}, \tag{2.3}$$

where I is the intensity, F_h is the structure factor, d is the thickness of the film, and σ_U and σ_L are the film roughness at the lower and upper interface boundary, respectively. The parameter r_{icc} is the interface correlation coefficient that describes how the upper and lower film interfaces are correlated (r_{icc} = 0 corresponds to uncorrelated, r_{icc} = 1

corresponds to completely correlated and r_{icc} = -1 corresponds to completely anti-correlated). q_z is the component of the scattering vector parallel to the interface normal, and $q = |\vec{q}| = |\vec{k}_{in} - \vec{k}_r| = \frac{4\pi \sin\theta_0}{\lambda}$. The incident and reflected wave vectors are $\vec{k}_{in}$ and $\vec{k}_r$, respectively, and $|\vec{k}_{in}| = |\vec{k}_r| = \frac{2\pi}{\lambda}$ for elastically scattered x-rays [64]. For films with a mosaic structure, different regions of the film scatter incoherently and the intensity can be described by the following equation [63]:

$$I(q_z) = \frac{|F_h|^2}{q_z^2}\left\{2 - 2\exp\left[-\frac{1}{2}q_z^2\left(\sigma_L^2 + \sigma_U^2 - 2r_{icc}\sigma_L\sigma_U\right)\right]\cos(q_z d)\right\}. \quad (2.4)$$

The wings on either side of the MnSi(111) peak shown in Fig. 2.6, which are representative of all the thin film samples discussed in this thesis, have a concave shape that is consistent with an incoherent film described by Eq. (2.4). In order to analyze the XRD profiles of the MnSi(111) peak in the thin films, I performed a least squares fit of the data with Eq. (2.3) and Eq. (2.4) and found that the data was consistent with the incoherent model. The reason that not all regions of the MnSi film scatter coherently may be due to the mosaic spread in the films, as described in Chapter 3. Analysis of the MnSi(111) peak in Fig. 2.6, gave a thickness d = 26.7 ± 0.3 nm, with F_h = 4.1. Although the fits to the data were in good agreement with the thickness estimates from XRR analysis, I was unable to determine an interfacial roughness value from the fit since the fit is insensitive to interface roughness when $\sigma_U = \sigma_L$ and r_{icc} = 1, as can been seen from Eq. (2.4).

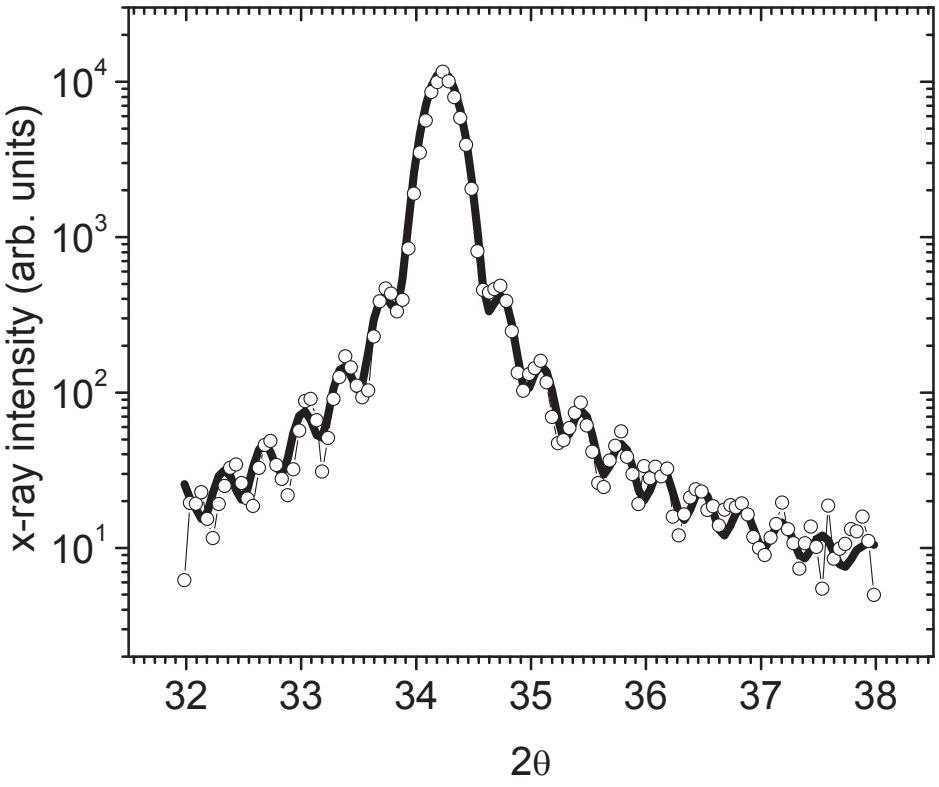

Figure 2.6. XRD diffractogram of a MnSi(111) peak for a 26.7 ± 0.3 nm MnSi thin film grown by molecular beam epitaxy on a Si(111) substrate. The fit to the Kiessig fringes with Eq. (2.4) (line) is in good agreement with the thickness determined by XRR.

2.4 Reflectivity

2.4.1 X-ray Reflectivity (XRR)

X-ray reflectivity (XRR) is used to determine the chemical structure of the MnSi thin films using the Siemens D500 diffractometer. Like XRD, XRR consists of $\theta_0 - 2\theta_0$ scans, although in the case of XRR, these are performed at grazing angles of incidence with the geometry shown in Fig 2.5. In this mode of operation, the reflectivity is sensitive to length scales much larger than atomic plane spacing, such as interface spacing [65]. For incident angles, θ_0, below a critical angle, θ_C, total external reflection occurs. The critical angle for Si is θ_C = 0.22º (q_c = 0.32 nm^{-1}) and for MnSi θ_C = 0.34º (q_c = 0.48 nm^{-1}). Above θ_C, x-rays penetrate the crystal and the interference between the scattered x-rays gives rise to fringes whose spacing is related to the layer thickness in the sample. The period of the interference fringes and the attenuation of their intensity are related to the thickness and the roughness of the layer, respectively.

Fig. 2.7 shows a reflectivity curve of a 4.6-nm MnSi thin film. The shorter period represents the 20-nm amorphous silicon protective layer and the larger period is due to the 4.6-nm MnSi layer. Surface roughness gives rise to diffuse scattering, resulting in a decrease in intensity of the specularly reflected beam. For the MnSi samples, the $\theta_0 - 2\theta_0$ scans were obtained between 0.3º and 7.0º. The surface of the sample was aligned with the source and detector by performing a rocking curve measurement at an angle less than the critical angle.

A rocking curve recorded below the critical angle shows both specular and diffuse components as shown in the inset of Fig. 2.8. The diffuse reflectivity, was measured by

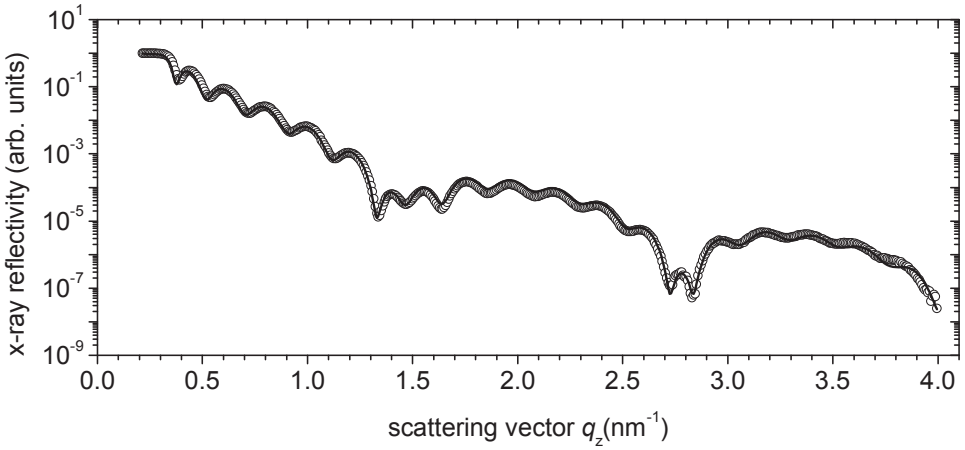

Figure 2.7. XRR-measurements (open circles) and simulation (line) of a 4.6 nm MnSi thin film on a Si(111) substrate. A 20 nm polycrystalline over layer protects the MnSi thin film from the *ex-situ* environment. The MnSi interface roughness was determined to be 0.46 nm.

performing a $\theta_0 - 2\theta_0$ scan with a sample offset $\Delta\Omega = 0.18^{\circ}$ (indicated by the arrow in the reflectivity data as shown in Fig. 2.8). The diffuse component was then subtracted from the $\theta_0 - 2\theta_0$ scan to obtain the specular reflectivity.

The size of the x-ray beam projected onto the sample, as shown in Fig. 2.5, is known as the beam footprint. For low angles of incidence, the footprint becomes larger than the size of the sample that results in an artificial drop in intensity with decreasing angle, as shown in Fig. 2.9 (a). In order to compensate for this effect, a linear footprint correction was applied to the portion of the data where the beam over fills the sample.

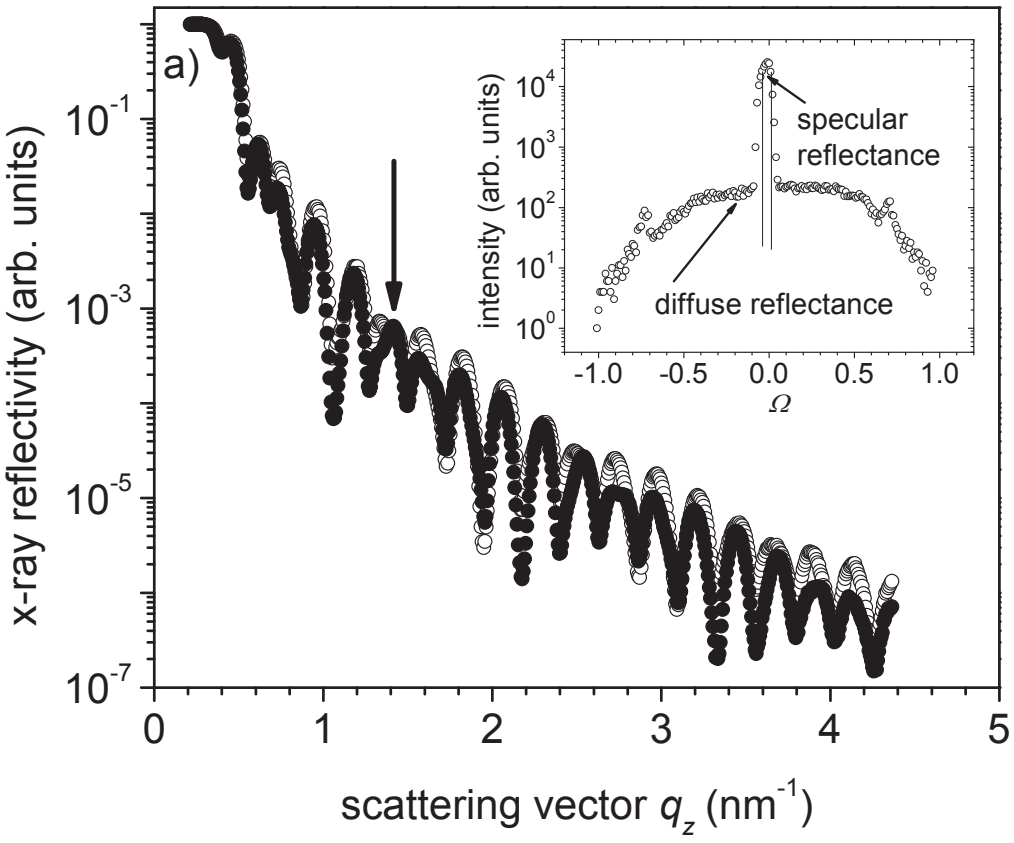

Figure 2.8. a) Footprint corrected XRR curves for a 26.7-nm MnSi thin film for sample angle $\Omega = 0^{\circ}$ (open circles), compared to the reflectivity after the diffuse reflectance measured at $\Omega = 0.18^{\circ}$ is subtracted out (solid circles). A rocking curve was performed at an angle $\theta_0 = 1.11^{\circ}$, shown by the arrow. The inset shows the rocking curve data specular and diffuse intensity regions of the XRR peak. The arrows indicate the two Ω for which $\theta_0 - 2\theta_0$ scans were performed.

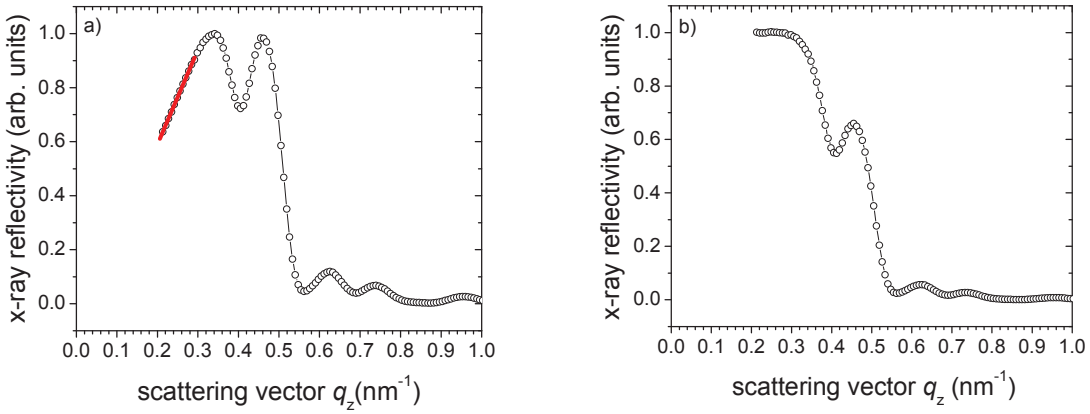

Figure 2.9. a) Reflectivity data before footprint correction. Below the critical angle, Q decreases linearly. A fit to the slope is shown by the straight line. b) Same data after a footprint correction.

2.4.2 Polarized Neutron Reflectivity

Owing to the magnetic moment of the neutron, polarized neutron reflectometry is a technique that can determine the magnetic structure of thin films in addition to the chemical structure. PNR measurements were performed at the NIST Center for Neutron Research with the NG-1 reflectometer (Fig. 2.10) using a neutron wavelength of 0.475 nm.

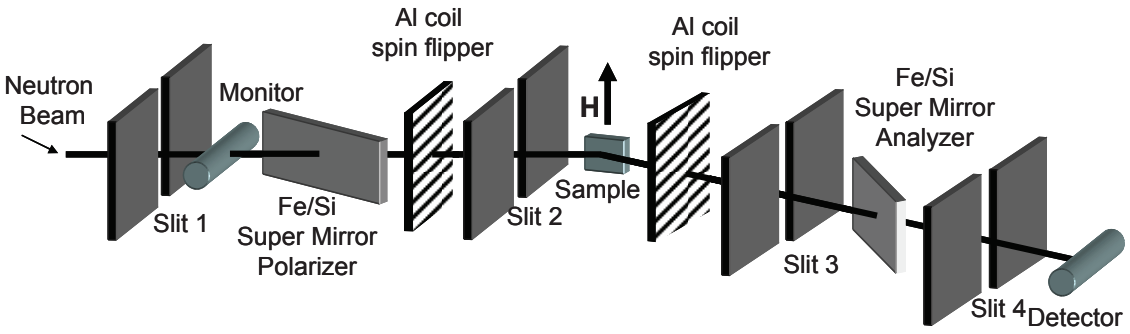

Figure 2.10. NG-1 reflectometer configuration (adapted from Nist, http://www.ncnr.nist.gov/instruments/ng1refl/Beamline_color.bmp).

A neutron polarizer, consisting of an Al-coil spin-flipper and a Fe/Si super-mirror, set the spin of the incident neutron parallel (+) or anti-parallel (−) to the external magnetic field. The flipper field, $\mu_0 H_F$, is perpendicular to both the neutron spin and neutron wavevector and its magnitude is adjusted to create a 180º rotation of the neutron spin as the neutron passes through the coil. A second Al-coil spin-flipper and super-mirror (the analyzer) selected the polarization detected by a He^3 detector. Together the polarizer and analyzer enabled measurement of four separate reflectivities R(+ +), R(− −), R(+ −), R(− +), where R(+ −) refers to the reflected intensity of up incident neutrons that have been spin-flipped and reflected as down neutrons. The R(+ +), R(− −) are the non-spin-flip reflectivities and the R(− +) and R(+ −) are the spin-flip reflectivities. Four separate background reflectivities were measured by performing $\theta_0 - 2\theta_0$ scans with an Ω-offset similar to the case of XRR. A footprint correction was also applied to the data during analysis.

2.5 Reflectivity Theory

In either PNR or XRR, the scattering vector, is much smaller than the reciprocal lattice vectors of the sample. Therefore, a continuum model can be used, where expressions for the reflectivity can be developed with an optical formalism in terms of the refractive indices of the sample. The Helmholtz equation,

$$\nabla^2 \vec{E} + k^2 \vec{E} = 0 , \tag{2.5}$$

describes electromagnetic (EM) wave propagation, and the Schrödinger equation,

$$\frac{\partial^2 \psi_S}{\partial r_S^{\,2}} + \frac{2m_n}{\hbar^2}\left(E_S - V_S\right)\ \psi_S = 0 , \tag{2.6}$$

describes the neutron propagation. In the case of x-ray radiation, the index of refraction, n_1, of a substance is,

$$n_1 = 1 - \frac{\lambda^2}{2\pi} r_e \rho_m (f' + if'') , \tag{2.7}$$

where $r_e = \frac{\mu_0 e^2}{4\pi\ m_e} = 2.818 \times 10^{-6}$ nm is the Thomson scattering length (or classical electron radius), ρ_m is the molecular number density of the material and *f'* and *f''* are the real and imaginary parts of the x-ray scattering factor. The real part of Eq. (2.7) can then be re-expressed in terms of an effective electron density, $\rho_e \approx \rho_m f'$,

$$n_1 = 1 - \frac{\lambda^2}{2\pi} r_e \rho_e . \tag{2.8}$$

The scattering length density (SLD) is the product of the number density of scatters and the scattering length. For x-rays the real part of the SLD is approximately $\rho_e r_e$, which

results in a refractive index that is slightly less than 1. The critical angle, θ_c is determined by $\cos\theta_c = n_1 = 1 - \frac{\lambda^2}{2\pi}\rho_e r_e$. Using the small angle approximation, this angle is,

$$\theta_c = \lambda\sqrt{\frac{\rho_e r_e}{\pi}}. \tag{2.9}$$

In the case of neutrons, the formalism is developed in a similar way, with an important difference — the scattering potential has a magnetic contribution. For neutrons, the index of refraction is dependent on the potential,

$$V_S = \frac{2\pi\hbar^2}{m_n}\rho_m b - g_n\mu_n\frac{\hbar}{2}\sigma_P \cdot B_{eff}, \tag{2.10}$$

where $b\left(\frac{2\pi\hbar^2}{m_n}\right)\rho_m$ is the nucleus-neutron potential energy term, and $g_n\mu_n\frac{\hbar}{2}\sigma_P \cdot B_{eff}$ is the Zeeman energy term. The nuclear scattering is given by the scattering length, *b*, and the neutron mass ($m_n = 1.675\times10^{-27}$ kg). The neutron SLD $= \rho_m b$. The magnetic scattering depends on the nuclear Landé factor, g_n = -1.913, the nuclear magneton ($\mu_n = \frac{e\hbar}{2m_n}$ = 5.05 x 10^{-27} J/T) and the neutron spin, $\vec{S}$. Eq. (2.10) is expressed in terms of the Pauli spin matrices $\sigma_P = \frac{2\vec{S}}{\hbar}$, in the basis of the two spin states $|+\rangle$ and $|-\rangle$ for a quantization axis determined by the direction of the external magnetic field,

$$\sigma_P \cdot B_{eff} = \begin{pmatrix} 0 & 1 \\ 1 & 0 \end{pmatrix} B_{eff_x} + \begin{pmatrix} 0 & -i \\ i & 0 \end{pmatrix} B_{eff_y} + \begin{pmatrix} 1 & 0 \\ 0 & -1 \end{pmatrix} B_{eff_z}. \tag{2.11}$$

In a magnetic thin film, the effective magnetic flux density $\vec{B}_{eff}$ is,

$$\vec{B}_{eff} = \mu_0\left(\vec{H}_{app} + \vec{M} + \vec{H}_{Demag}\right), \tag{2.12}$$

where $\mu_0\vec{H}_{\text{app}}$ is the applied external field, $\mu_0\vec{M}$ is the sample magnetization. The demagnetizing field, $\mu_0\vec{H}_{\text{Demag}} = -\mu_0 D\vec{M} = -\mu_0\begin{pmatrix}0&0&0\\0&0&0\\0&0&1\end{pmatrix}\vec{M}$ is zero when the magnetization is in-plane. In thin films $\mu_0\vec{H}_{\text{Demag}}$ cancels the contribution from the out-of-plane component of the magnetization, $\mu_0 M_z$, and the effective field can be written as,

$$B_{\text{eff}} = B_0 + \mu_0 M_{||}, \tag{2.13}$$

where $M_{||}$ is the in-plane component of the magnetization $\vec{M}$. Therefore, it is only possible to measure the in-plane magnetization with PNR. Solutions to Eq. (2.6) of the form $\psi_+(\vec{r}) = a_+ \exp\left(i\vec{k}\cdot\vec{r}\right)$ and $\psi_-(\vec{r}) = a_- \exp\left(i\vec{k}\cdot\vec{r}\right)$, generate four possible values for the wave vector *k,*

$$\left(k^{\pm}\right)^2 = \frac{2m_n E_S}{\hbar^2} - \left(4\pi\rho_m b \mp \frac{2m_n g_n \mu_n}{\hbar^2}|B|\right). \tag{2.14}$$

For $\vec{S} \parallel \vec{M}$, $|+\rangle$ and $|-\rangle$ are eigenstates and there is no spin-flip. However, for $\vec{S} \perp \vec{M}$, $\sigma_P \cdot B_{eff}$ mixes the spin states $|+\rangle$ and $|-\rangle$ resulting in spin-flip scattering. The general state for the combined incident and reflected neutron beam can then be written in terms of the eigenstates,

$$\psi(r) = \begin{bmatrix}\cos\left(\frac{\theta_A}{2}\right)\\ \sin\left(\frac{\theta_A}{2}\right)e^{i\phi}\end{bmatrix}\left(A_+ e^{+i\vec{k}^+\cdot\vec{r}} + B_+ e^{-i\vec{k}^+\cdot\vec{r}}\right) + \begin{bmatrix}-\sin\left(\frac{\theta_A}{2}\right)e^{-i\phi}\\ \cos\left(\frac{\theta_A}{2}\right)\end{bmatrix}\left(A\_e^{+i\vec{k}^-\cdot\vec{r}} + B\_e^{-i\vec{k}^-\cdot\vec{r}}\right), \tag{2.15}$$

where ϕ and θ_A are the azimuthal and polar angles, respectively (Fig. 2.11). For a neutron with spin and applied field oriented along the *z*-axis, as shown Fig. 2.11, the wave function is,

$$\psi_0(r) = \begin{bmatrix} A_{0_+} e^{ik^+ r} + B_+ e^{-ik^+ r} \\ A_{0_-} e^{ik^- r} + B_- e^{-ik^- r} \end{bmatrix}. \tag{2.16}$$

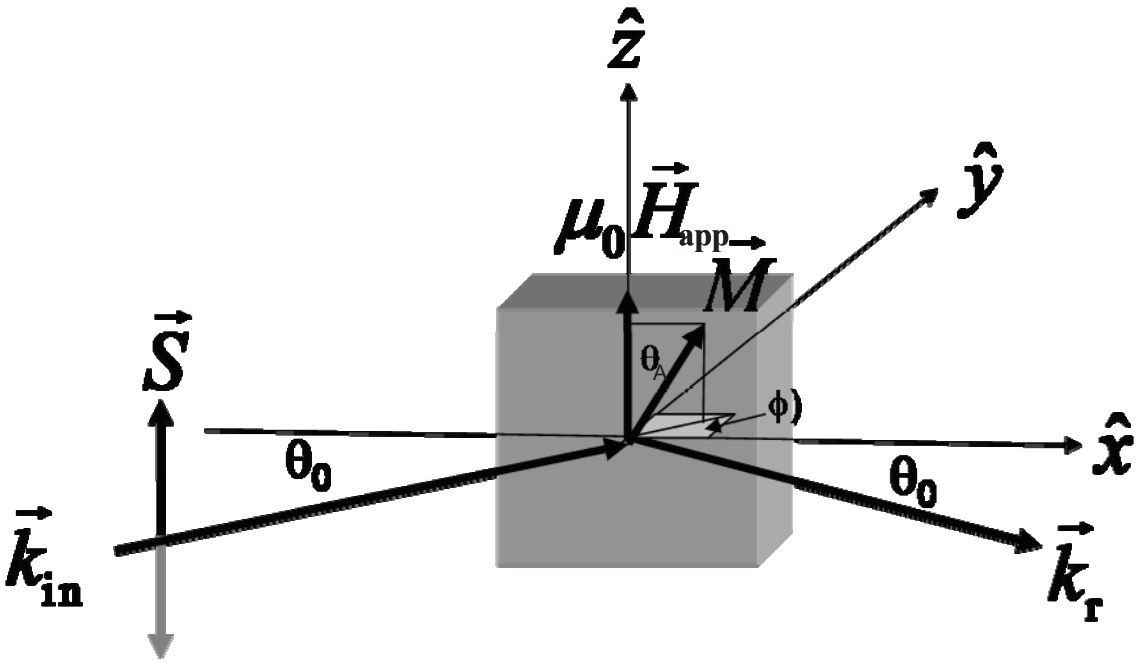

Figure 2.11. Diagram of the neutron diffraction geometry for a neutron with its spin $\vec{S}$ oriented along the z-axis and an applied field oriented along the *z*-axis.

The critical angle is determined from the continuity of $k_{\|}$ across the interface. Assuming *B* is small outside of the sample, the incident wavevector is,

$$(k_0)^2 = (k_0^+)^2 = (k_0^-)^2 = \frac{2m_n E_S}{\hbar^2}, \tag{2.17}$$

and the transmitted wave vectors are

$$\left(k_1^{\pm}\right)^2 = k_0^2 - 4\pi\rho_m\left(b \pm b_{\mathrm{m}}\right). \tag{2.18}$$

The index of refraction is then

$$n^{\pm} \approx 1 - \frac{2\pi\rho_m}{k_0^2}\left(b \pm b_{\mathrm{m}}\right), \tag{2.19}$$

and the critical angles for up and down neutrons are:

$$\theta_{\mathrm{C}}^{\pm} = \sqrt{\frac{4\pi\rho_m\left(b \pm b_{\mathrm{m}}\right)}{k_0^2}} = \lambda\sqrt{\frac{\rho_m\left(b \pm b_{\mathrm{m}}\right)}{\pi}}. \tag{2.20}$$

The reflection coefficient, which is the experimentally determined quantity in both XRR and PNR, can be determined from the boundary conditions at each interface. Fig. 2.12 (a) shows a wave incident on an interface located in the x-z plane at $z = 0$ with the incident $\vec{k}_{in}$, reflected $\vec{k}_r$ and refracted $\vec{k}_{tr}$ wave vectors. The angle of refraction is labelled θ_1. Fig. 2.12 (b) shows the change in the wave vector amplitude and wavelength of a wave as it travels from vacuum (air) into the medium, where $k_0 = \left|\vec{k}_{in}\right| = \left|\vec{k}_r\right| = \left|\vec{k}_{tr}\right| / n_1$ and $k_1 = \left|\vec{k}_{tr}\right|$ [64].

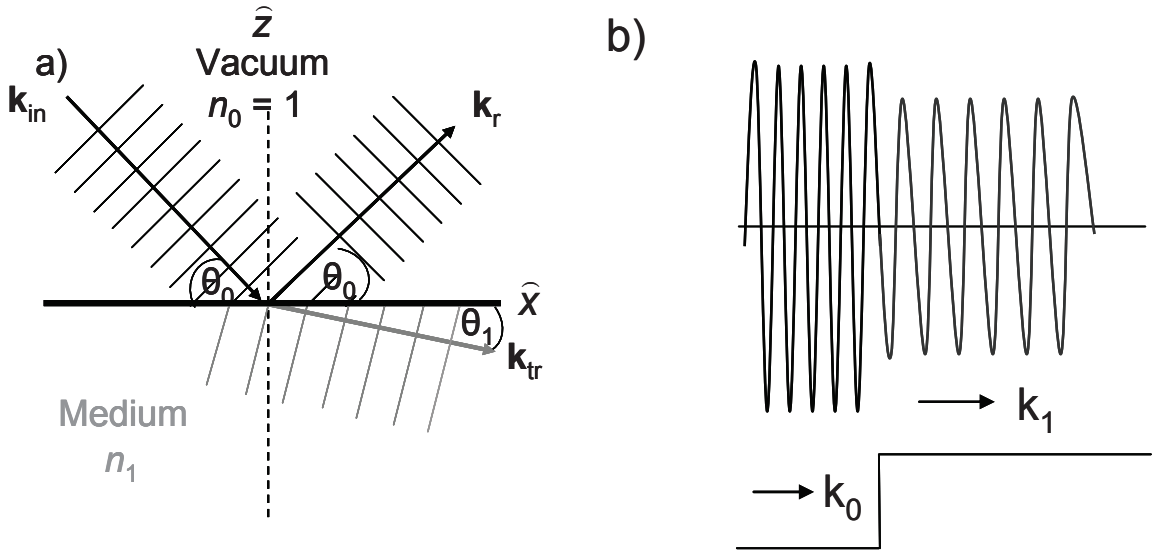

Figure 2.12. a) Schematic representation of the change in the incident wavevector k_{in} after undergoing reflection (shown by the wavevector k_r) and transmission (shown by the wavevector k_{tr}) as it propagates into the medium from vacuum (air). b) A representation of the change in the wave vector amplitude and wavelength of wave as it travels from vacuum (air) into the medium where $k_0 = \left|\vec{k}_{in}\right| = \left|\vec{k}_r\right| = \left|\vec{k}_{tr}\right| / n_1$ and $k_1 = \left|\vec{k}_{tr}\right|$

The incident, reflected and transmitted wave vectors shown in Fig. 2.12 are

$$\vec{k}_{in} = k_0(\cos\theta_0\hat{x} - \sin\theta_0\hat{z}), \tag{2.21}$$

$$\vec{k}_r = k_0(\cos\theta_0\hat{x} + \sin\theta_0\hat{z}), \tag{2.22}$$

$$\vec{k}_{tr} = k_0 n_1(\cos\theta_1\hat{x} - \sin\theta_1\hat{z}), \tag{2.23}$$

respectively.

In the case of XRR, the *x*-component of the electric field is continuous across the interface at z = 0, and for plane waves this boundary condition may be expressed as,

$$E_{in}e^{i(\omega t-k_0(\cos\theta_0 x))}+E_r\,e^{i(\omega t-k_0(\cos\theta_0 x))}=E_{tr}\,e^{i(\omega t-k_0 n_1(\cos\theta_1 x))}, \tag{2.24}$$

which also leads to,

$$E_{in}\ +E_r\ =E_{tr}\ . \tag{2.25}$$

Since the *x*-component of the magnetic field is also continuous across the interface,

$$\frac{\partial E_{yin}}{\partial z}+\frac{\partial E_{yr}}{\partial z}=\frac{\partial E_{ytr}}{\partial z}, \tag{2.26}$$

and

$$\left(E_{in}\ -E_r\ \right)\cos\theta_0=n_1E_{tr}\ \cos\theta_1\,. \tag{2.27}$$

By combining equations Eq. (2.25) and Eq. (2.27), one obtains the Fresnel equations, expressed in terms of the reflected amplitude, $r = E_r / E_{in}$,

$$r=\frac{k_0-k_1}{k_0+k_1}, \tag{2.28}$$

and the transmitted amplitude, $t = E_{tr} / E_{in,}$

$$t=\frac{2k_0}{k_0+k_1}. \tag{2.29}$$

The reflectivity, *R*, measured in an XRR experiment is related to the reflected amplitude by:

$$R=\left|r\right|^2=rr^*. \tag{2.30}$$

To illustrate how geometry affects the reflectivity, Fig. 2.13 shows the results from calculations of the reflectivity from (1) an infinite sample, (2) a perfect 10-nm thick film,

and (3) a 10-nm film with a 0.5-nm RMS roughness. For case (1), the intensity of the reflectivity above the critical angle drops as $q_c^4/(16\ q_z^4)$. For case (2), Fig 2.13 shows an oscillation in the reflectivity whose period dependents on the thickness of the film. Case (3) shows that the roughness at the interfaces attenuates the reflectivity signal (Fig. 2.13).

For samples with multiple layers, multiple reflections and interference from these reflections generate more complicated oscillation patterns in the detected reflectivity as shown in Fig. 2.7. In this case, numerical modelling software, such as Simulreflec, is needed to determine the thickness, roughness and densities of the multiple layers [66]. The calculation performed by the Simulreflec software uses an exact recursive matrix calculation [64, 66] and the calculations are performed by applying the boundary conditions for the electric and magnetic field at each of the interfaces between the layers.

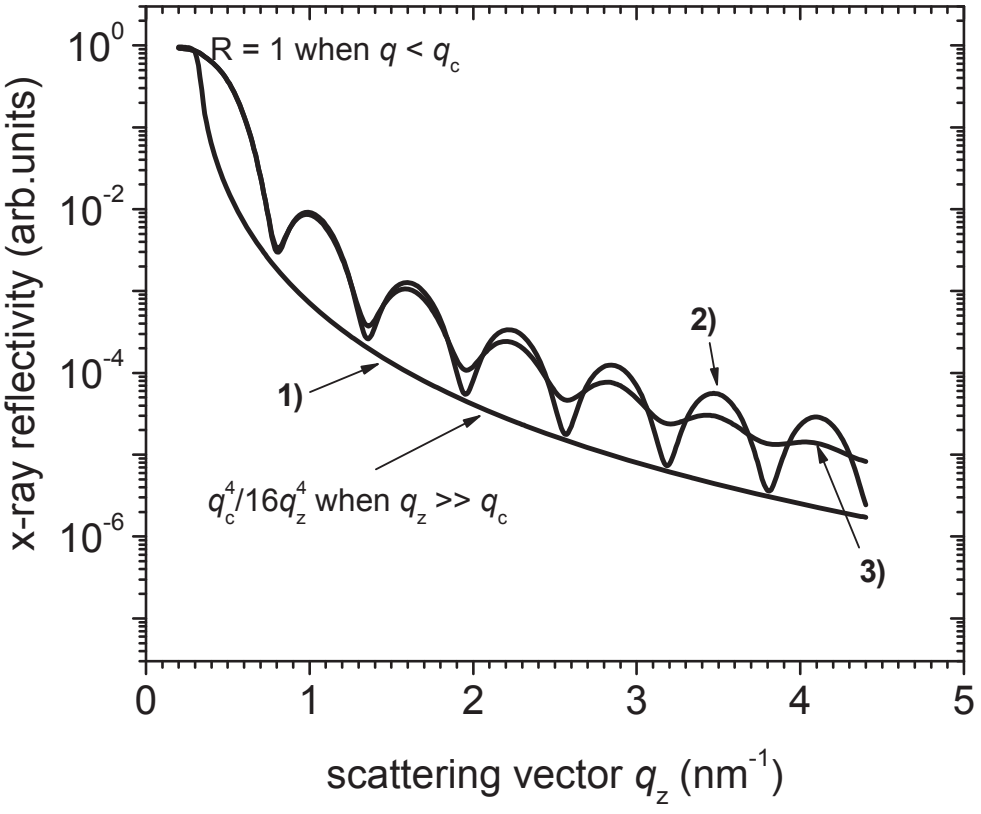

Figure 2.13. 1) Reflectivity curve simulation of (1) an infinite sample, (2) a perfectly smooth sample with a thickness d = 10 nm, and (3) a sample of thickness d = 10 nm with an interface roughness σ_R = 0.5 nm on an infinite substrate.

In the case of PNR, the boundary conditions for the continuity of ψ_S and $\nabla \psi_S$ across the interface give rise to a set of Fresnel equations, similar to equations Eq. (2.28) and Eq. (2.29). However, since the refractive index in the case of neutrons is spin-dependent, the Fresnel equations are also dependent on spin. In the case of a semi-infinite

ferromagnetic substrate, where the magnetization aligns along an in-plane magnetic field ($\phi = 0^{o}$, Fig. 2.11), the non-spin flip reflection amplitudes are,

$$r^{++} = \frac{k_{0_z} - k_{1_z}^{+}}{k_{0_z} + k_{1_z}^{+}},\ r^{--} = \frac{k_{0_z} - k_{1_z}^{-}}{k_{0_z} + k_{1_z}^{-}} \text{ and } r^{+-} = r^{-+} = 0, \tag{2.31}$$

assuming that the wavevector in vacuum is $k_0 = k_0^{+} = k_0^{-}$. The difference between the two non-spin flip reflectivities, R(+ +) = $|r^{++}|^2$ and R(– –) =$|r^{--}|^2$ is shown in Fig. 2.14 for a simulation of a 100-nm Fe film on a silicon substrate. The Fe film has a moment of 2.2 μ_B / atom. From Eq. (2.20), this difference can be used to determine the magnetization. Both the spin-flip intensities are zero, as expected since $|+\rangle$ and $|-\rangle$ are eigenstates of the system.

In the case where an in-plane magnetic field is applied perpendicular to the sample magnetization, the non-spin flip reflected amplitude can be expressed as an average of the reflection amplitudes in Eq. (2.16), calculated for the previous experimental geometry:

$$r = \frac{1}{2}\left(r^{++} + r^{--}\right). \tag{2.32}$$

However, the spin-flip reflected amplitude is given by,

$$r^{+-} = \frac{k_{0_z}\left(k_{1_z}^{+} - k_{1_z}^{-}\right)}{2\left(k_{0_z} + k_{1_z}^{+}\right)\left(k_{0_z} + k_{1_z}^{-}\right)}, \tag{2.33}$$

because the component of $\vec{S} \perp \vec{M}$ mixed $|+\rangle$ and $|-\rangle$, as shown by Eq. (2.11).

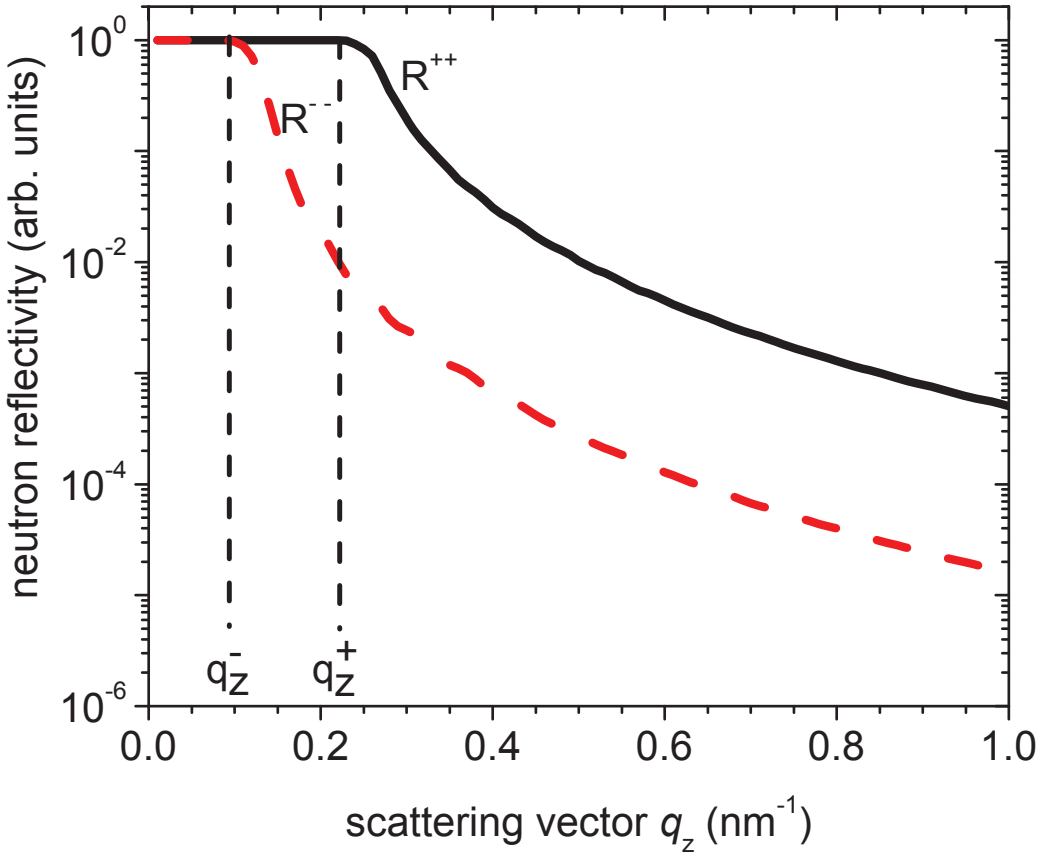

Figure 2.14. A polarized neutron reflectometry simulation for a 100 nm Fe film on a silicon substrate where the film has a moment of 2.2 μ_B / atom. The critical q-vectors q_z^- and q_z^+ are shown for the non-spin flip reflectivities, R(+ +) $=|r^{++}|^2$ (solid top curve) and R(– –) $=|r^{--}|^2$ (dashed bottom curve), respectively.

These simple geometric configurations illustrate the point that the spin-flip reflected amplitude gives a measure of the component of the in-plane magnetization that is perpendicular to the neutron spin, whereas the non-spin flip intensity is sensitive to the in-plane component that is parallel to the neutron spin.

The previous cases show how the reflectivities for a semi-infinite ferromagnetic film are affected by different field orientations. For a helical magnetic thin film, Simulreflec was used to model the helical magnetic structure of MnSi by treating the MnSi film as a series of individual ferromagnetic layers with a thickness of 0.2624 nm, whose moments gradually rotated from layer to layer about the film normal. An out-of-plane magnetic field would polarize the neutrons along the film normal, and therefore along the direction of the propagation vector for MnSi thin films (Fig. 2.15). This is the optimal geometry to investigate the magnetic structure of the MnSi(111) films since the neutron spin is perpendicular to all the moments in the helix and will therefore give the largest spin-flip reflectivity. A Simulreflec simulation of a 35.2-nm thick MnSi film with a wavelength of 18 nm on a Si substrate is shown in Fig. 2.16. The simulation of the magnetic structure of the film consists of 134 layers, each layer 0.2624 nm thick. The simulation is of a right-handed helix and a magnetic Bragg peak (shown by the arrow) is observed in only one of the spin channels. A right-handed helix produces a peak in the down-flipped spin signal R(+ −), at a scattering vector equal to the propagation vector q_z = 0.35 nm^{-1}, whereas for a left-handed helix, this is found in R(− +).

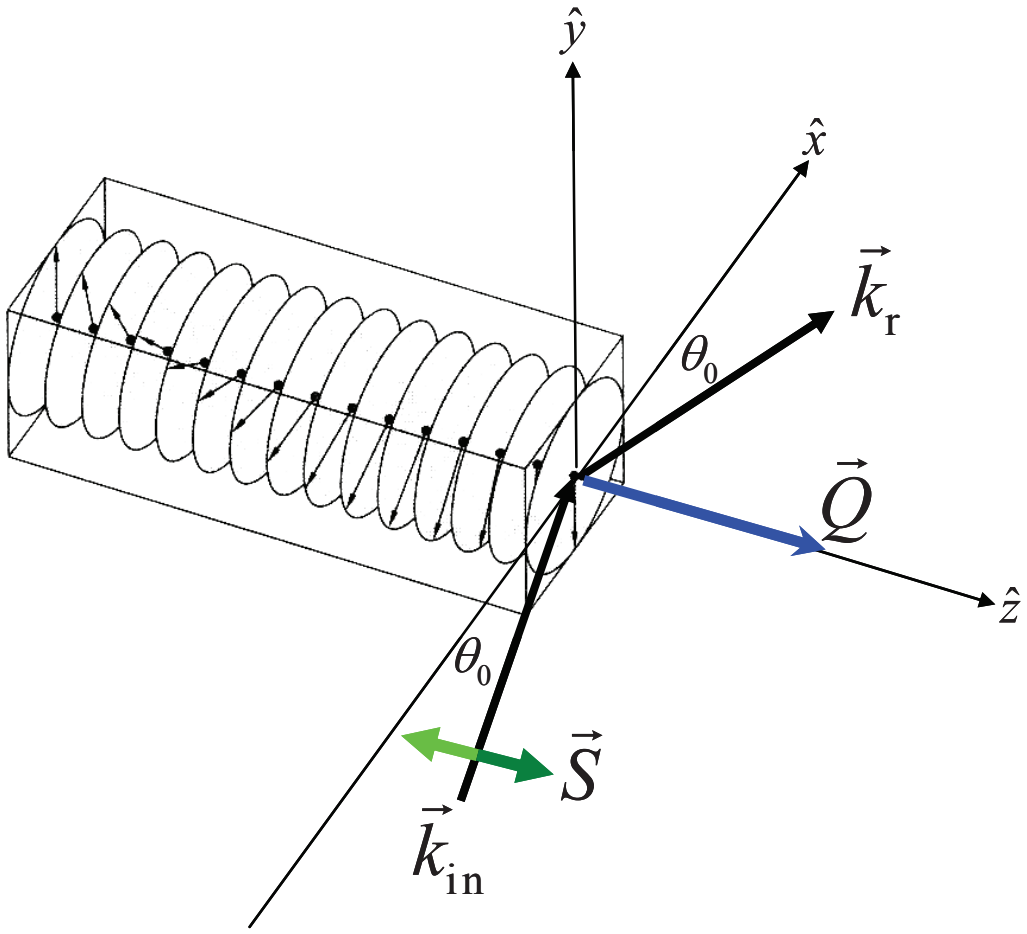

Figure 2.15. A schematic diagram showing the non-conventional PNR geometry where the magnetic field and the neutron spins are parallel with the film normal in order to maximize the spin-flip signal containing the information about chirality. The film is shown with a right-handed spin density wave about the *Q* vector

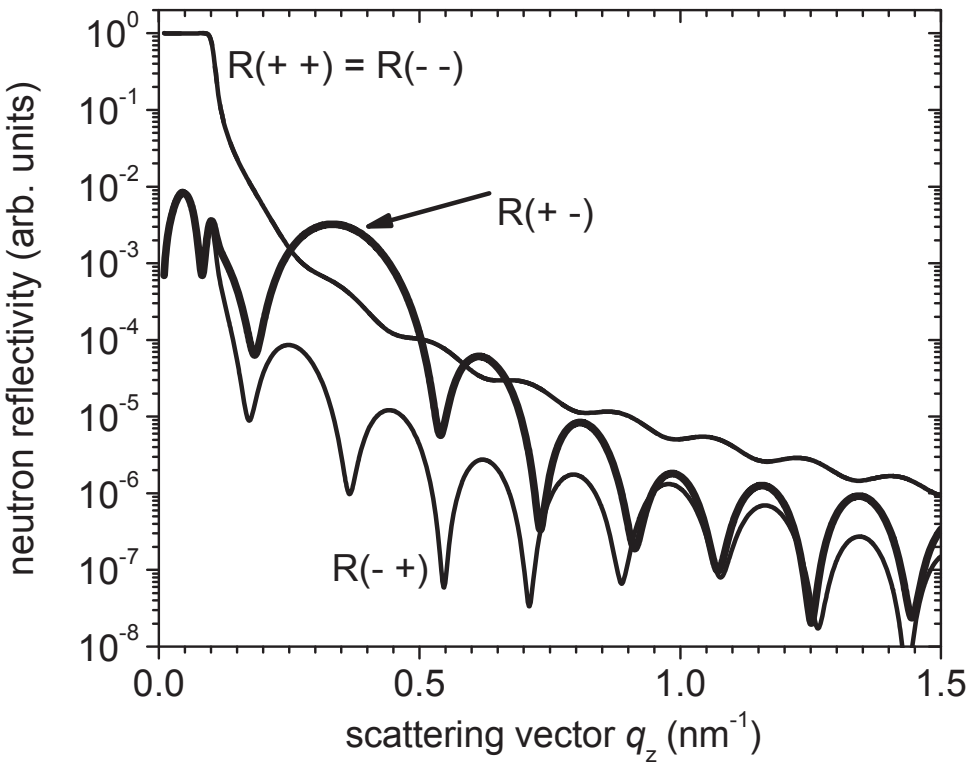

Figure 2.16. A Simulreflec simulation of a 35.2-nm thick MnSi film with a wavelength of 18 nm on a Si substrate. The simulation is of a right-handed helix and a magnetic Bragg peak (shown by the arrow) is observed in the R(+ –) spin flip channel at a $q_z = Q = 0.35$ nm^{-1}. For a left-handed helix, the magnetic Bragg peak is observed in the R(– +) spin flip channel.

2.6 Subtraction of Magnetic Background Due to Silicon Substrate

The magnetic properties of the MnSi films were studied by SQUID magnetometry. The magnetic signal at high field intensity was dominated by the diamagnetic response of the substrate. Since the critical field H_{C2} is approximately 1 T for MnSi thin films, the contribution of the substrate to the measured moment was determined from a linear fit to the $M - H$ data above a field of 3T, as shown in Fig. 2.17.

At low temperatures and fields above 0.6 T, the magnetization in bulk MnSi increases linearly with a high field susceptibility of χ_{HF} = 1.69 kA/mT and does not saturate below an applied field of 14 T [25]. This increase in magnetization is small compared to the high field magnetization of 163 kA/m observed in the thin film samples and was therefore neglected. This correction to the data underestimates the susceptibility of the substrate. However, the correction from χ_{HF} is only 2% in an applied field of 2 T and has no affect on the measurement of the remanent magnetization M_r. The saturation magnetization M_{sat} was obtained by extrapolating the slope of the hysteresis curve between 3 – 5 T to H = 0, and therefore is also independent of any correction due to χ_{HF}.

The SQUID measures the total magnetic moment of the sample. The magnetization is obtained by dividing the moment by the volume of the sample. The area of the sample was measured with a digital calliper and the thickness was determined from the XRD and XRR measurements, as described in Section 2.3 and 2.4.1, respectively.

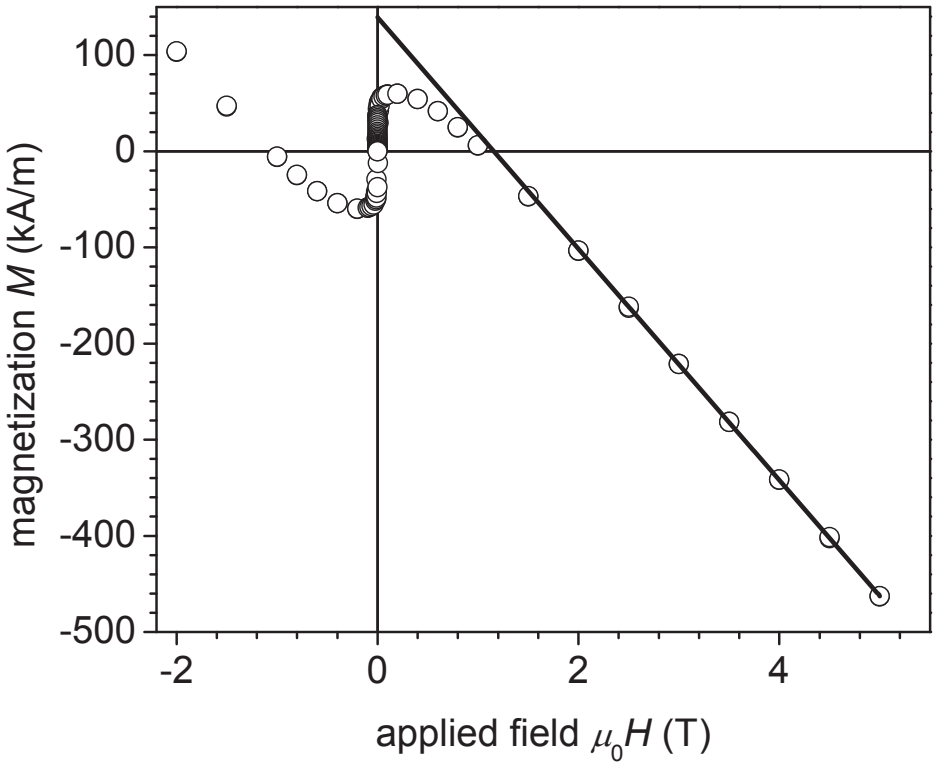

Figure 2.17. The large diamagnetic response of the Si substrate gives a linear background to the measured $M - H$ curves of a 6-nm sample at a temperature of 5 K. M_{sat} is obtained from extrapolating the slope of the hysteresis curve between 3 – 5 T to H = 0.

Chapter 3 – MnSi Films Grown by Solid Phase Epitaxy

Various research groups have used SPE as a technique to explore the growth properties of epitaxial MnSi thin films on Si(111) in order to generate smooth defect free thin films, as described in Chapter 1 [24, 43 – 51]. Since the magnetic properties of MnSi thin films have been largely unexplored [52] [53], an investigation was performed on the structural and magnetic properties of epitaxially grown MnSi thin films. In Chapter 3, a correlation is shown between the magnetic and structural properties of epitaxial MnSi(111) thin films grown by SPE on Si(111) substrates. The lattice mismatch between the film and the substrate lead to an in-plane tensile strain found in the film, which was partially relaxed due to the presence of misfit dislocations. However, the out-of-plane strain has an unusual strain dependence with thickness that is the result of changes in the elastic constants of the film. A strong correlation between T_C and κ / c_{44} as a function of thickness suggests that the changes in the elastic constants and T_C with thickness have a common origin that maybe due to interstitial defects resulting from SPE. A glassy magnetic behaviour was observed in the MnSi films and plane-view TEM images provided evidence that both left and right-handed domains are present in the MnSi films due to the noncentrosymmetric crystal structure of MnSi. The glassy magnetic behaviour is a result of disorder and frustration in the films where the disorder arises from the distribution of inversion domains and defects, and the frustration arises from the inversion domain boundaries.

3.1 Optimal Growth Conditions

An effusion cell in the UHV chamber evaporated amorphous Mn films onto clean Si(111) wafers at RT, which were transformed into crystalline MnSi films by annealing in UHV at 400 °C. The sample was monitored with RHEED until a $\sqrt{3}\times\sqrt{3}$ RHEED pattern appeared, characteristic of a MnSi(111) film on Si(111) [47]. The MnSi films grown by SPE ranged from a thickness of 0.68 nm to 21.0 nm. After cooling the films to RT, a 6-nm protective layer of amorphous Si was deposited onto the film surface on the first series of samples, but the thickness of the Si capping layer was increased to 20 nm for subsequent samples. *Ex-situ* x-ray photoelectron spectroscopy (XPS) measurements determined that a native oxide layer, approximately 2.2 nm thick, was present on the samples. Performing *ex-situ* XRR measurements, the MnSi films were confirmed to be twice the thickness of the initial amorphous Mn films.

MnSi exists within a very narrow region of the MnSi phase diagram shown in Fig. 3.1. The SPE grown samples were annealed at various temperatures and annealing times to determine the optimal growth conditions for the MnSi thin films. For samples grown at too cool a temperature, or too short an annealing time, XRD measurements show the coexistence of Mn_5Si_3 and MnSi in the samples. Evidence of a broad peak of the Mn rich phase with a peak at $2\theta_0$ = 37.8º near the unstrained bulk value Mn_5Si_3(002) of $2\theta_0$ = 37.38º is shown in Fig. 3.2, in addition to an out-of-plane compressively strained MnSi(111) peak at $2\theta_0$ = 34.17º. Kiessig fringes observed on either side of the MnSi(111) peak are consistent with a smooth surface despite the additional Mn rich

phase co-existing with the MnSi phase. *Ex-situ* rapid thermal annealing the sample for 2 hours at 400 ºC in an argon atmosphere removed the Mn_5Si_3 from this sample. The increased amplitude of the MnSi(111) peak and the increased oscillation amplitude of the Kiessig fringes surrounding the peak after the disappearance of the Mn_5Si_3 peak are consistent with a decrease in the interfacial roughness of the film.

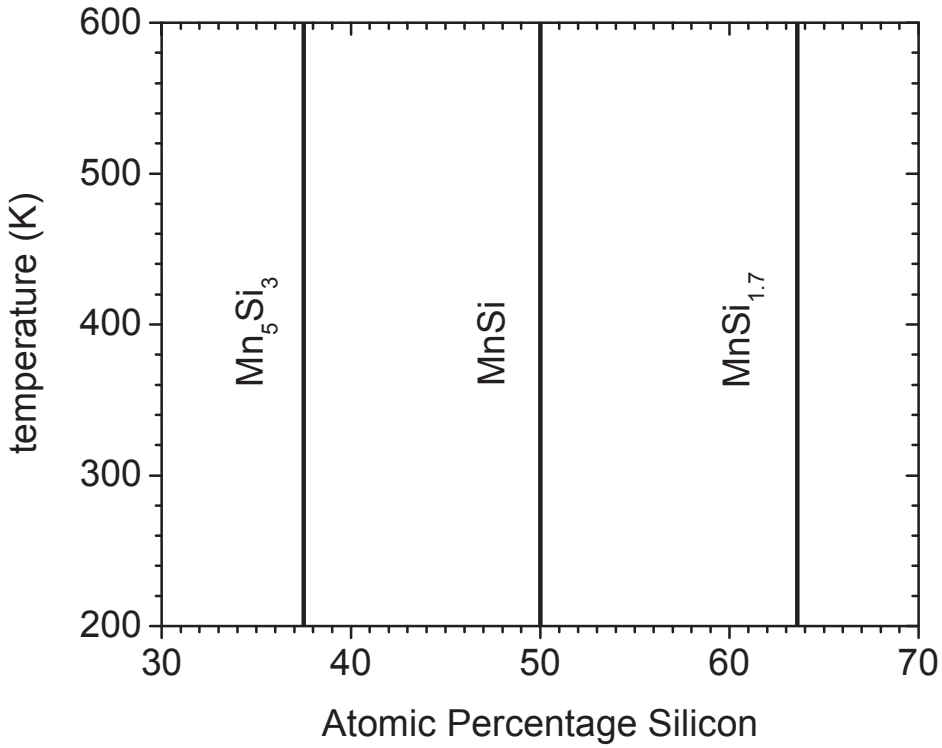

Figure 3.1. MnSi phase diagram. MnSi only occurs over a very narrow region in the MnSi phase diagram and is sensitive to the ratio of Mn to Si. Mn rich Mn_5Si_3 or Si rich $MnSi_{1.7}$ can form [67].

.

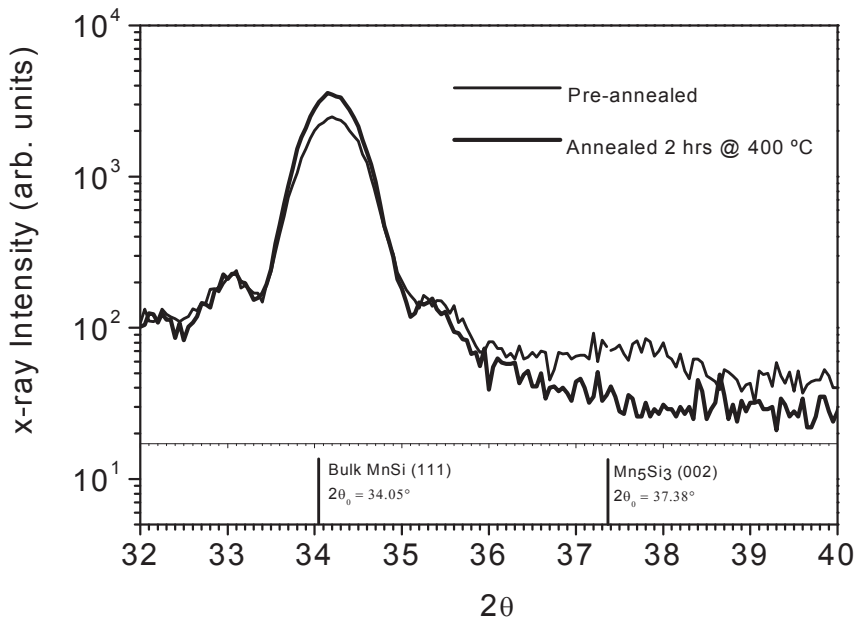

Figure 3.2. XRD results from a strained Mn_5Si_3 (002) at $2\theta_0$ = 37.8º peak in addition to the strained MnSi(111) peak at $2\theta_0$ = 34.17º. *Ex-situ* annealing removes Mn_5Si_3 from the sample, as observed by the disappearance of its $2\theta_0$ peak. Bulk unstrained peak angles are shown by the lower bar graph.

Annealing for either too long or too hot allowed the MnSi film to continue to react with the Si substrate to form $MnSi_{1.7}$ "fingers" within the MnSi film until the MnSi completely transformed into $MnSi_{1.7}$ [68]. After a 9-nm thick Mn layer was deposited onto a Si(111) wafer at RT and annealed at a temperature of 400 ºC for 14 hours, XRD measurements showed evidence of multiple $MnSi_{1.7}$ peaks coexisting with a MnSi(111) peak, as shown in Fig. 3.3. Additional MnSi peaks with different crystal orientations were also observed.

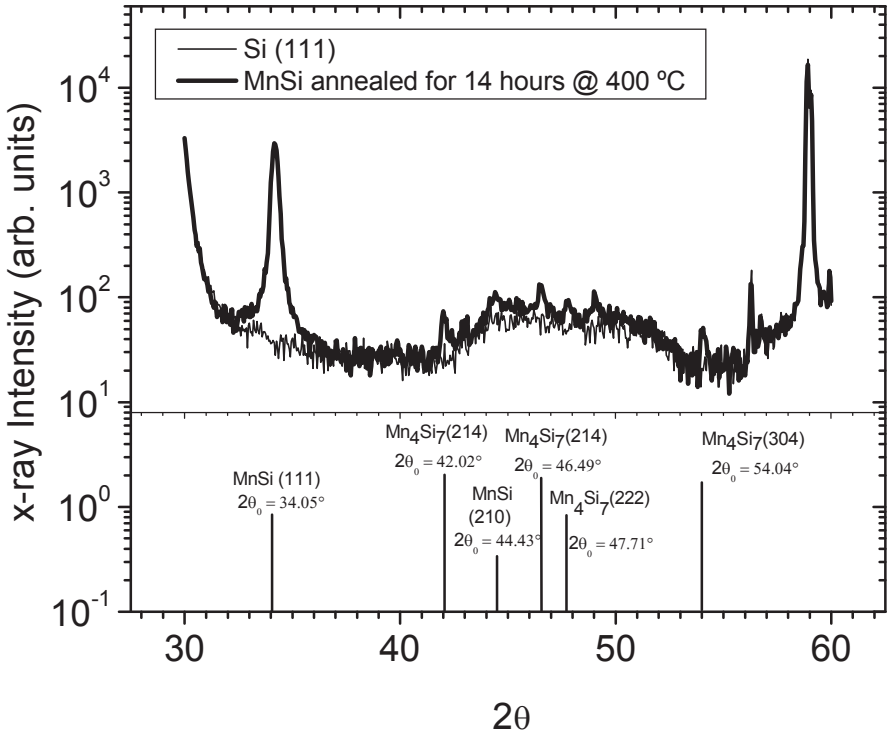

Figure 3.3. A MnSi(111) peak and multiple orientations of $MnSi_{1.7}$ appear with the deposition of 18 nm of Mn on a Si(111) substrate annealed @ 400 ºC for 14 hours. Data compared with a clean Si(111) substrate. Bulk unstrained peak angles are shown by bar graph.

Fig. 3.4 shows an XRD scan of a smooth 5.0-nm MnSi thin film after an *in-situ* anneal at 400 ºC as indicated by the appearance of Kiessig oscillations. When the sample was annealed at 500 ºC for 1.5 hours, the MnSi film was completely transformed into $MnSi_{1.7}$.

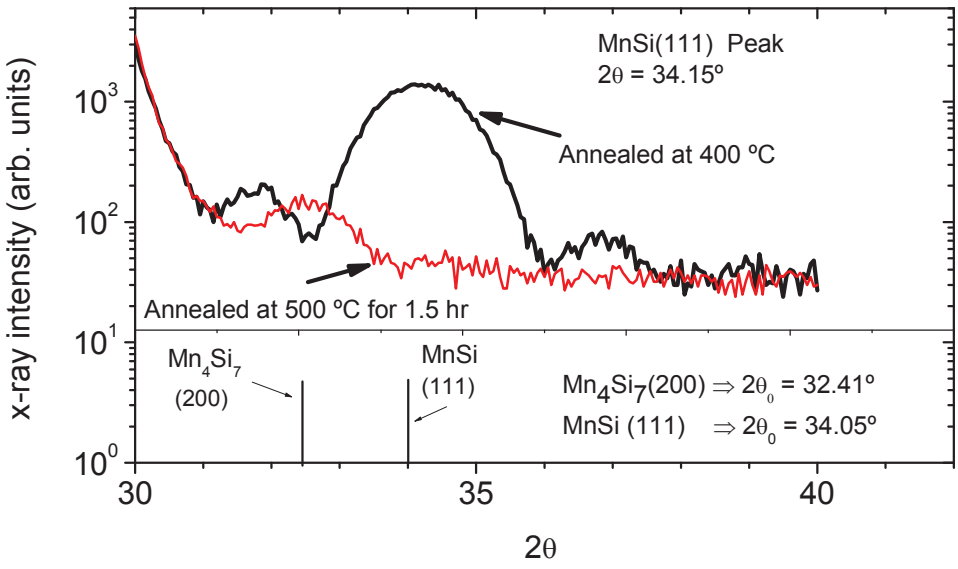

Figure 3.4. MnSi(111) peak shown for a 5.0-nm thin film grown by SPE at 400 ºC, shown after *ex-situ* annealing at 400 ºC. Annealing at 500 ºC, transforms the MnSi into $MnSi_{1.7}$. Bulk unstrained peak angles are shown by bar graph.

3.2 Film Thickness Determination

Both XRR and XRD were performed on the SPE grown samples to determine MnSi film thickness. Simulreflec modelling software was used to fit the specular component of the XRR measurements [66]. The data in Fig. 3.5 was obtained by subtracting the diffuse scattering contribution, estimated by performing a $\theta_0 - 2\theta_0$ scan with a $\Omega = 0.18º$ offset, from the specular $\theta_0 - 2\theta_0$ measurement ($\Omega = 0º$).

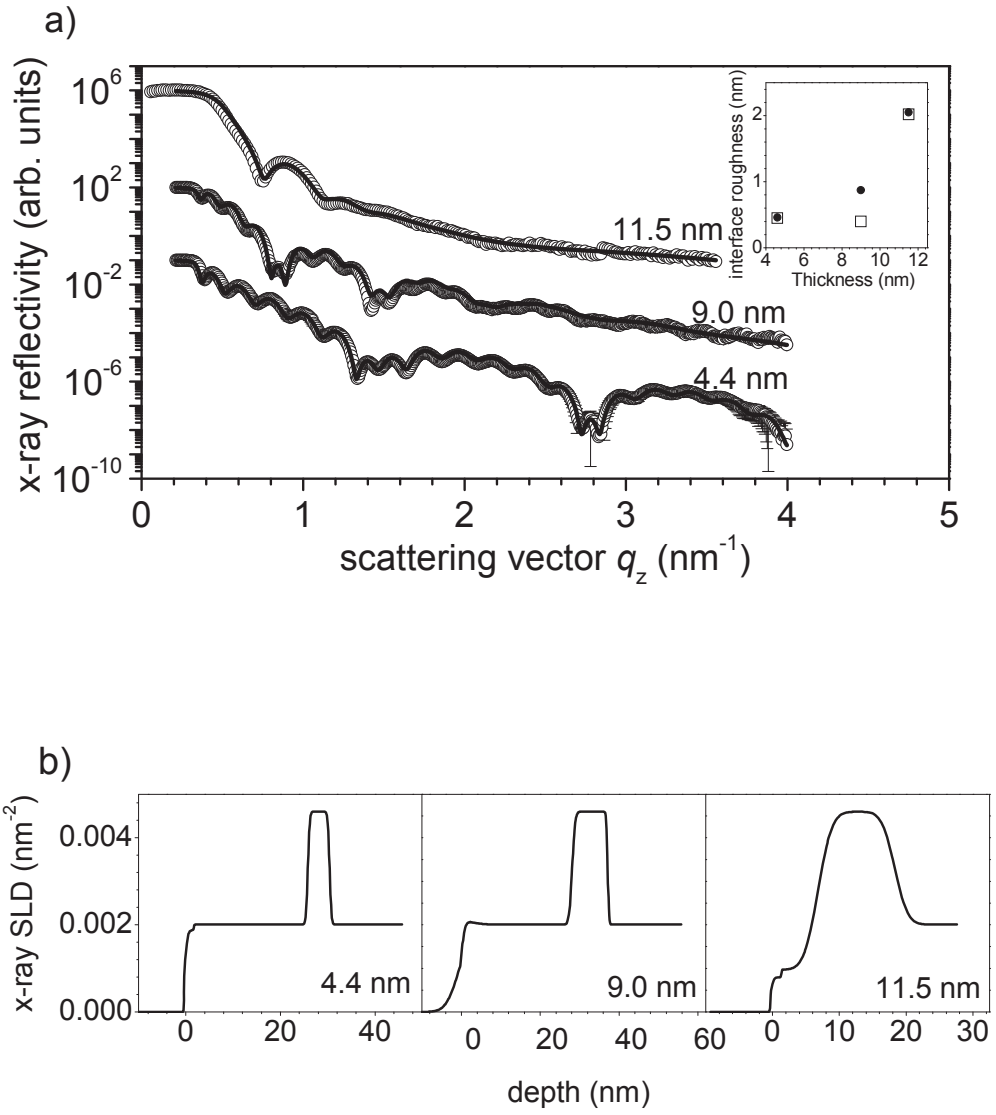

Figure 3.5. a) XRR curves of films grown by SPE. The solid lines represent fits to data obtained from the SLD profiles. Inset in a) are RMS-roughness values obtained from the fits to the data. The open squares show the interface roughness between the film and substrate and the filled circles represent the roughness at the film-cap interface. b) SLD profiles for the MnSi films. The thicknesses are obtained from the fits and displayed next to each curve.

In Fig. 3.5 (a), XRR data is shown with fits for 3 representative samples that range in thickness from 4.4 nm – 11.5 nm. The short wavelength oscillations clearly seen on the 4.4-nm and 9.0-nm samples are due to the thickness of the amorphous silicon-capping layer. The long wavelength oscillations, related to the MnSi film thickness, become shorter with increasing film thickness. At a film thickness of 9.0 nm, the observed oscillations at higher q weaken in amplitude and almost completely wash out at a thickness of 11.5 nm due to interfacial roughness. Fig. 3.5 (b) shows the fits generated from the scattering length density (SLD) profiles. The sharp interfaces observed for the 4.4-nm thin film indicate a smooth film. The interface roughness can be observed in the SLD plots in Fig. 3.5 (b). Unlike the other two samples with a 20-nm thick protective cap, the 11.5-nm sample has a 6-nm thick capping layer. The drop in the SLD of the Si capping layer for the 11.5-nm sample is due to interface roughness.

Since XRR fits are not necessarily unique, the model was tested with fits to the MnSi(111) XRD peak. The same 3 representative samples shown in Fig. 3.5 are shown in Fig. 3.6. Fits to the Kiessig fringes of the MnSi(111) peak in Fig. 3.6 confirmed the thicknesses extracted from XRR. The observation of Kiessig oscillations surrounding the MnSi(111) peak of the 5-nm sample is consistent with the existence of sharp MnSi/Si interfaces. The width of the Kiessig fringes narrowed and the amplitude of these oscillations decreased and, almost completely vanished at 11.5 nm, as shown in Fig. 3.6.

Although the 9.0-nm and 11.5-nm XRD and XRR thickness measurements agree, there is a 0.6-nm discrepancy between the measurements of the thickness of the thinnest film shown in Fig. 3.5 and Fig. 3.6. From the XRR model, the thinnest MnSi film has a thickness of 4.4 nm. There is a difference because the XRR model includes an

interfacial region between the MnSi and the substrate that is 0.5 nm thick and has an SLD that is lower than the x-ray scattering length density of MnSi by a factor of 0.7. A mixture of Si and MnSi regions in this layer accounts for this lower density. Adding these layers together, the total MnSi thickness agrees with the thickness determined by the

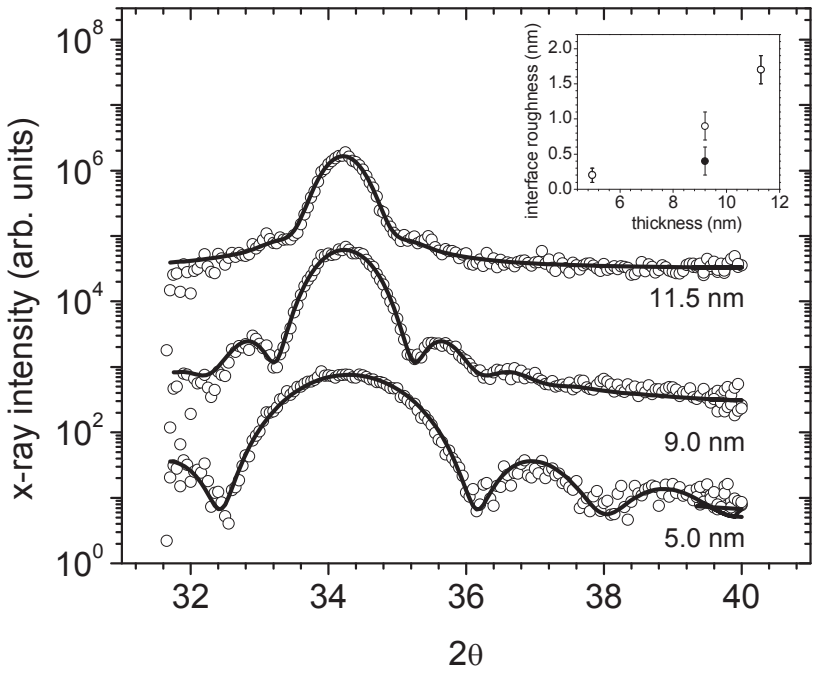

Figure 3.6. XRD of the MnSi(111) peak for the same 3 samples shown in Fig. 3.5. The solid line represents the fit to the data using Eq. (2.4) and the thicknesses extracted from the fit are shown next to each curve. The inset shows the interfacial roughness at the lower film boundary (solid circles) and at the upper boundary (open circles) obtained from the fits. Error bars are ± 1 standard deviation (σ).

XRD model. Although the XRD model can fit the thickness of the film, the model cannot determine the density differences near the film interfaces, which the XRR modelling software can determine. In addition, the XRD model used to fit the data is insensitive to the interfacial roughness, which has a measured uncertainty of approximately ± 0.2 nm due to the incoherent scattering present in the films.

For films thicker than 11.5 nm, the large interfacial roughness of the films prevented good fits to the XRR data. Since the thickness extracted from XRR and XRD measurements at lower films agreed well with Mn flux monitor readings (see Chapter 2, Fig. 2.3), the thickness was estimated with Mn flux measurements for films thicker than 11.5 nm.

3.3 Film Strain Measurements

An in-plane tensile strain, in the films, measured by transmission electron microscopy, was observed due to the lattice mismatch between the MnSi(111) thin films and the Si(111) substrates. Plan-view TEM specimens were prepared by low-angle mechanical polishing and imaged with a Philips CM30 TEM [69]. The in-plane strain for the SPE grown samples was measured using [111] zone axis TEM plan-view selected area diffraction patterns (Fig. 3.7 (a)) and was found to partially relax with increased film thickness. Partial relaxation of the strain leads to fine structure in the diffraction spots. The fine structure arising from double diffraction is shown in Fig. 3.7 (b) consists of a central spot surrounded by six symmetrically oriented spots. Double diffraction occurs when each MnSi diffracted spot acts as a source electron beam for the Si crystalline

substrate and generates a complete Si[111] zone-axis diffraction pattern for each MnSi spot.

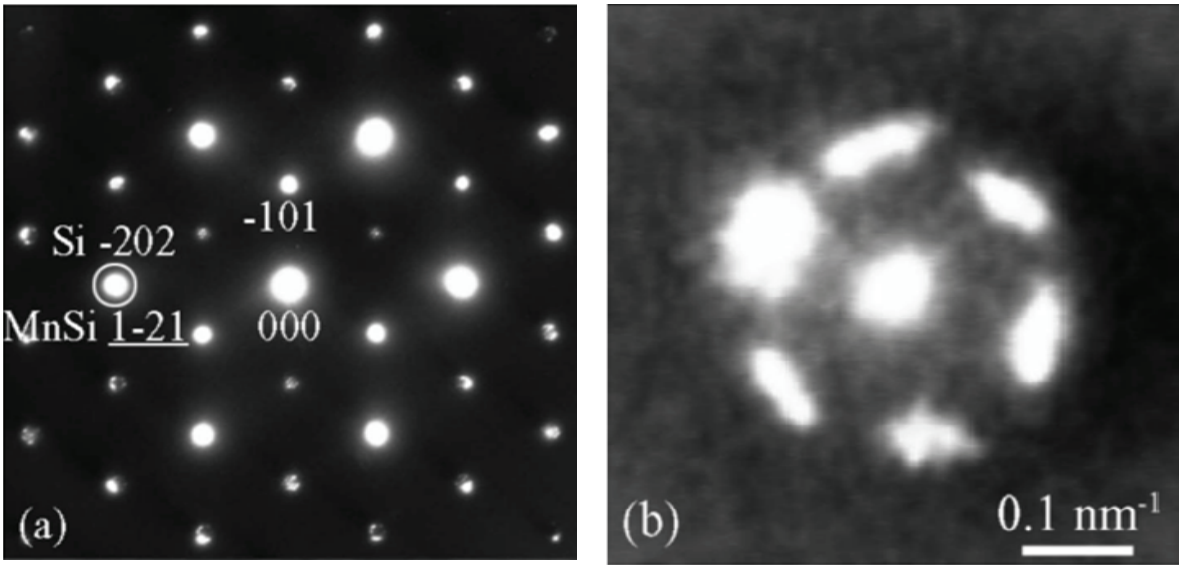

Figure 3.7. a) Plan-view SADP of an 11.5-nm thick MnSi layer on a Si substrate at the [111] zone-axis orientation. b) The fine structure within the diffraction spot circled in a). (Images courtesy of Prof. M.D. Robertson, Acadia University)

The following relationship

$$\varepsilon_{\parallel}(\%) = 3.0\% - 100\% \frac{\Delta g}{g_{ref}}, \tag{3.1}$$

determined the in-plane strain, where Δg is the reciprocal distance between the fine structure's centre spot and outer ring of spots and g_{ref} is the inverse distance between the (000) spot and one of the Si{220} spots. This method was used to quantify the relaxation of the in-plane strain as a function of MnSi layer thickness and corresponds to the data points shown in Fig. 3.8 (a) [70].

Cross-sectional high-resolution TEM (HRTEM) images obtained using a 300 kV aberration corrected FEI Titan Cubed TEM (Fig. 3.9), of the films show that the

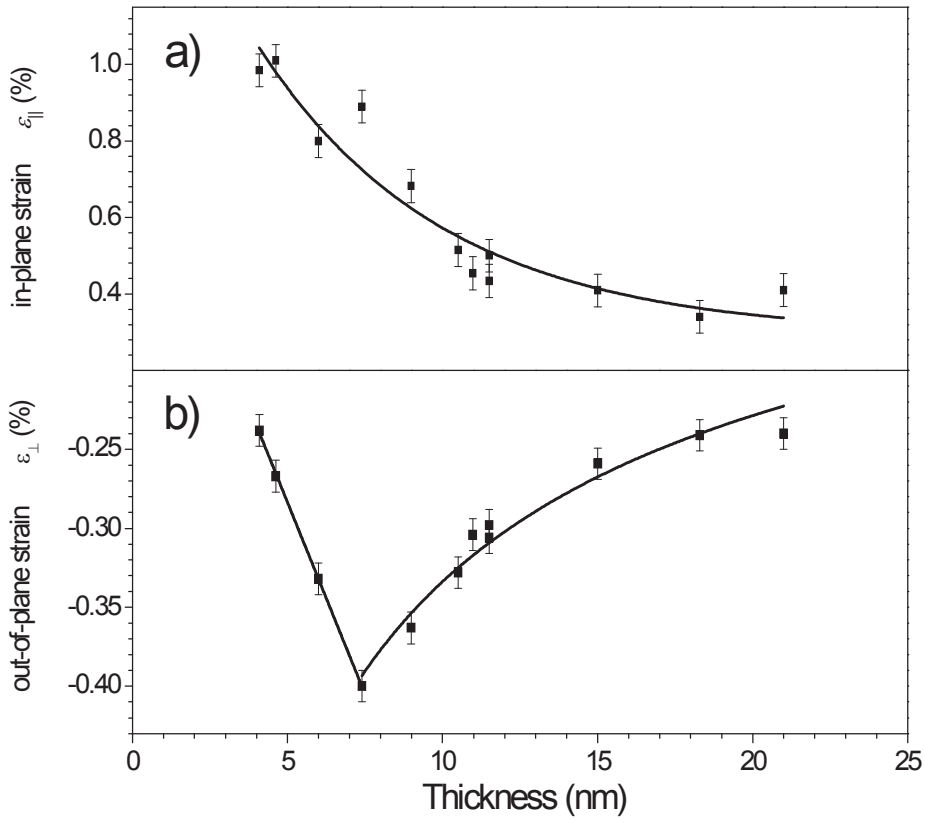

Figure 3.8. a) The in-plane strain measured by TEM plan-view selected area diffraction patterns as a function of thickness. b) The out-of-plane strain measured by XRD. Error bars are ± 1σ.

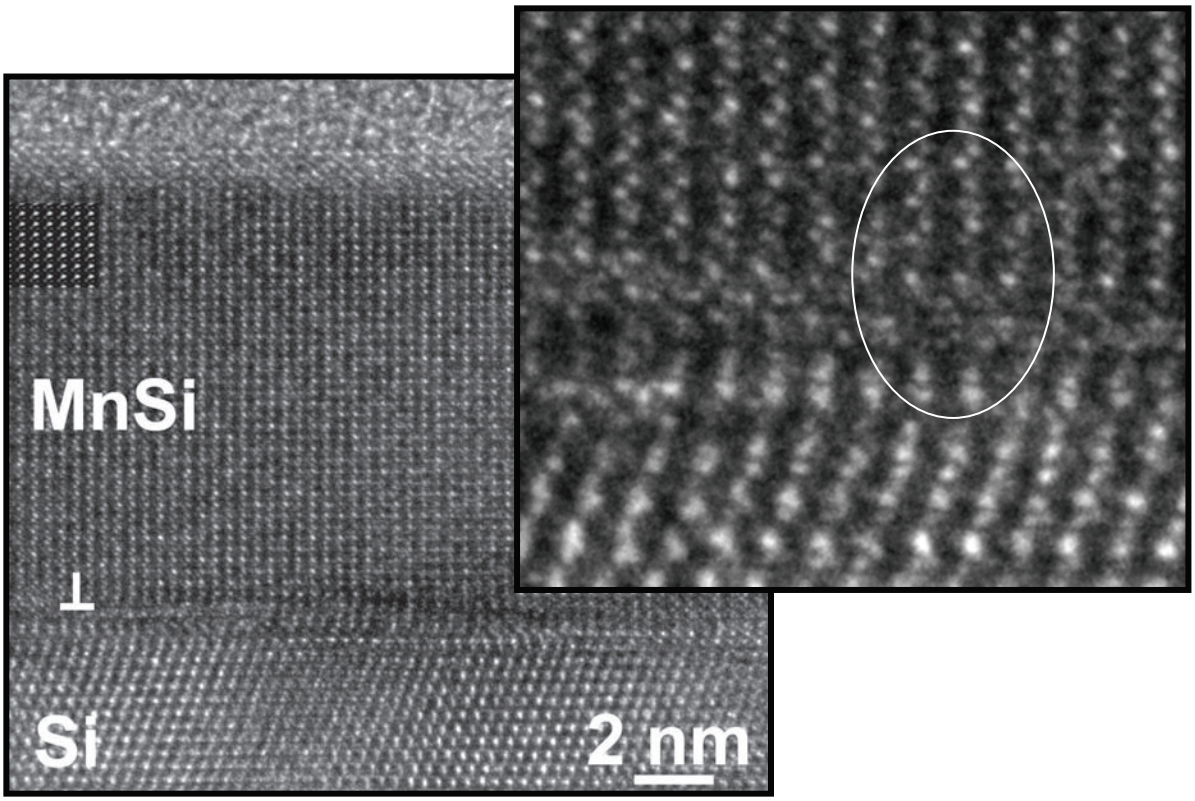

Figure 3.9. HRTEM cross-sectional image shown on the left of an 11.5-nm thin film grown by SPE. The image on the right is a blow-up of the film that shows strain partially relieved by edge misfit dislocations shown in circle. (Images courtesy of Prof. M.D. Robertson, Acadia University)

strain in the films is partially relaxed by misfit dislocations. The in-plane tensile strain induces an out-of-plane compressive strain through the Poisson effect. The out-of-plane compressive strain measured by XRD had an unusual strain dependence with respect to film thickness, as shown in Fig. 3.8 (b). An increase in the magnitude of the out-of-plane strain up to a 7-nm thickness is observed before the out-of-plane strain

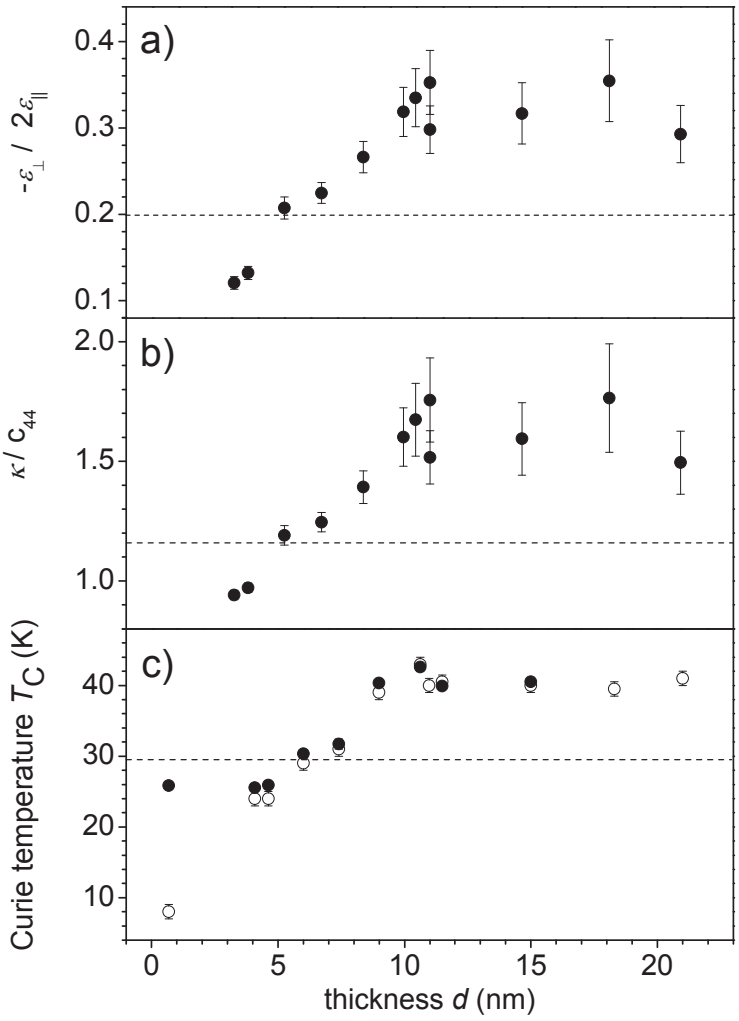

Figure 3.10. a) Ratio of the strains $-\varepsilon_\perp / 2\varepsilon_\parallel$ as a function of thickness with ± 1σ error bars. b) Ratio of compressibility to the shear elastic constant c_{44} as a function of thickness. Dashed lines in a) and b) indicate expected values from bulk elastic constants. c) Curie temperature as a function of film thickness determined from remanent magnetization measurements (open circles) and from field cooled magnetization measurements (solid circles) in an applied field of 10 mT. Bulk Curie temperature of 29.5 K shown by the dashed line.

begins to relax. In order to understand the behaviour observed from the out-of-plane strain measurements, the strain ratio $-\varepsilon_{\perp} / 2\varepsilon_{\parallel}$ was plotted as a function of thickness in Fig. 3.10 (a). Since this strain ratio should be a constant given by Eq. (1.26) derived in Chapter 1. By using the elastic stiffness constants for bulk MnSi in Eq. (1.26), c_{11} = 283.3 GPa, c_{12} = 64.1 GPa, and c_{44} = 117.9 GPa [71], the strain ratio of 0.20 was obtained, which differed from the value determined for the thin films in Fig. 3.10 (a). Films thicker than 10 nm, have an average strain ratio of 0.32 ± 0.01.

From Eq. (1.26), the ratio of the bulk modulus $\kappa = (c_{11}+2c_{12})/3$ to the shear elastic constant c_{44} as a function of thickness (Fig. 3.10 (b)) was calculated. A linear increase was observed in κ/c_{44} with increasing thickness, from 0.94 ± 0.02 for a thickness of 4 nm to an average value of 1.63 ± 0.04, for thicknesses ranging from 10 – 21 nm, as compared to the bulk value of 1.16. This behaviour could be due to either a softening of c_{44} or a stiffening of the bulk modulus κ. Due to the [111] orientation of the films, a softening c_{44} would contribute to a softening of the out-of-plane elastic stiffness constant $c'_{33} = (2c_{11}+2c_{12}+c_{44})/4$. Results obtained by Ogi *et al*. for Fe films on Si(100) showed a similar behaviour for κ/c_{44} and the out-of-plane strain $\varepsilon_{\perp}$ with respect to thickness [72]. Interstitial defects may be responsible for the behaviour observed in Fig. 3.10 (b). Dederichs *et al*. have shown that c_{44} of single-crystal Cu can decrease as much as 31% per atomic percentage of interstitials, with little effect on κ [73]. Therefore, a small atomic percentage of interstitials may be enough to cause the variations observed in Fig. 3.10 (b).

3.4 Effect of Strain on Film's Magnetic Properties

Since there was an unusual strain dependence of the elastic properties of the MnSi thin films, the effect of strain on the magnetic properties in the films was investigated. A Quantum Design MPMS-XL SQUID magnetometer was used to measure the magnetic properties of the thin films and configured with a longitudinal pick-up coil with applied dc fields oriented along the $[1\ \bar{1}\ 0]$ direction, unless otherwise specified.

Two different methods were used to determine the Curie temperature, as shown in Fig. 3.10 (c). In the first method, the remanent magnetization, M_r, shown by open symbols, was measured as a function of temperature on warming, after saturating the sample in a field of 5 T at 2 K. The temperature at which the magnetization drops to zero gives a measure of T_C. The Curie temperature was determined by using the knee in the M_r as a function of temperature and extrapolated the $M_r(T)$ data, from a few degrees below the knee, and assigned the T_C to the temperature where it dropped to the level of the background magnetization, which is approximately 100 A/m. The concave nature of the curves is due to the presence of magnetic domains in the samples. Since magnetic domains can obscure the measurement, T_C using power-law fits (shown by the thick solid lines in Fig. 3.11) was also determined to the $M(T)$ data in an applied field of 10 mT, close to T_C. A power law fit of the form $M(T) = M_T \left| 1 - T/T_C \right|^{\beta}$, where M_T is a scaling factor and β is a critical exponent, was used to determine T_C. A best value for T_C was determined by minimizing the error by iterating T_{max}, T_{min} and the reduced χ^2 per degree of freedom (DOF) over an interval close to T_C in order to achieve a best fit, where T_{max} is

the temperature where a broadening in the $M(T)$ data curve due to finite size was observed.

The Curie temperatures determined by both methods, shown in Fig. 3.10 (c), are in good agreement with one another, except for the 0.7-nm sample. The lower value determined from the remanent magnetization for the 0.7-nm sample may be due to the

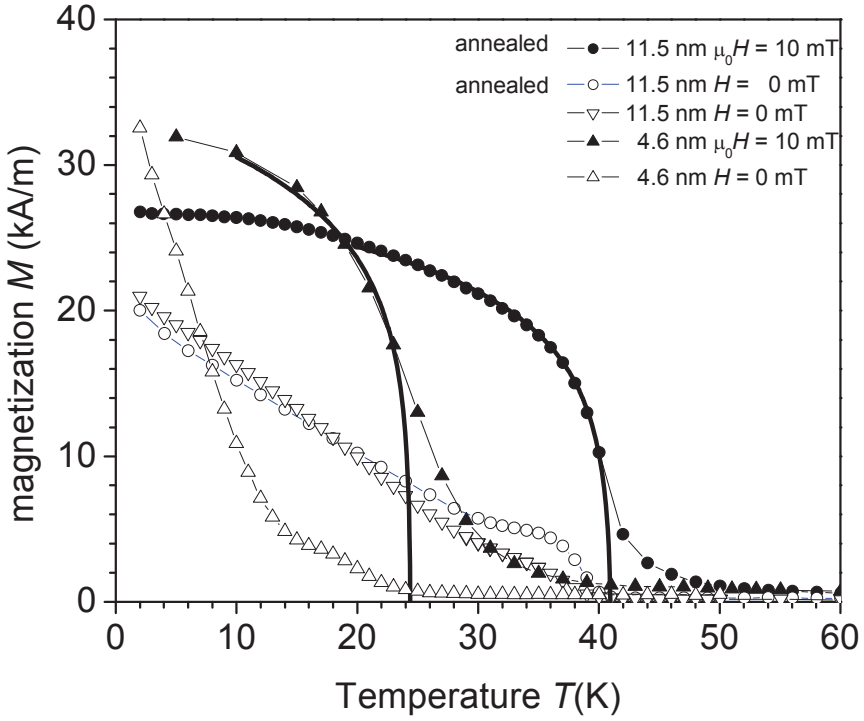

Figure 3.11. Remanent magnetization data of MnSi films, measured on warming the sample (open symbols). Field-cooled magnetization data (filled symbols) in a field of 10 mT, together with power-law fits, are shown by the thick solid lines. The annealed samples were heated *ex-situ* at 400 °C for 1.5 hours.

magnetic domain structure of the film dropping the remanent magnetization to zero at a temperature far below the real T_C. In Fig. 3.10 (c) the T_C reached a value as large as 43 K, which is 46% larger than the bulk value, $T_{C\,(bulk)} = 29.5$ K.

As the film thickness decreases below 9 nm, Fig. 3.10 (c) shows that T_C begins to drop. The T_C of magnetic thin films drops at low film thicknesses due to a reduction in the number of spin-spin interactions from the presence of the interfaces. However, the reduction in temperature observed in Fig. 3.10 (c) occurs over a 20-monolayer (ML) thickness range (1 ML = 0.263 nm, the bulk MnSi(111) plane spacing). This is larger than the measurements reported for Fe, Co, Ni [74, 75] and Gd [76] where the reduction in temperature occurred over a thickness range of 2.2 ML for Co, 2.3 ML for Fe, 4.7 ML for Ni and 8.6 ML for Gd [75].

Although the films are under biaxial stress, the MnSi thin film measurements were compared with bulk MnSi measurements under hydrostatic pressure in order to separate finite size effects from the effects of strain. Although hydrostatic pressure experiments in bulk are fundamentally different from the biaxial strain present in the films, changes in band structures under hydrostatic strain and biaxial strain are comparable for materials with a small Poisson ratio and therefore changes in the magnetism should follow similar strain dependence. Density functional calculations of GdN indicate that changes in band structure are similar for both hydrostatic and biaxial stress due to a small Poisson ratio of 0.2 [77], whereas the Poisson ratio for bulk MnSi is $v = c_{12} / (c_{11}+c_{12}) = 0.185$ [71].

Pressure dependence results reported by Pfleiderer *et al*. [78] were converted into volume strain values $\Delta V / V$ using the bulk modulus of $\kappa = (c_{11}+2c_{12}) / 3 = 137$ GPa

reported by Shistov *et al*. [71], which results in the plot shown in Fig. 3.12 (a). Pfleiderer *et al*. [78] fit the Curie temperature by using Moriya's spin fluctuation theory, $T_C \sim (p_c - p)^{3/4}$. This was used to extrapolate the bulk data to positive strain, which gave an

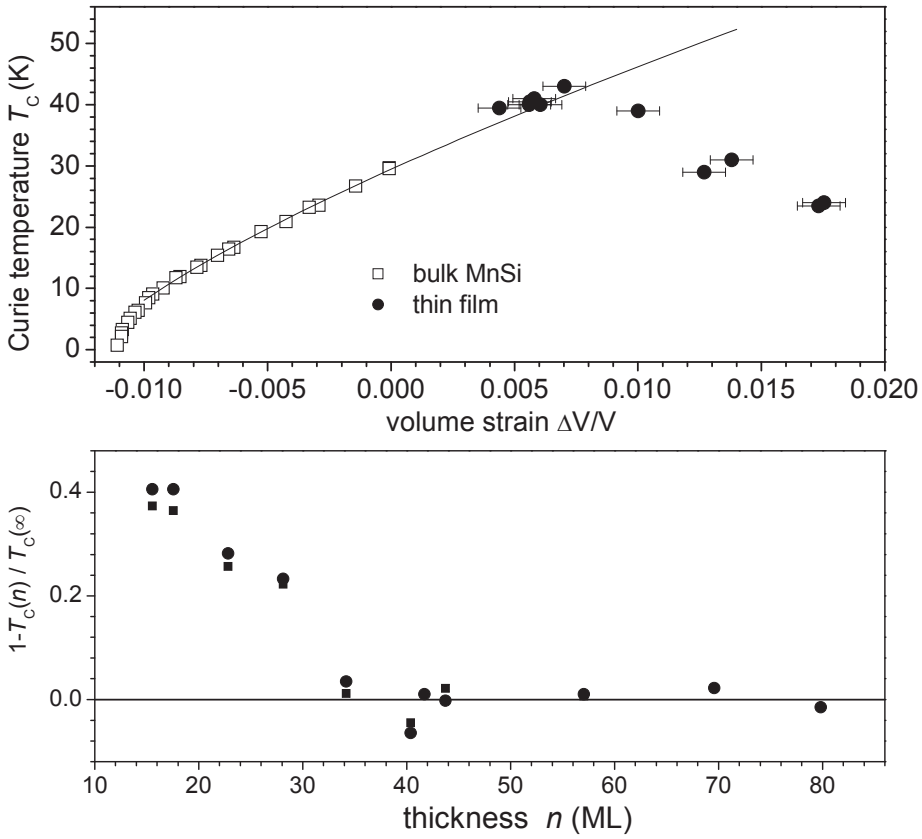

Figure 3.12. a) The dependence of Curie temperatures on volume strain in MnSi thin films and in bulk MnSi. The bulk values are taken from [78]. The curve is an extrapolation of a fit to the bulk data using spin-fluctuation theory [78]. b) The normalized difference between the expected thick film T_C (∞) and the measured T_C (n).

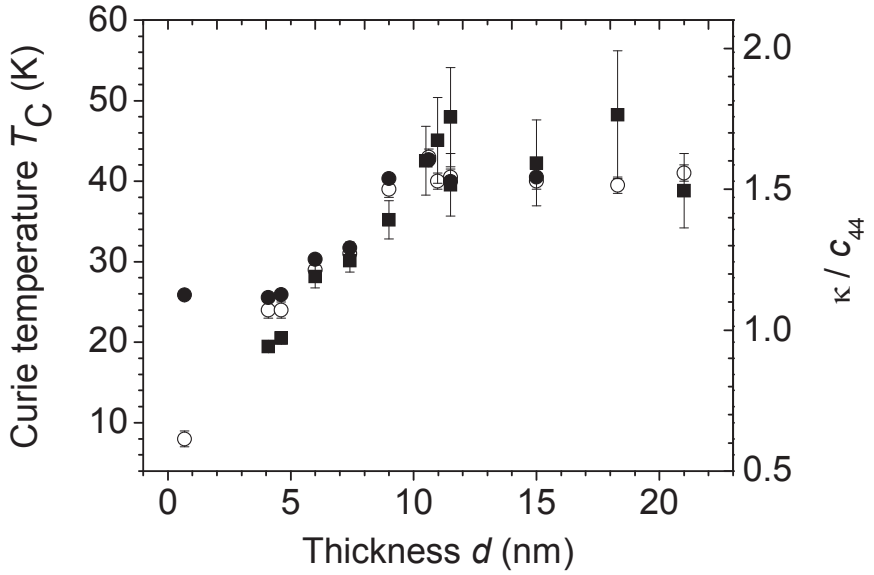

Figure 3.13. A strong correlation between T_C (circles) and κ / c_{44} (solid squares) as a function of thickness suggests that the drop in the elastic constants and T_C have a common origin. T_C as a function of film thickness determined from remanent magnetization measurements (open circles) and from field cooled magnetization measurements (solid circles) in an applied field of 10 mT.

estimate of T_C in the infinitely thick film limit. As seen in Fig. 3.12 (a) the extrapolation of the bulk data gave a good fit to the T_C of the films for thickness greater than 10 nm, which had a volume strain, $\Delta V / V < 0.007$. Figure 3.12 (b) shows the deviation of T_C (*n)* of the film with *n* monolayers from the Curie temperature $T_C(\infty)$ expected from the thick film limit. The T_C as a function of the number of monolayers, *n* was plotted in order to compare the results with those reported by Zhang and Willis on ferromagnetic thin films. The range of the exchange interaction would therefore determine the thickness range over

which a reduction in T_C is observed. However, this model would require the spin-spin interactions in MnSi to extend over 20 ML to explain the slow linear decay in $1-T_C(n)/T_C(\infty)$, which is much larger than the values reported for Co (2.2 ML) , Fe (2.3 ML) , Ni (4.7 ML) and Gd (8.6 ML) mentioned earlier [75].

The strong correlation between the thickness dependence of T_C and κ / c_{44} shown in Fig 3.13 suggests that the changes in the elastic constants and T_C with thickness have a common origin. Si or Mn interstitials that result from solid-phase epitaxy may be responsible for the strong correlation, since interstitial defects are also known to have a large effect on the T_C of magnetic materials [79], in addition to softening c_{44}, as discussed in Section 3.3. In an attempt to change the distribution of defects in the sample, the 11.5-nm film was annealed *ex-situ* at 400 ºC for 1.5 hours in an argon atmosphere. Longer annealing times were avoided to prevent the formation of higher silicides. Although changes were observed in the shape of the M_r (T) curves as shown in Fig. 3.11, annealing did not change the T_C significantly. It is also worth pointing out that the extrapolation of the bulk data with the results of spin-fluctuation theory is valid only for small deviations from the critical pressure. These results call for further theoretical work in order to understand the expected dependence of T_C on pressure for positive volume strain.

3.5 Magnetic Structure of SPE Grown Films

In order to understand the magnetic structure of the thin films grown by SPE, the $M-H$ hysteresis curves generated from the SQUID magnetometer measurements were analyzed. $M-H$ measurements were performed in both the in-plane $[1\,\bar{1}\,0]$ and out-of-

plane [111] orientations, and the shape of the $M - H$ curves was found to be qualitatively similar to data reported by Bloch *et al*. and Koyama *et al*. for bulk crystals with helical magnetic order [25, 35]. In Fig. 3.14, the applied field was oriented out-of-plane (open circles) with respect to the film (parallel to the direction of the easy axis for the propagation vector $\vec{Q}$ for bulk MnSi). In this orientation the magnetization increased

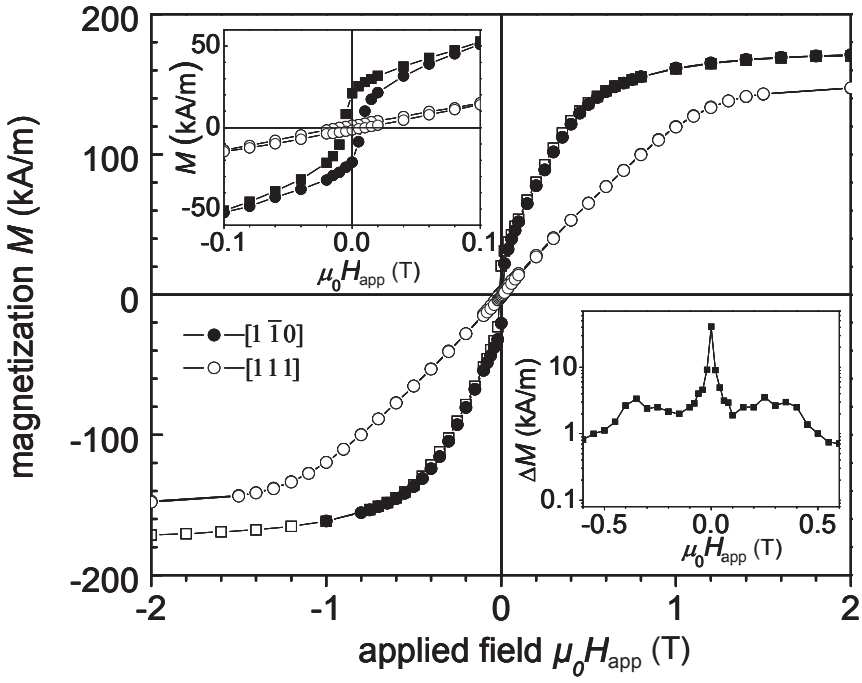

Figure 3.14. $M - H$ loops measured at 5 K for an 11.5-nm thick sample. The upper inset shows the magnetization between $\mu_0 H_{app} = -0.1$ and 0.1 T. The lower inset is the difference between the in-plane $M - H$ curves for increasing and decreasing field, which shows that the hysteresis extends to fields of approximately 0.5 T.

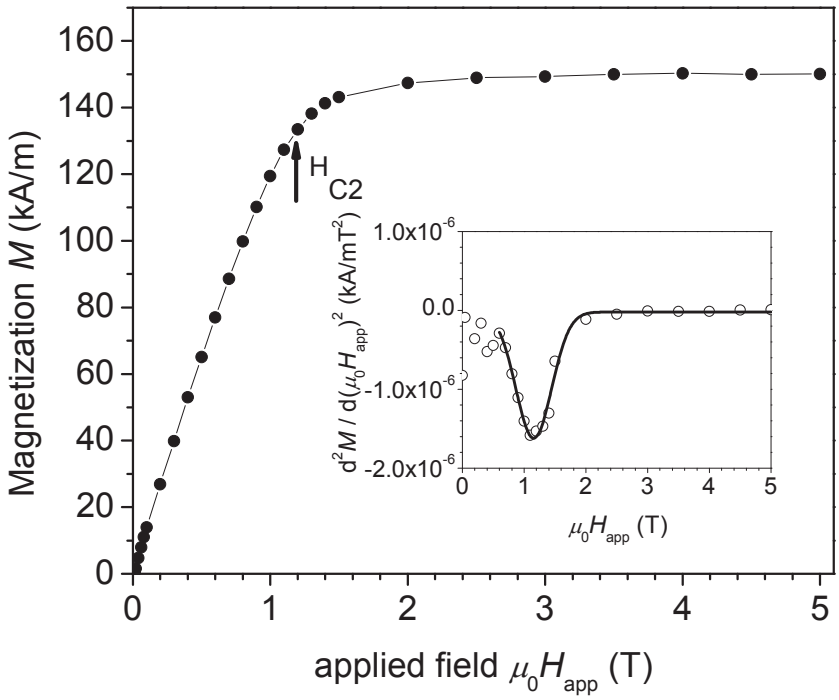

Figure 3.15. For an 11.5 nm sample grown by SPE, the out of plane measurement of the magnetization increases linearly up to a critical field of 1.16 ± 0.01 T. This value obtained from the minimum in $\mathrm{d}^2M / \mathrm{d}\left(\mu_0 H_{\mathrm{app}}\right)^2$ is shown in the inset.

approximately linearly with applied magnetic field up to a critical field H_{C2} = 1.16 ± 0.01 T, obtained from the minimum in $\mathrm{d}^2M / \mathrm{d}\left(\mu_0 H_{\mathrm{app}}\right)^2$ (Fig. 3.15). The in-plane hysteresis measurements (solid circles) for a field along $[1\,\bar{1}\,0]$ displayed $M - H$ features that were qualitatively similar but more rounded than the out-of-plane measurements, as shown in Fig. 3.14.

In Fig. 3.16, the saturation magnetization (M_{sat}) is shown as a function of film thickness, where the dashed line corresponds to the bulk moment of 0.39 μ_B / Mn [25]. Film thicknesses greater than 10 nm have an M_{sat} consistent with the bulk value. However, as the film thickness decreases below 10 nm, a decrease in the magnetization is observed before it rises to a value greater than that of bulk. This moment enhancement seen in the thinnest film may be due to the interfaces. Hortamani *et al*. used DFT calculations to predict a moment of 3.4 μ_B / Mn at the MnSi/Si interface [23]. As the film begins to increase in thickness, there is a drop in the moment per Mn atom, which may be due to the same defects that create changes in the elastic properties and T_C.

A simple model is proposed that attempts to describe the changes in the magnetic moment with thickness. Four layers were required to model the M_{sat} as a function of thickness: two MnSi/Si interfaces (assumed to have equal moments in order to simplify the model), a defected MnSi layer near the substrate and a bulk-like layer MnSi layer with a moment of (0.43 ± 0.03) μ_B / Mn. The solid line in Fig. 3.16 shows the result of the fit, where the defect layer thickness and the moments in each of the layers are treated as fitting parameters. The defected layer is (3 ± 1) nm thick with a moment of (0.22 ± 0.09) μ_B / Mn and the interfacial MnSi has an enhanced moment of (0.5 ± 0.1) μ_B / Mn, albeit not as large as predicted by DFT.

The thickness dependence of the remanent magnetization, obtained from $M - H$ curves, was used to search for evidence of helical magnetic order. The out-of-plane remanent magnetization was zero within experimental error, given a ± 5º uncertainty in the alignment of the sample in the SQUID magnetometer. This is consistent with a propagation vector pointing out of plane. However, the in-plane M_r is

not zero and it varies with thickness. In a helical magnet with an out-of-plane propagation vector, all the moments will cancel each other when the film thickness reaches an integer multiple of the wavelength of the helix. Therefore, M_r should oscillate as a function of thickness, d, according to the following equation, where f is a scaling factor:

$$\frac{M_r}{M_{sat}} = f \frac{\int_{-d/2}^{d/2} M_{sat} \cos(Qz)}{M_{sat}\, d} dz = f \frac{\sin(Qd/2)}{Qd/2}. \tag{3.2}$$

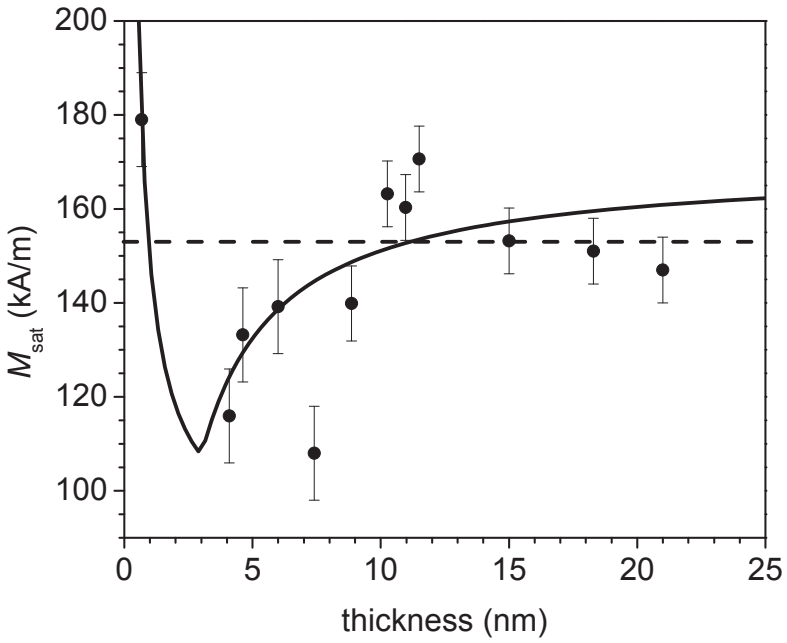

Figure 3.16. The saturation magnetization with ± 1σ error bars as a function of MnSi film thickness. The solid line is a fit to the data and the dashed line is M_{sat} for bulk MnSi.

In Fig. 3.17, the remanent magnetization M_r is shown normalized to the saturation magnetization M_{sat}. The solid line depicts the dependence expected using Eq. (3.2)

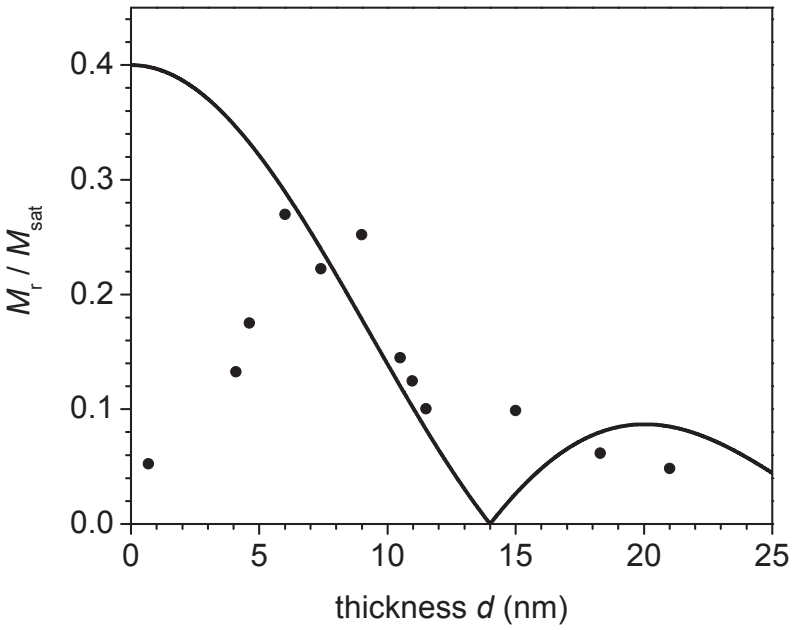

Figure 3.17. The remanent magnetization normalized to the saturation magnetization as a function of thickness. The solid line is fit obtained from Eq. (3.2) assuming a helical magnetic order with the propagation vector $\vec{Q}$ parallel the [111] direction with a wavelength of $2\pi/Q = 14$ nm.

assuming a helical magnetic order with a wavelength of $2\pi/Q = 14$ nm and the propagation vector $\vec{Q}$ oriented parallel to the [111] direction. The magnitude of the remanent magnetization is smaller than expected when integrating the moments of the helix over the film thickness. A scaling factor $f = 0.4$ was used to create a better fit to the

data. Unfortunately, Fig. 3.17 does not give any clear evidence for the magnetic order in the films. The normalized remanent magnetization determined from the data does not fall to zero for any thickness, contrary to the expectations for a helical magnet. The rounding observed in the $M - H$ curves suggests a distribution of helical wavelengths due to inhomogeneities in the films and these inhomogeneities together with variations in film thickness due to roughness could obscure the oscillations in the remanent magnetization as a function of thickness. This result motivated the growth of higher quality films by the method of MBE, as discussed in Chapter 4.

3.6 Glassy Behaviour

Unlike bulk MnSi, temperature dependant measurements performed on an 11.5-nm sample exhibited a surprising glassy behaviour. Glassy behaviour results from the effects of disorder and frustration and the presence of a broad distribution of energy barriers may explain this behaviour. Thermoremanent magnetization (TRM) measurements indicated that the magnetization for this sample relaxed over very long-time scales. In performing this measurement, the sample was cooled from 90 K to a target temperature in an applied field of 10 mT. The field was held at this temperature for $\tau_w = 500$ s before the field was set to zero. The remanent magnetization $M_r(\tau)$ was measured at the target temperature as a function of time, τ, as soon as the current in the magnet dropped to zero. The time dependence of $M_r(\tau)$ in TRM measurements for most temperatures can be described phenomenologically by,

$$M_r(\tau) = M_0 - S_M \log(\tau/\tau_0), \tag{3.3}$$

where M_0 is a constant and S_M is the magnetic viscosity and is arbitrarily set to τ_0 = 1s. However, experimental results differed from this equation when T neared 30 K, as seen in Fig. 3.18 (a). Therefore, the data was fit within an interval where $S_M = -dM_r(\tau) / d\log(\tau/\tau_0)$ is approximately constant, $10^3 < \tau < 10^4$ s, and the results plotted in Fig. 3.18 (b) showed a broad peak at 27 K. The logarithmic time dependence shown in Fig. 3.18 (a) and the broad peak in the viscosity indicate a magnetic relaxation over a broad distribution of energy barriers.

The TRM measurements also explain some of the unexpected behaviour of the remanent magnetization. Unlike the staggered magnetization in bulk MnSi, which follows a $M(0) - M(T) \sim T^{3/2}$ dependence, as explained by spin fluctuation theory [80], a linear dependence of the $M_r(T)$ curves was observed as shown in Fig. 3.11. In the absence of a spin wave theory for helical magnetic thin films needed for a detailed comparison with $M_r(T)$, a theory for ferromagnets provides some insight into the magnetic behaviour observed in MnSi thin films.

As with MnSi, the magnetization calculated from mean field theory for ferromagnets also follows a $T^{3/2}$ law. In ferromagnetic thin films, the temperature dependence of the magnetization follows,

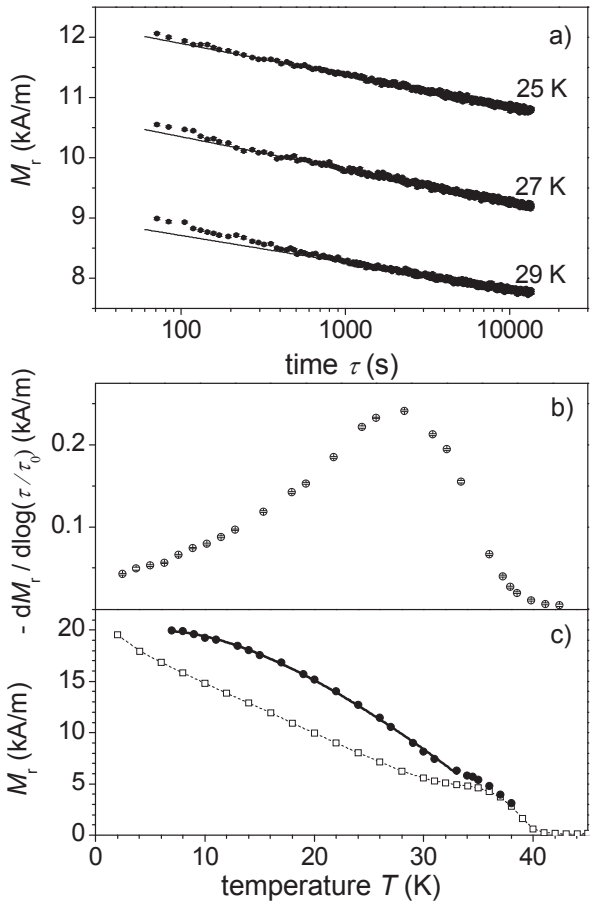

Figure 3.18. a) TRM in a 11.5-nm thick MnSi film as a function of time, τ, measured after cooling in a field of 10 mT, and waiting for $\tau_w = 500$ s at the target temperature before turning off field. b) Magnetic viscosity determined from the slope of the TRM data at 3600s. c) TRM measured approximately $\tau = 70$ s after turning off the field. The curve is a fit using spin-wave theory for ferromagnetic thin films, Eq. (3.4). For comparison, a portion of the M_r (T) data (open symbols) from Fig. 3.11 is included.

$$[M_r(0) - M_r(T)] \sim k_B T \ln\left(E_g / k_B T\right), \tag{3.4}$$

where E_g is the effective spin-wave gap due to anisotropy and dipolar interactions [81]. Given the same $T^{3/2}$ temperature dependence for ferromagnets and helical magnets, Eq. (3.4) was assumed to hold true for magnetic thin films as well. For MnSi thin films, an explanation for the deviation of the $M_r(T)$ data from the shape of the fit given by Eq. (3.4) is revealed by TRM measurements performed immediately after the field is turned off and before the magnetization has a chance to relax significantly. A TRM measurement at approximately t = 70 s as a function of temperature is shown in Fig. 3.18 (c). A good fit to the data is shown by the solid line using Eq. (3.4) with E_g = 1.4 meV. The difference between the TRM and $M_r(T)$ curves can therefore be understood by the slow decay of the magnetization.

Given that the films were assumed to consist of a single crystal, it was not clear where the frustration came from. However, plan-view TEM images provided an explanation for the glassy behaviour observed in the SPE grown films. Due to the non-centrosymmetric crystal structure of MnSi, there is a handedness in the crystal structure. TEM images presented evidence that both left and right-handed domains are present in the MnSi films in nearly equal proportions. Micron-sized chiral domains were observed by tilting the samples by ~16° so that the electron beam was aligned along the [221] and [112] zone axes of MnSi and Si, respectively. This produced the SADP shown in Fig. 3.19 (a). The dark-field image shown in Fig. 3.19 (c) was produced from the $(\bar{1}02)$ reflection, displayed in Fig. 3.19 (a). In this image, half of the image has a bright intensity and Fig 3.19 (a) shows a SADP obtained from one of the bright domains. A SADP obtained from a dark domain resulted in the SADP image shown in Fig. 3.19 (b).

The dark-field image of the $(0\,\bar{1}\,2)$ reflection is shown in Fig. 3.19 (d) and the image contrast of the domains with respect to Fig. 3.19 (c) is reversed. Therefore, two distinct crystalline domains were observed in the MnSi layer that occurred with nearly equal probability. The two regions have opposite chiralities and this is important since the chirality of the magnetic structure is determined by the handedness of the crystal structure. In bulk MnSi, Ishida *et al*. reported that left-handed inversion domains have a left-handed spiral [82]. The interface between the domains would therefore produce magnetic frustration due to competing windings of the magnetic moments in the adjacent helical magnetic domains. The glassy magnetic behaviour can therefore be explained by a combination of disorder and frustration in the films where the disorder arises from the distribution of inversion domains and defects, and the frustration arises from the inversion domain boundaries.

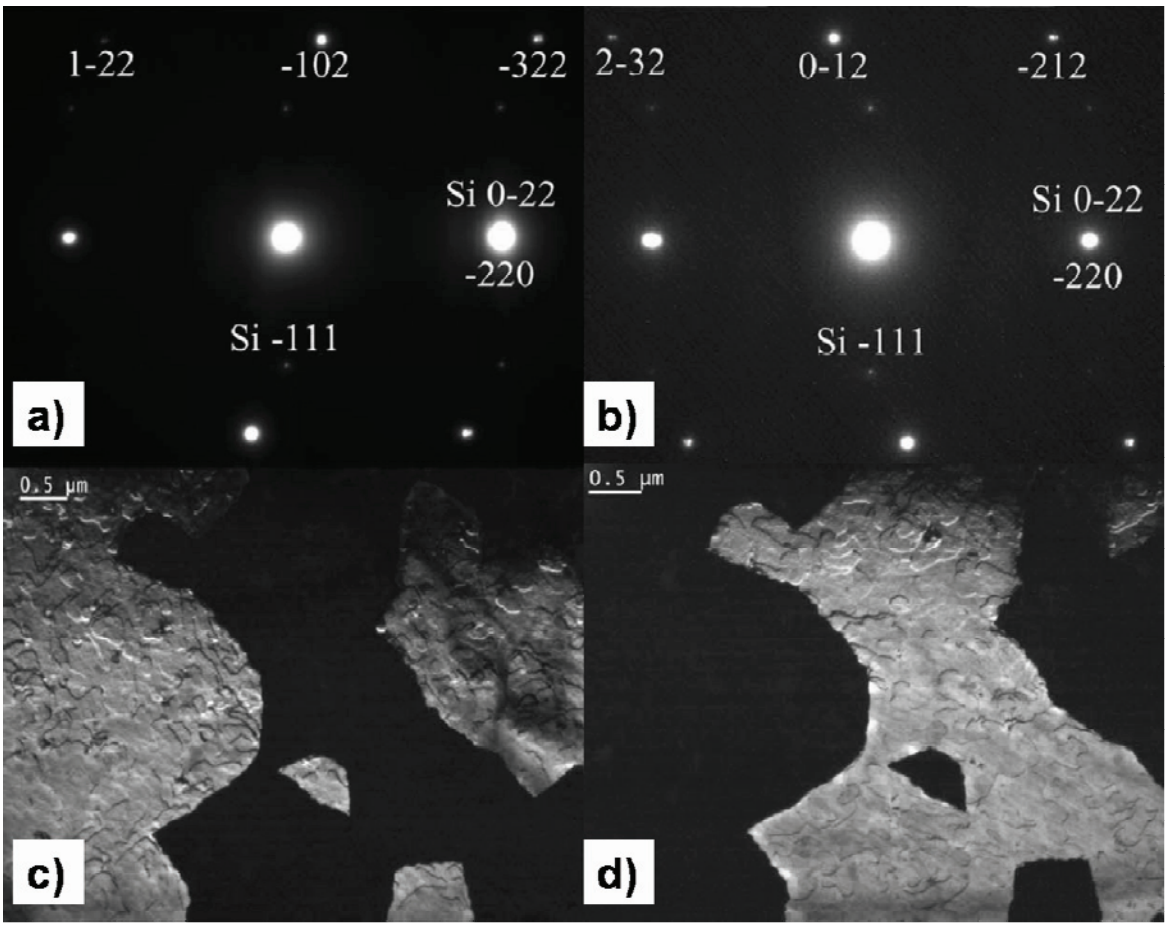

Figure 3.19. TEM images of a 6-nm-thick MnSi layer on a Si substrate. a) SADP from one of the MnSi chiral domains. b) SADP from the opposite MnSi chiral domain. c) Dark-field TEM image using the $(\bar{1}02)$ spot from a). d) Dark-field TEM image using the $(0\,\bar{1}2)$ spot from b). (Images courtesy of Prof. M.D. Robertson, Acadia University)

Chapter 4 – Characterization of MBE Grown MnSi Films

The lack of evidence of helical magnetic order in the SPE grown thin films motivated a search to find another growth method that would produce smoother MnSi films. In this chapter, a report is presented on the magnetic structure of MnSi(111) thin films grown by MBE. A combination of PNR and SQUID magnetometry show that the films have helical magnetic order with a propagation vector $\vec{Q}$ along the film normal. A helix wavelength of $2\pi/Q$ = 13.9 ± 0.1 nm is found to be independent of film thickness over a 7 – 40 nm range in film thickness. PNR shows that the magnetic structure has both left-handed and right-handed chiralities due to the presence of inversion domains observed by TEM.

This chapter also presents a magnetic characterization of MnSi thin films in a magnetic field transverse to $\vec{Q}$ in order to understand the reorientation of the helical magnetic order. The magnetic behaviour in an in-plane $[1\,\bar{1}\,0]$ field direction shows a clear departure from the behaviour reported in bulk. In order to understand this difference, the uniaxial magnetocrystalline anisotropy (MCA) in the films as a function of thickness was measured by SQUID magnetometry. A combination of PNR and SQUID magnetometry show that helical magnetic order is distorted in the direction of the applied field.

4.1 Chemical Structure of MBE Grown Films

The MnSi(111) thin films grown by MBE onto Si(111) substrates were prepared as described earlier in Section 2.1. XRD, XRR and PNR measurements showed that this

method of growth improved the quality of the films compared to the SPE grown films. As shown in Fig. 3.6 and discussed in Chapter 3, the interfacial roughness in the SPE grown films washed out the Kiessig fringes in the XRD measurements about the MnSi(111) peak for films thicker than 11.5 nm. For the MBE grown films shown in Fig. 4.1, the Kiessig fringes were larger in amplitude than the SPE films and begin to disappear near a thickness of 39.5-nm. This is consistent with smoother film interfaces.

The large increase in the oscillation amplitude of the XRR data in Fig. 4.2 shows significant improvement in the interface quality of MBE films as compared to the SPE grown films shown in Fig. 3.5. In Fig. 4.2, large oscillations are observed up to q_z = 4.3 nm^{-1} for both the 14.6-nm and 26.7-nm samples. However, the oscillations attenuate more quickly in the 39.5-nm sample due to larger interfacial roughness and the presence of precipitates in this sample. The fits to the XRR data (Fig. 4.2 (a) generated from the SLD plots, as shown in Fig. 4.2 (b) – (d), are in agreement with the thicknesses and roughnesses extracted from XRD. The SLD plots show sharp interfaces indicating smoother interfaces for the 14.6-nm and 26.7-nm thick films compared to the rounded interfaces observed for the 39.5-nm thick film. Since MnSi occupies a narrow region in the MnSi phase diagram, shown earlier in Fig. 3.1, it is sensitive to the ratio of Mn to Si. Instabilities in the flux during growth created $MnSi_{1.7}$ precipitates in many of the samples.

Fig. 4.3 shows three TEM bright field plan-view images that represent different amounts of $MnSi_{1.7}$ precipitates found in the films. For film thicknesses less than 11.6 nm, no evidence of precipitate formation was observed. For the remaining films, $MnSi_{1.7}$ precipitates with varying diameters as large as 0.5 μm were found (Fig. 4.3 (b)

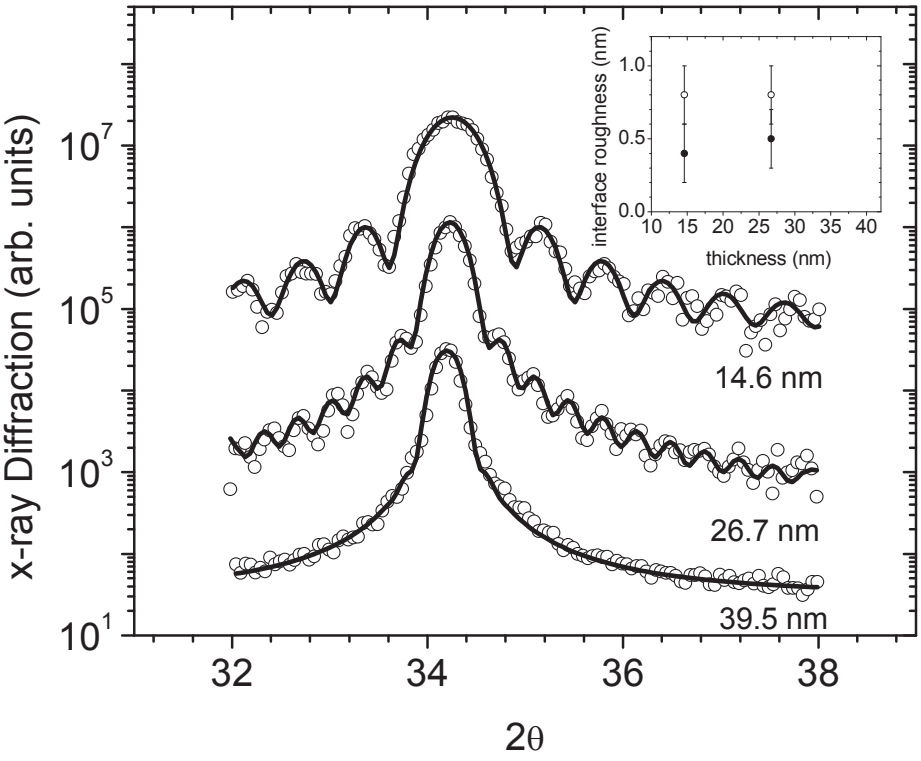

Figure 4.1. XRD measurements of a MnSi (111) peak for 14.6-nm, 26.7-nm and 39.5-nm thick films are shown. The solid line is a fit to the MnSi (111) peak. The inset shows the interface roughness of the lower film boundary (solid circles) and the upper boundary (open circles). The moderate interface roughness in the MBE samples makes it difficult to resolve the Kiessig oscillations at higher film thickness.

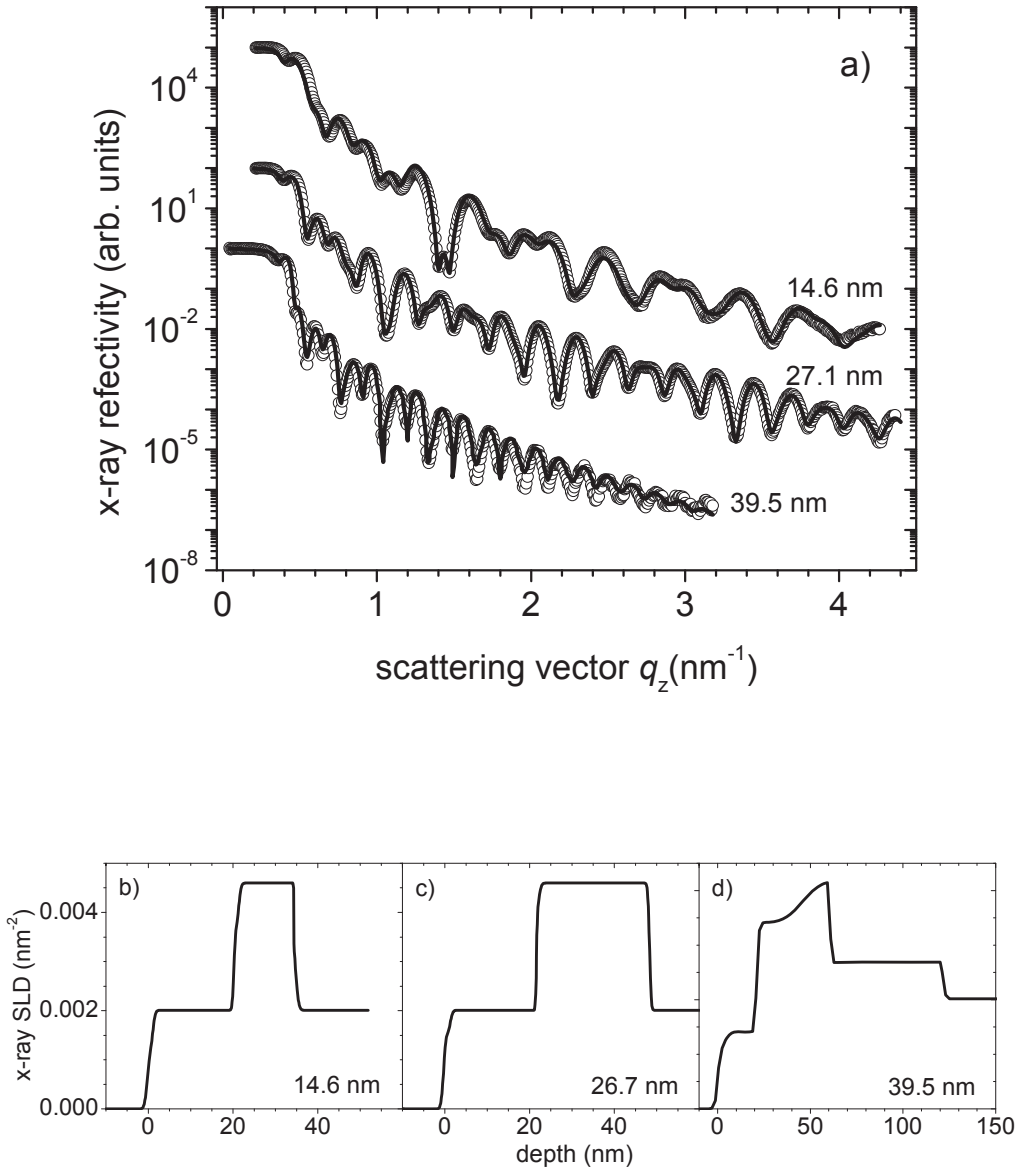

Figure 4.2. (a) XRR measurements (open circles) of 14.6-nm, 26.7-nm and 39.5-nm thick MnSi films grown by MBE presented. The fits generated from the x-ray SLD, shown in the lower 3 panels, (b – d), are represented by the solid lines in (a).The XRR curves are separated by a vertical offset for clarity.

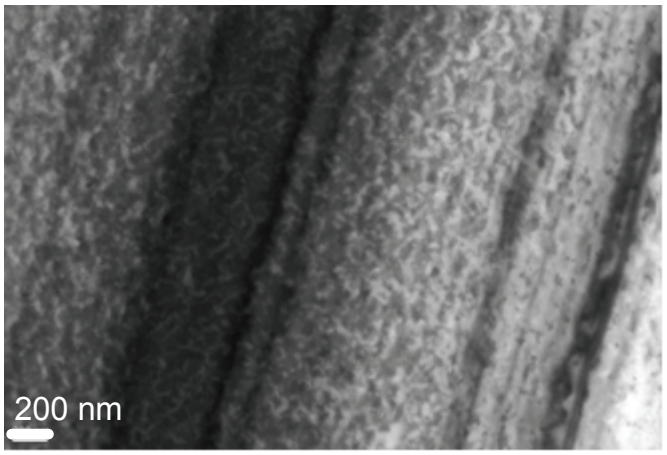

a) 11.6-nm film with no evidence of $MnSi_{1.7}$ precipitates.

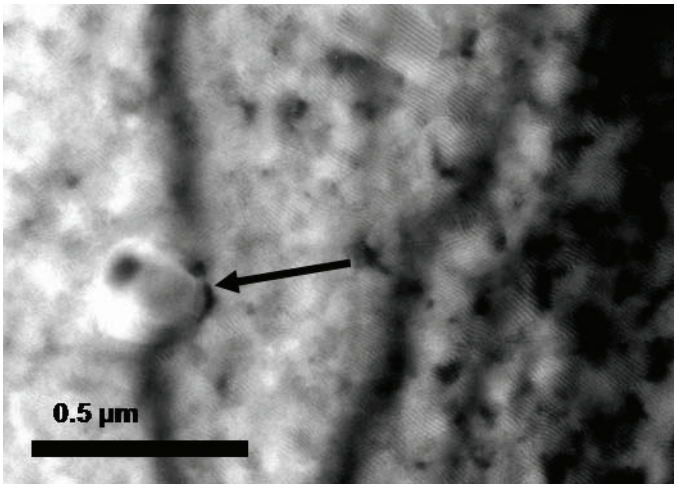

b) 14.6-nm film with ~7% $MnSi_{1.7}$ coverage. The $MnSi_{1.7}$ precipitates, an example of which is show by the arrow, are ~ 200 µm in diameter.

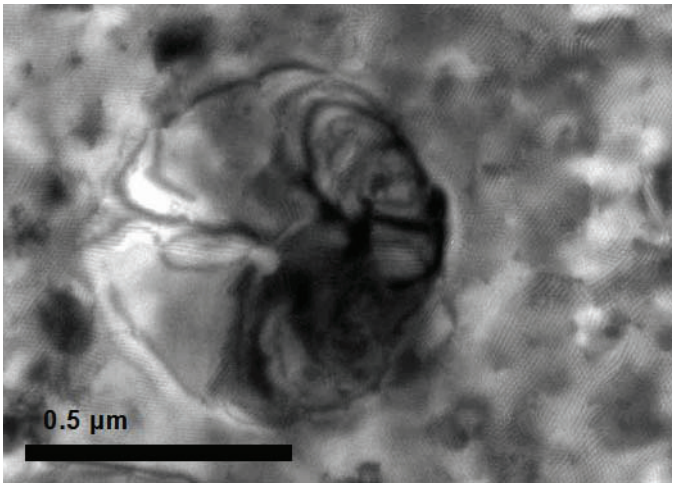

c) 35.6-nm film with ~ 19% of film covered by $MnSi_{1.7}$ precipitates. Precipitates have increased in size to ~0.5 um.

Figure 4.3. TEM bright-field plan-view images of MnSi thin films. (Images courtesy of Prof. M. D. Robertson, Acadia University)

and (c)). Two of the thin film samples (not shown) were observed to contain more than 60 % precipitate coverage. In these two samples, the saturation magnetization (M_{sat}) dropped significantly, as shown in Fig. 4.4, due to the low magnetic moment of 0.012 μ_B / Mn, for $MnSi_{1.7}$ precipitates [83]. The concentration of $MnSi_{1.7}$ in the films

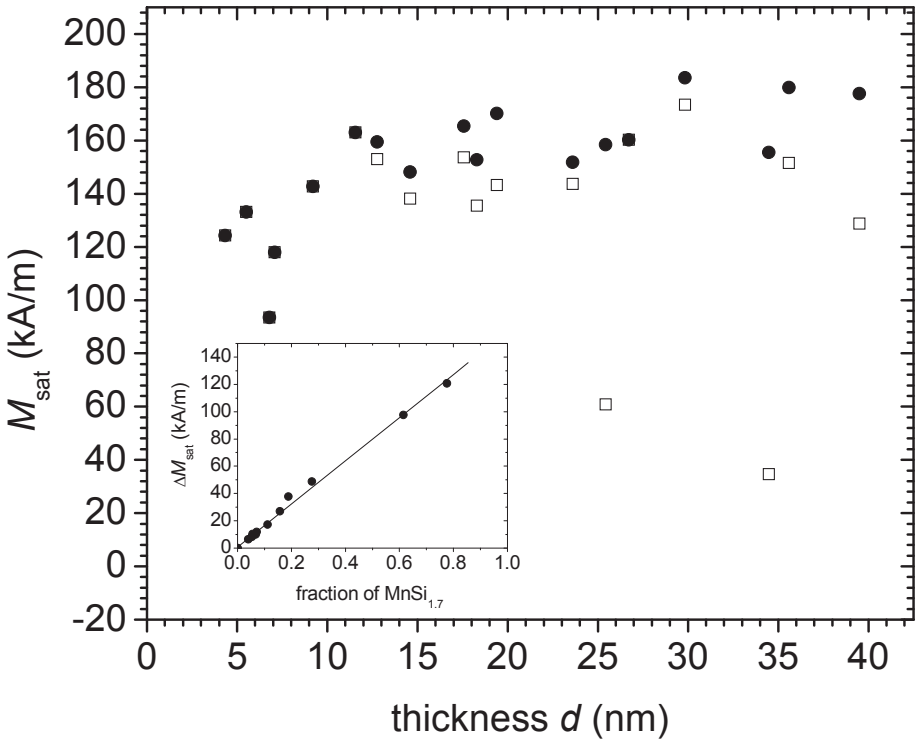

Figure 4.4. M_{sat} as a function of thickness for MnSi films grown by MBE. The open squares represent the M_{sat} data before correcting for $MnSi_{1.7}$. The solid circles are the corrected values for M_{sat} taking into account the fraction of the film occupied by the $MnSi_{1.7}$ phase. The difference between these two values, ΔM_{sat}, as a function of the percentage of $MnSi_{1.7}$ precipitates is shown in the inset.

is consistent with the drop in M_{sat} observed in the samples, as shown in the inset in Fig. 4.4. This means that the measured moment is only due to MnSi, and the fluctuations in the total volume are due to error in the measure of the volume of MnSi based only on sample area and sample thickness. Corrections to the volume of the MnSi phase were determined from the fraction of the sample occupied by the $MnSi_{1.7}$ phase in the plan-view TEM images, and were used to correct the values of M_{sat}. Above a thickness of 9 nm, the M_{sat} is approximately constant with an average value M_{sat} = 163 ± 3 kA/m. This corresponds to a moment of μ_{film} = 0.42 ± 0.01 μ_B / Mn as compared to μ_{bulk} = 0.39 μ_B / Mn in bulk crystals [25].

TEM dark field images of the MBE grown films provided evidence of a handedness in the crystal structure. TEM images presented in Fig. 4.5 were imaged under

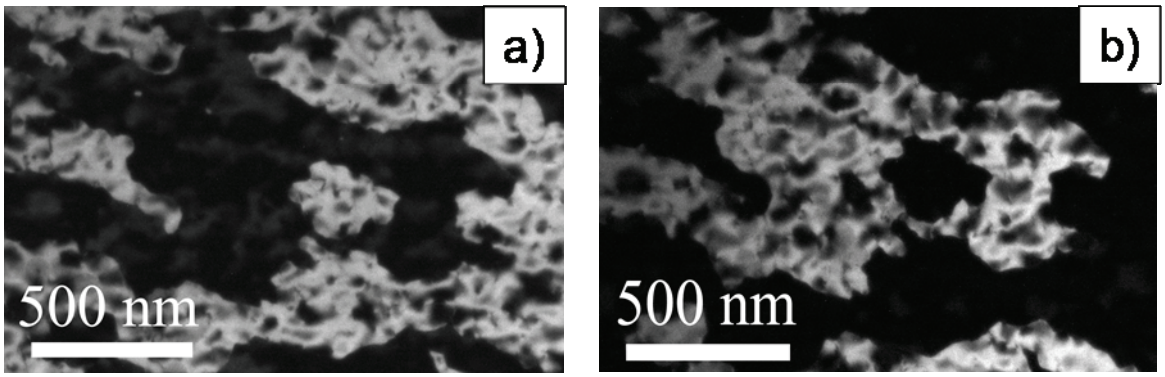

Figure 4.5. Dark field images of a d = 17.6-nm thick film grown by MBE. Chiral domains were imaged by tilting away from [111] direction to the [221] zone axis of MnSi. Complementary (0-12) and (-102) reflections from SADP spots described in Section 3.6 were used in (a) and (b), respectively, which have opposite contrast for opposite crystal chiralities. (Images courtesy of Prof. M. D. Robertson, Acadia University)

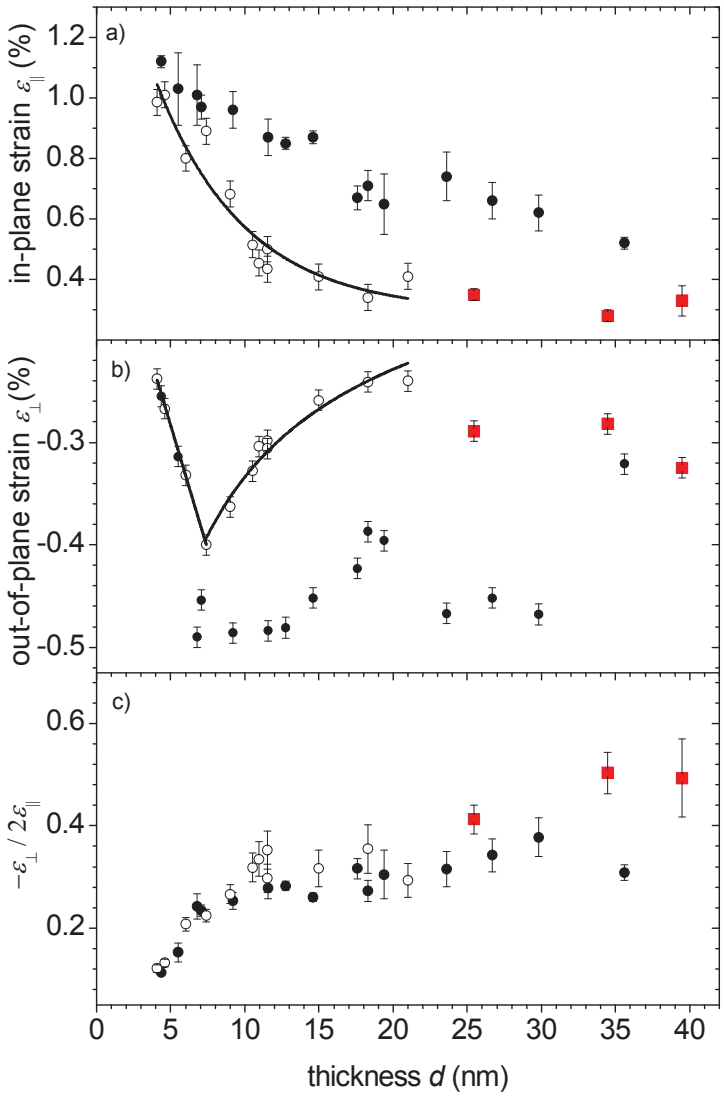

Figure 4.6. (a) In-plane strain measured by TEM plan-view SADP, (b) out-of-plane strain measured by XRD, and (c) the ratio of the out-of-plane strain to twice the in-plane strain as a function of thickness. SPE films are shown by open symbols, and MBE sample by closed symbols. Samples with a concentration of $MnSi_{1.7}$ precipitate greater than 20% are shown by square symbols. All error bars are ± 1 σ.

the same tilt orientation as described for the SPE grown films in Chapter 3. Since both left- and right-handed domains are present in the MBE grown films, both magnetic chiralities are also present [82]. The chiral domains are a few hundred nm in width, as compared to the micron-sized domains observed in the SPE grown thin films.

The in-plane and out-of-plane strain in the MBE grown MnSi films with respect to film thickness are shown in Fig. 4.6 (a) and 4.6 (b) respectively. In Fig. 4.6 (a) and (b), the strains are higher in the MBE samples (solid symbols) compared to the SPE samples (open symbols). The higher residual strains are attributed to the shorter annealing times during MBE growth. However, the ratio of the strains $-\varepsilon_{\perp} / 2\varepsilon_{\parallel}$ for the MBE grown films, which is related to the ratio κ / c_{44}, is the same for the MBE and SPE grown films, as shown in Fig. 4.6 (c), if samples with a $MnSi_{1.7}$ precipitate concentration greater than 20% are ignored. For films within a thickness range of 9.2 nm – 39.5 nm, the strain ratio $-\varepsilon_{\perp} / 2\varepsilon_{\parallel}$ shown in Fig. 4.6 (c) had an average value of 0.31 ± 0.01 when samples with percentages of $MnSi_{1.7}$ greater than 20% are neglected. This agrees with the value of 0.32 ± 0.01 shown earlier for samples grown by SPE, which suggests that the elastic constants for both sets of samples are the same. As with the SPE grown films discussed in Chapter 3, interstitial defects may be responsible for the observed behaviour.

In contrast, a large concentration of $MnSi_{1.7}$ precipitates does affect the elastic properties of MBE grown films, as shown in Fig. 4.6 (c). For the three cases with a concentration greater than 20%, both $\varepsilon_{\perp}$ and $\varepsilon_{\parallel}$ are more relaxed than the strains found in the other MBE samples, which suggests that the precipitates help to nucleate dislocations. Furthermore, the large values of $-\varepsilon_{\perp} / 2\varepsilon_{\parallel}$ suggest that large concentrations of $MnSi_{1.7}$

precipitates soften c_{44}. Further measurements are needed in order to understand the complex strain behaviour observed in the MBE grown films.

4.2 Magnetic Structure of the MBE Grown Films

Strain has an effect on the magnetic structure of the epitaxial films grown on the Si (111) substrates, as discussed in Chapter 3. Since the films grown by MBE are smoother than films grown by SPE, the effects of an applied field on the magnetic structure of MBE grown films were explored. SQUID magnetometry measurements were performed on a series of MBE grown thin films with thicknesses ranging from 4.3 – 39.5 nm with the same sample orientations as discussed in Chapter 3.

The Curie temperature was determined using the two different methods previously described in Chapter 3. The average Curie temperature between a thickness of 9.2 – 39.5 nm, T_C = 42.3 ± 0.2 K, is larger than the average $T_C = 40.6 \pm 0.4$ K for SPE samples. Fig. 4.7 presents a plot of the T_C as a function of volume strain. For a given film thickness, the MBE data have a higher volume strain than the SPE data, and as expected, have a higher T_C. A correlation was observed between T_C and the strain ratio (Fig. 4.8) similar to that seen in the SPE samples. The T_C of the samples with a percentage greater than 20% of $MnSi_{1.7}$ precipitates followed the same thickness dependence as the other films, which suggests that the precipitates do not affect the T_C. For MBE grown films with a thickness less than 9.2 nm, a similar drop was observed in the Curie temperature and the elastic constant, as seen with the SPE grown films. However, the MBE samples

do show a higher peak in the T_C vs. $\Delta V / V$ curve. This drop in T_C with thickness could be due to the presence of defects as with the case for SPE samples.

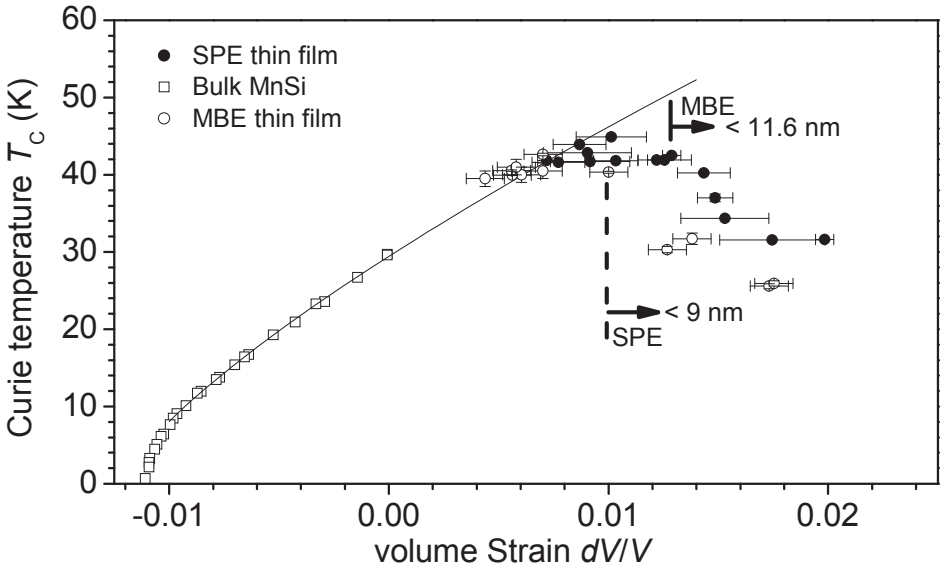

Figure 4.7. Comparison between the dependence of Curie temperature on volume strain in MnSi SPE (open circles), MBE (closed circles) thin films, and the data for bulk MnSi (open squares) from Ref. [78]. The curve is an extrapolation of a fit to the bulk data using spin fluctuation theory [78]. The vertical dashed and solid lines show where T_C begins to drop with film thickness for SPE and MBE grown films, respectively.

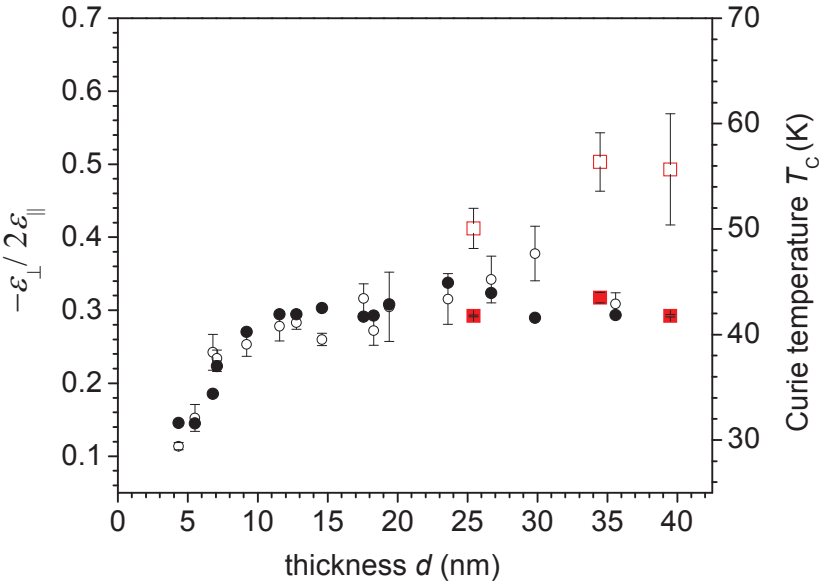

Figure 4.8. Correlation between T_C and the ratio of the out-of-plane to twice the in-plane strain. The T_C vs. thickness is shown by the solid symbols and the ratio of the out-of-plane to twice the in-plane strain is shown by the open symbols. Thin films with concentrations of $MnSi_{1.7}$ precipitates greater than 20% are shown by square symbols.

SQUID measurements provided indirect evidence of helical magnetic order in the MBE grown films. In Fig. 4.9, the remanent magnetization was measured by saturating the films in a 5-T field along the $[1\,\bar{1}\,0]$ in-plane direction (solid circles) at a temperature of 5 K. The field was then reduced to zero. No remanent magnetization was found in the out-of-plane [111] direction, which is consistent with the expectation that the moments lie in the plane of the film, as was found for the SPE samples.

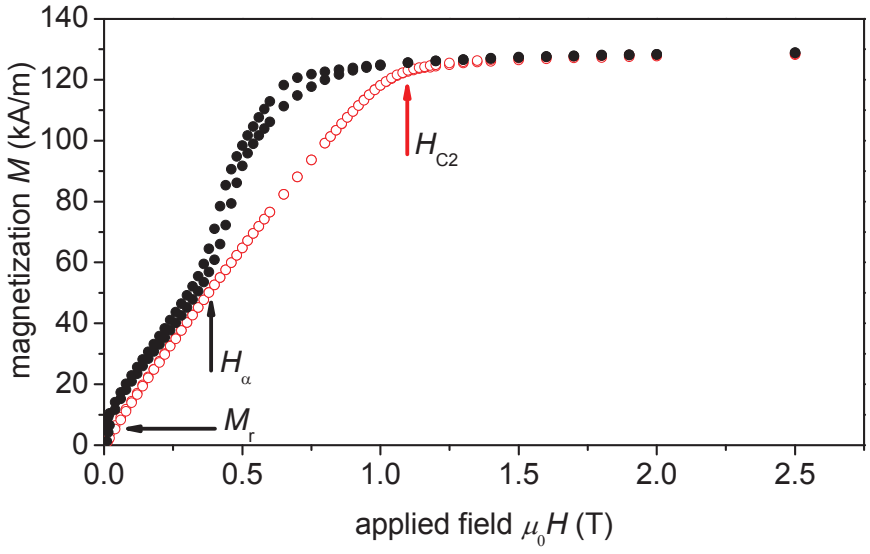

Figure 4.9. Magnetization as a function of applied field for a 20-nm Si / 39.5-nm MnSi / Si(111) film. The open circles are a measure of magnetization in the [111] out-of-plane direction. The solid circles are a measure of the magnetization in the $[1\,\bar{1}\,0]$ in-plane direction. H_{C2} is the out-of-plane saturation field. The remanent magnetization M_r is film-thickness dependent in-plane and zero out of plane.

Fig. 4.10 shows that M_r/M_{sat} oscillates as a function of thickness, as would be expected for a helix oriented out-of-plane. The fit generated from Eq. (3.2) agrees with the data for thicknesses greater than 7 nm. The presence of magnetic domains accounts for the scaling factor $f = 0.51 \pm 0.02$. The propagation vector $\vec{Q} = 0.451 \pm 0.004$ nm^{-1} corresponds to a wavelength of $2\pi/Q = 13.9 \pm 0.1$ nm, as compared to the bulk value of 18 nm [29, 31]. The agreement between the model and the data between 7 nm and 40 nm suggests that Q is constant over this range. The departure of the data from the model for

thicknesses less than 7 nm may be explained by the presence of domains, the presence of a helix with a shorter wavelength, the absence of helical magnetic order or the effect of surface anisotropies. Further investigations, which include the measure of surface anisotropy and, ideally, magnetic imaging are required to resolve this issue.

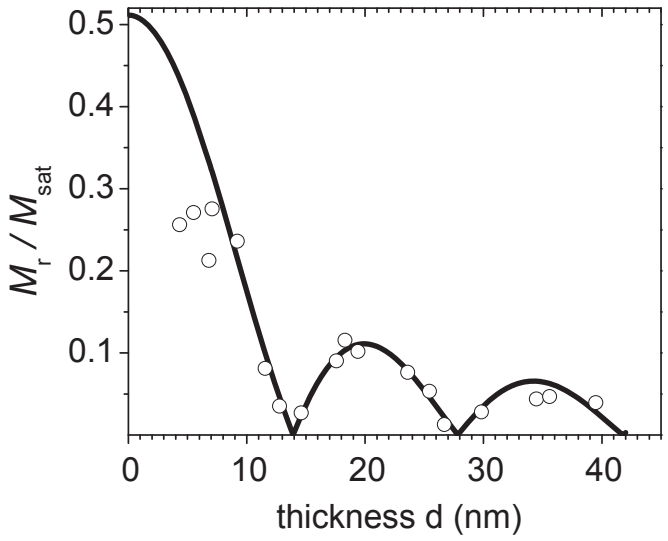

Figure 4.10. The remanent magnetization normalized to the saturation magnetization as a function of film thickness. The solid line shows the fit to the data using Eq. (3.2), which gives $2\pi/Q = 13.9 \pm 0.1$ nm.

4.3 Direct Evidence of Helical Magnetic Order

PNR measurements found direct evidence of helical magnetic order and were performed at the NIST Center for Neutron Research on a 20-nm Si / 39.5-nm MnSi / Si(111) MBE grown sample using the NG-1 reflectometer. Four spin dependent reflectivities R(+ +), R(– –), R(– +) and R(+ –) were measured, where the R(+ +), R(– –)

are the non-spin-flip reflectivities and the R(– +) and R(+ –) are the spin flip reflectivities. In order to minimize the disorder due to domains, the sample was field-cooled from RT to 7 K in an applied field of $\mu_0 H_{app}$ = 0.8 T, oriented in the [1 $\bar{1}$ 0] in-plane direction before reorienting the field to the out-of-plane direction. Initially, no evidence of helical magnetic order was observed in the spin-flip channels in this configuration. To maximize the spin-flip signal that contains the information about the chirality, a non-conventional geometry (schematic shown in Fig. 4.11) was used, where the magnetic field and the neutron spins are nearly parallel with the film normal [84]. The sample was field cooled along the *x*-axis and then the field was rotated to a position

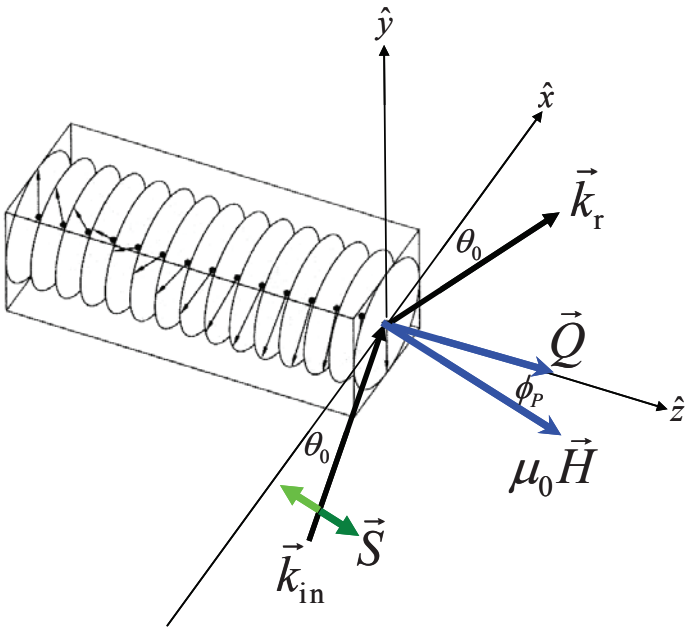

Figure 4.11. Schematic diagram showing experimental geometry of a PNR measurement of a 20-nm Si / 39.5-nm MnSi / Si(111) film. A small in-plane magnetic field created by rotating the magnetic field ϕ_P = 7.5º away from the film normal was needed to observe R(+ –) and R(– +).

ϕ_P = 7.5° away from the film normal. This provided a small in-plane field to align the domains in the sample and reduce the magnetic disorder in the films due to the glassy magnetic behaviour described in Section 3.6 [70]. In the schematic shown in Fig. 4.11, the MnSi $[1\,\bar{1}\,0]$ film direction is shown oriented along the *y*-axis with the film normal pointing along the *z*-axis. For an applied field of $\mu_0 H_{app}$ = 0.2 T, the in-plane component of the field was $\mu_0 H_{app}$ = 26 mT, which is larger than the $\mu_0 H_{app}$ = 8.3 mT coercive field of the 39.5-nm film. At T = 7 K and $\mu_0 H_{app}$ = 0.2 T, a broad magnetic Bragg peak was observed in both the spin-flip signals at q_z = 0.45 nm^{-1} with equal intensity, as shown in Fig. 4.12. In order to check that this peak had a magnetic origin, the field strength was

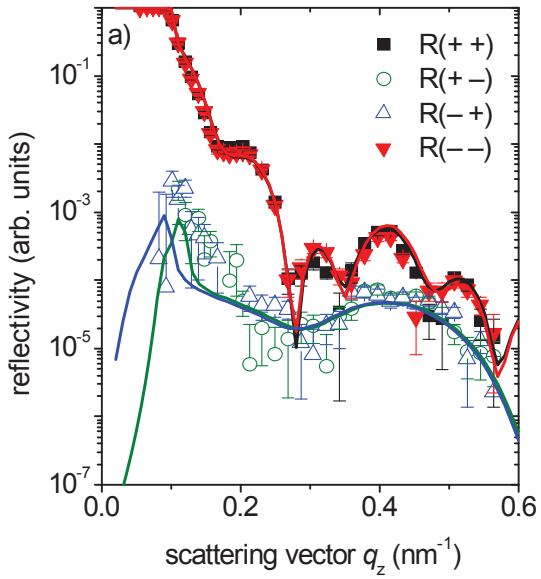

Figure 4.12. PNR measurement of a 20-nm Si / 39.5 nm MnSi / Si(111) film with the experimental geometry shown in Fig. 4.11. The sample was field cooled to T = 7 K in a field of $\mu_0 H_{app}$ = 0.2 T. Solid lines show all four fits to the data.

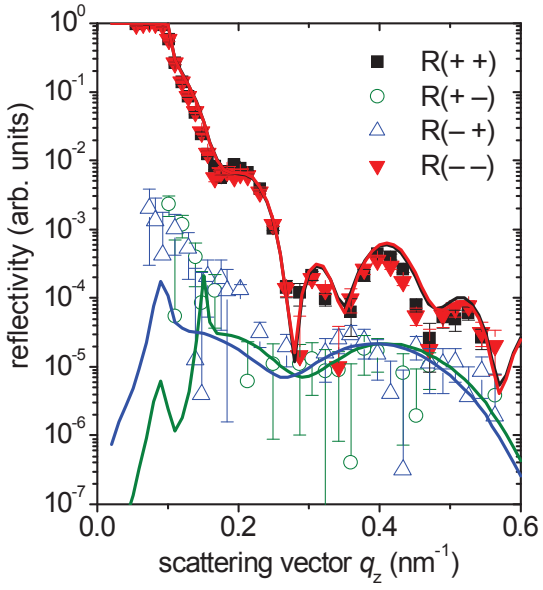

Figure 4.13. PNR measurement of a 20-nm Si / 39.5-nm MnSi / Si(111) film with the experimental geometry shown in Fig. 4.11. Measurement of the sample was performed at a temperature of 7 K and in a field $\mu_0 H_{app}$ = 0.6 T. Solid lines show all four fits to the data.

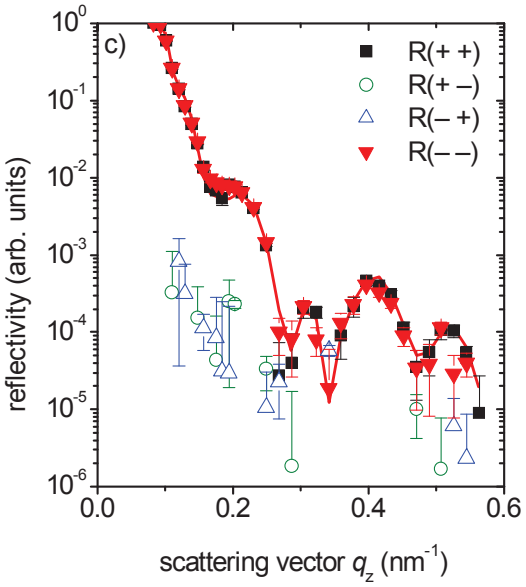

Figure 4.14. PNR measurement of a 20-nm Si / 39.5-nm MnSi / Si(111) film with the experimental geometry shown in Fig. 4.11. Measurement of the sample was performed at a temperature of 80 K and in a field $\mu_0 H_{app}$ = 0.6 T. Solid lines show fits to the non-spin flip data.

increased to $\mu_0 H_{app}$ = 0.6 T (Fig. 4.13). The resulting drop in intensity observed in both R(+ –) and R(– +) is explained by the reduction of the in-plane component of the magnetization. The cone angle $\alpha = \sin^{-1}(H / H_{C2}) = 36°$ was found for $\mu_0 H_{app}$ = 0.6 T, as compared to α = 11° for a field of 0.2 T. Fig. 4.14 shows that the spin-flip signal disappeared when the temperature of the film was subsequently raised to 80 K, well above T_C, which confirms the magnetic origin of this peak.

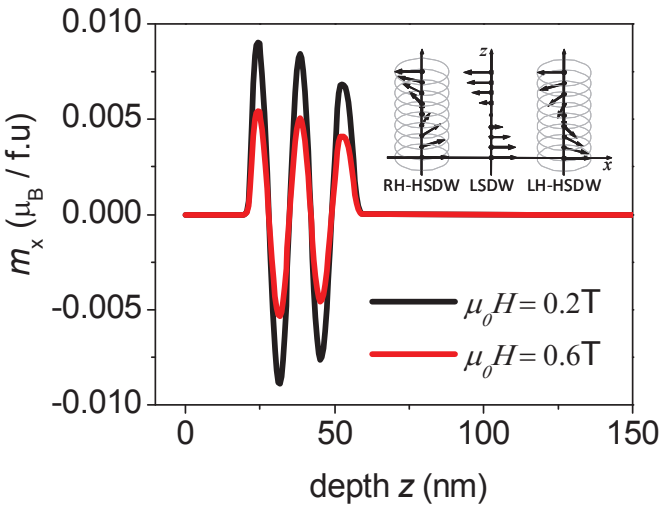

Figure 4.15. Depth distribution of the component of the magnetic moments along the direction of the applied field (in units of μ_B per formula unit) used to fit data in Fig. 4.12 – Fig. 4.14. The magnetization profile is consistent with a linear spin-density wave (LSDW) created by a superposition of a left-handed and right-handed spin-density wave, shown in the inset.

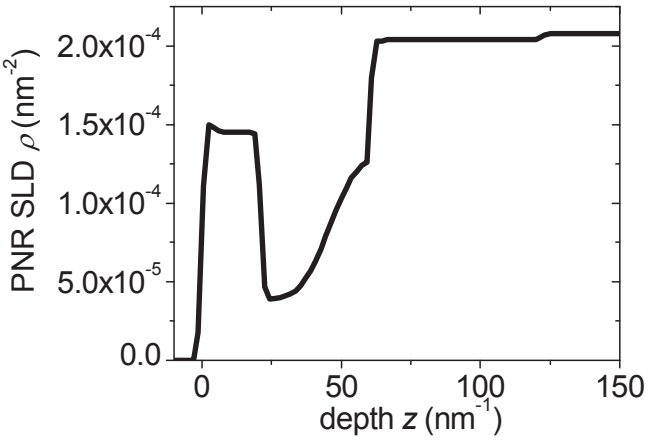

Figure 4.16. Depth distribution of nuclear SLD used to fit data in Fig. 4.12 – Fig. 4.14.

To determine the chemical structure of the thin film, the non-spin-flip PNR data (measured at a temperature of 80 K) and the XRR were simultaneously fit to the same model. The SLDs for Si, MnSi and SiO_2 are shown in Table 4.1. The PNR data was background and footprint corrected using Reflpak software [85]. The model used to calculate the reflectivity was based on the cross-sectional TEM image shown in Fig. 4.17. Both the XRR and PNR average the scattering length density in the plane of the sample over the coherence length, which is much larger than the $MnSi_{1.7}$ precipitates; therefore, a layered model is an appropriate description of the data. Table 4.2 shows the model of the Mn containing layers used to fit the PNR and XRR data with four fitting parameters: atomic or molecular number density ρ_m, the atomic fraction of Mn atoms, the layer thickness and the layer roughness σ_R. The SLD profiles obtained from the x-ray (Fig. 4.18 inset) and neutron data (Fig. 4.16) were generated from the same set of parameters shown in Table 4.2 and produce reflectivities that are in good agreement with both sets of the data in Fig. 4.14 and 4.18. The magnetic structure of the film was

obtained from the spin-flip signal. As explained in Chapter 2, a monochiral system would not produce a Bragg-like peak in both spin-flip channels. The fact that peaks of equal intensity were observed in R(– +) and R(+ –) implies that both left and right handed chiralities exist in equal proportions in the films. This is consistent with the TEM measurements in Fig. 4.5, since both crystal chiralities are observed in these films, and therefore both magnetic chiralities would be expected [82]. Since the coherence length of the neutron is approximately 10 μm, the neutron reflectivity is an average of many chiral domains. Averaging both left and right-handed helical spin density waves produces a linear spin density wave polarized along the in-plane component of the magnetic field. The depth profile of the magnetic moment (Fig. 4.15) was determined from fits to the spin flip reflectivities using only two fitting parameters: Q and the

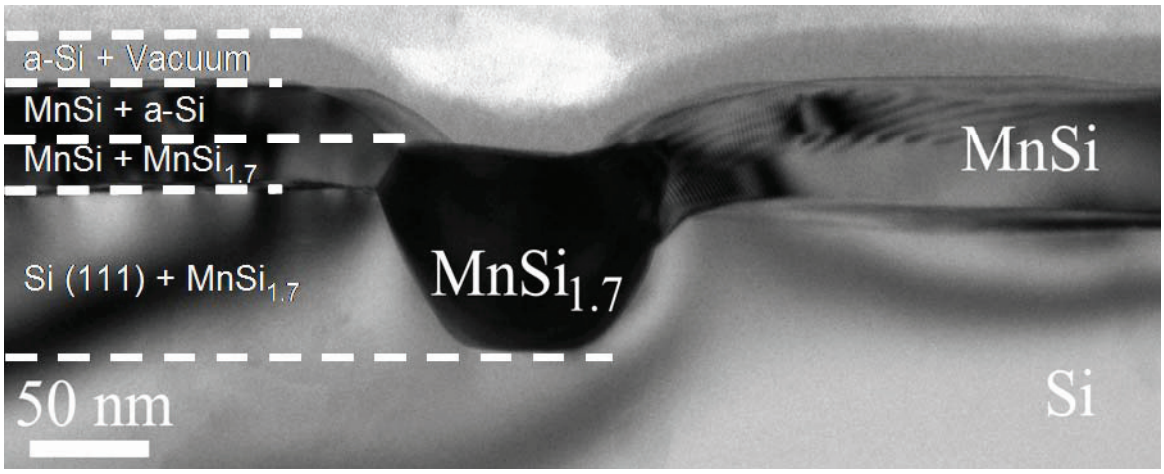

Figure 4.17. Cross-sectional TEM image of a 20 nm Si/39.5nm MnSi/ Si (111) film showing one of the $MnSi_{1.7}$ precipitates. (Image courtesy of Prof. M. D. Robertson, Acadia University)

	ρ_m ($\times 10^{28}$ m^{-3})	b (fm)	X-ray SLD(Re) (nm^{-2})	X-ray SLD(Im) (nm^{-2})	SLD neutrons (nm^{-2})
Si	5.00	4.15	2.01×10^{-03}	4.58×10^{-05}	2.08×10^{-04}
Mn	8.18	-3.73	5.66×10^{-03}	6.54×10^{-04}	-3.06×10^{-04}
MnSi	8.44	0.21	4.59×10^{-03}	3.74×10^{-04}	1.76×10^{-05}
SiO2	2.51	15.8	2.15×10^{-03}	2.76×10^{-05}	3.97×10^{-04}

Table 4.1. A summary of the atomic or molecular number density, neutron scattering length, x-ray scattering length densities and neutron scattering length densities for Si, Mn, MnSi and SiO_2. (Re) and (Im) are the real and imaginary components of the x-ray SLD, respectively.

layers	thickness (nm)	ρ_m ($\times 10^{28}$ m^{-3})	(Mn_xSi_{1-x})	X-ray SLD (Re) (nm^{-2})	X-ray SLD (Im) (nm^{-2})	Neutron SLD (Re) (nm^{-2})	σ_R (nm)
SiO_2 + vac	2.55	0.994	N/A	8.51×10^{-4}	2.98×10^{-6}	1.57×10^{-4}	1.03
Si + vac	18.65	3.500	N/A	1.41×10^{-3}	7.14×10^{-5}	1.45×10^{-4}	2.80
MnSi + Si	24.48	6.406	0.450	3.41×10^{-3}	3.42×10^{-5}	3.87×10^{-5}	0.93
MnSi + $MnSi_{1.7}$	15.05	8.398	0.330	4.18×10^{-3}	1.16×10^{-3}	1.30×10^{-4}	7.92
$MnSi_{1.7}$ + Si	61.27	6.192	0.109	2.69×10^{-3}	1.29×10^{-3}	2.04×10^{-4}	0.49
Si(111)	N/A	5.000	N/A	2.01×10^{-3}	4.58×10^{-5}	2.08×10^{-4}	1.01

Table 4.2. Layer parameters used to fit both PNR and XRR scattering length densities to a single model to determine chemical structure of a 20-nm Si / 39.5-nm MnSi / Si(111) film.

magnetic moment / unit cell. The small drop in magnetic moment with depth was included to account for the drop in the MnSi concentration due to the $MnSi_{1.7}$ precipitates. In summary, PNR of the 39.5-nm thick film finds evidence of a conical magnetic phase

in low fields with a wavelength of 14.0 ± 0.5 nm, which is in agreement with the result from the SQUID measurements, which find $2\pi / Q$ = 13.9 ± 0.1 nm. These results raise the question of the origin in the reduction in wavelength. Given that $Q = SD_0 / A$ (Eq. (1.8)), there are three possible origins: an increase in M_{sat}, or D_0, or a decrease in A. An analysis of the energetics of the reorientation of the helix in a transverse field is able to address this issue.

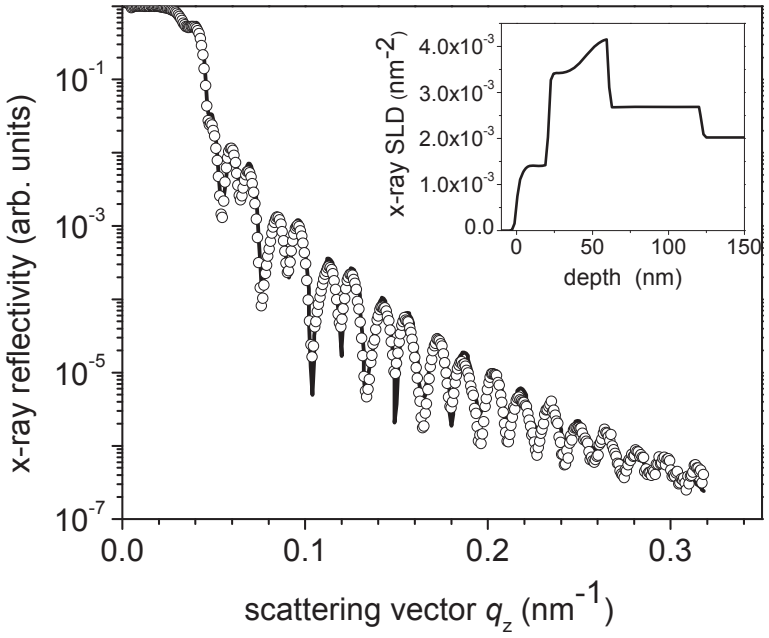

Figure 4.18. X-ray reflectivity data from a 20-nm Si / 39.5-nm MnSi / Si(111) film containing $MnSi_{1.7}$ precipitates. The fit generated from the model is represented by the solid line and the inset is the x-ray SLD used to fit the data.

4.4 Spin Reorientation in MnSi Thin Films

A characterization of the response of the MnSi thin films to an in-plane field is important for testing the models of the fundamental interactions in the films. For MBE grown thin films, the $M - H$ curves in Fig. 4.19 show a departure of the magnetic behaviour of the MnSi in an in-plane magnetic field compared to bulk crystals. The first

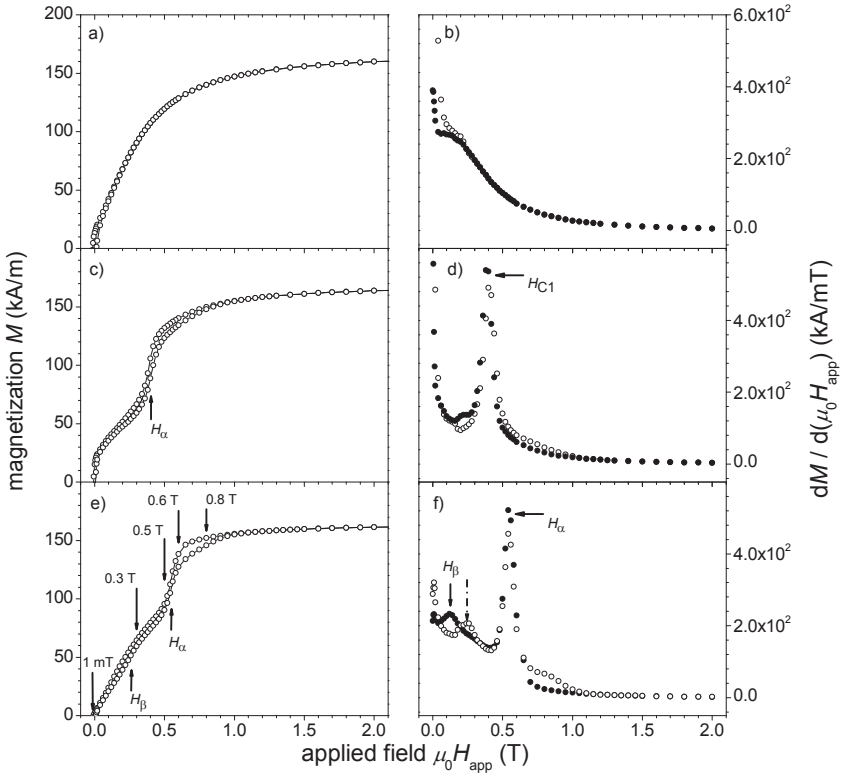

Figure 4.19. SQUID $M - H$ curves and the corresponding $dM/d(\mu_0 H_{app})$ with an applied field in the $[1\,\bar{1}\,0]$ (in-plane) orientation for three MBE grown films a) – b) 11.6 nm, c) – d) 17.6 nm, e) – f) 26.7 nm. Open symbols represent data measured with an increasing field and solid symbols represent the hysteresis branch measured on decreasing the field.

difference is the existence of a remanent magnetization, which was discussed in Chapter 3. Another difference between the MBE films and bulk crystal is the presence of a first-order-like step in the magnetization. For samples with MnSi thicknesses between 12.8 nm and 25.4 nm, a sharp kink in the $M - H$ curves was observed at a field labelled

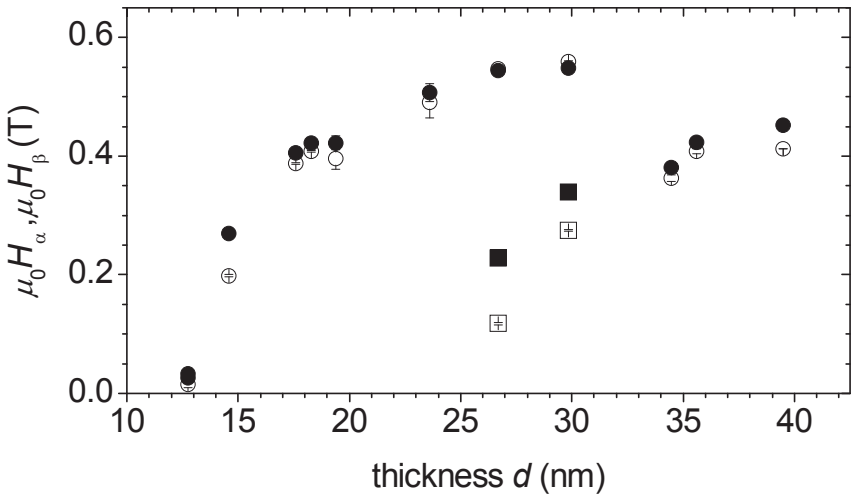

Figure 4.20. H_α (solid and open circles) and H_β (solid and open squares) extracted from the dM/d($\mu_0 H_{app}$) of the SQUID measurements with the magnetic field along $[1\,\bar{1}\,0]$ as shown from Fig. 4.19 (d) and (f). The open (closed) symbols show H_α and H_β calculated from the decreasing (increasing) H branch.

H_α, as shown in Fig. 4.19 (c) and (d), which are dependent on the film thickness, as shown in Fig. 4.20. An additional discontinuity was observed for two samples, shown in Fig. 4.20 by square symbols, at an applied field that is labelled H_β (Fig. 4.19 (e) and (f)). There is no evidence of a kink in the $M - H$ loops for samples less than 11.6 nm in thickness (Fig. 4.19 (a) and (b)).

The values for H_α obtained from a Gaussian fit to the peak in $dM/d(\mu_0 H_{app})$ (Fig. 4.19 (d) and (f)), are shown in Fig. 4.20, for both the increasing field branch and decreasing field branch of the $M - H$ curves. The onset of $\mu_0 H_\alpha$ in the $M - H$ loops occurs at a thickness slightly less than $2\pi/Q$, whereas the onset of the $\mu_0 H_\beta$ occurs at a thickness a little less than $4\pi/Q$. It is not possible to explain these two transitions with Plumer and Walker's model, despite its success in bulk MnSi, as briefly discussed in Chapter 1. Their solutions to a Landau-like free energy are not able to account for the large values of H_α relative to H_{C2} [111] [34].

The knee in the out-of-plane [111] $M - H$ loops (Fig. 4.21), which is determined from the minimum in $d^2M / d\left(\mu_0 H_{app}\right)^2$, is used as a measure of $H_{C2}[111]$ and is plotted as a function of thickness in Fig. 4.22. Since an out-of-plane uniaxial anisotropy, K_u, was expected from the epitaxially induced out-of-plane strain, the $H_{C2}[1\,\bar{1}\,0]$ as a function of thickness was also determined. Ishikawa *et al*. reported that H_{C2} is independent of field orientation, which is explained by the low anisotropy in bulk MnSi [29, 31]. In the films, this is not the case: H_{C2} is larger for the out-of-plane measurements. There was a clear minimum in $d^2M / d\left(\mu_0 H_{app}\right)^2$ for films thicker than 14.6 nm at a field near the knee in the $M - H$ data, which was assigned $H_{C2}[1\,\bar{1}\,0]$ (Fig. 4.21). The second derivates were

calculated from the increasing field branch of the hysteresis loops since they provided sharper transitions. In the two thinnest samples in Fig. 4.22, there was no clear minimum in $\mathrm{d}^2M / \mathrm{d}\left(\mu_0 H_{\mathrm{app}}\right)^2$ due to the rounding of the $M - H$ curves. In these two cases, the knee in the $M - H$ loops was determined by extrapolating the low field $M(H)$ data to the field where it reaches the saturation magnetization.

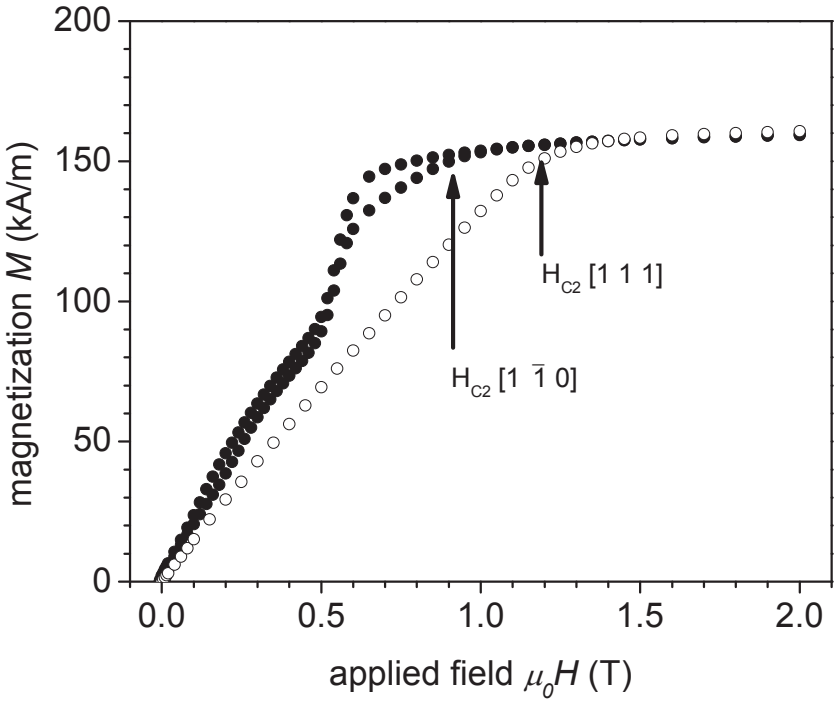

Figure 4.21. $M - H$ loops of a 20 nm Si/26.7 nm MnSi/ Si (111) thin film. The solid circles represent the data generated in an applied field oriented in the $[1\,\bar{1}\,0]$ in-plane direction and the open circles represent the data generated in an applied field oriented in the [111] out-of-plane direction

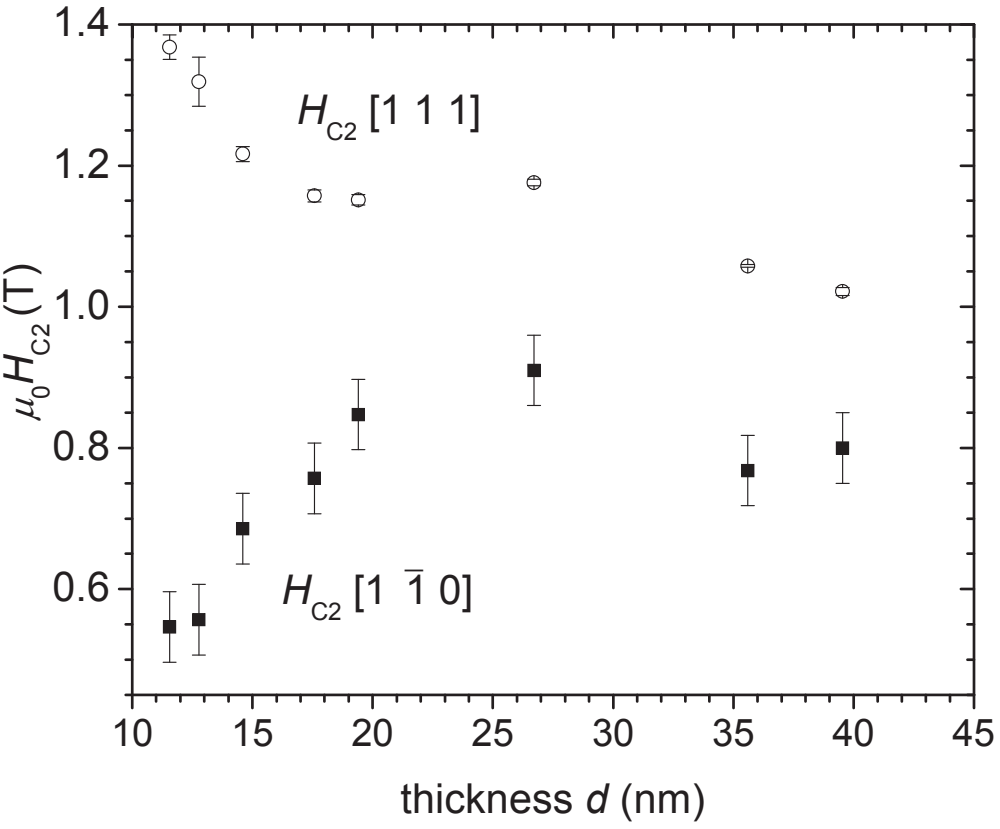

Figure 4.22. A plot of H_{C2} as a function of MnSi film thickness d for both the [111] (solid circles) and [1 $\bar{1}$ 0] (open squares) directions. H_{C2} was calculated from the minimum in $\mathrm{d}^2M / \mathrm{d}\left(\mu_0 H_{\mathrm{app}}\right)^2$ of the $M - H$ curves.

Fig. 4.22 compares the critical field H_{C2} in both the [111] and [1 $\bar{1}$ 0] directions. The uniaxial MCA constant is obtained from the measurement of H_{C2} through Eq. (1.16) and Eq. (1.17),

$$K_u = \frac{M_{\text{sat}}}{3}\left(\mu_0 H_{\text{C2}}^{[111]} - \mu_0 H_{\text{C2}}^{[1\text{-}10]} - \mu_0 M_{\text{sat}} - \frac{K_m}{M_{\text{sat}}}\right), \tag{4.1}$$

and is shown in Fig. 4.23, where the small anisotropic exchange term contribution discussed in Chapter 1 is neglected.

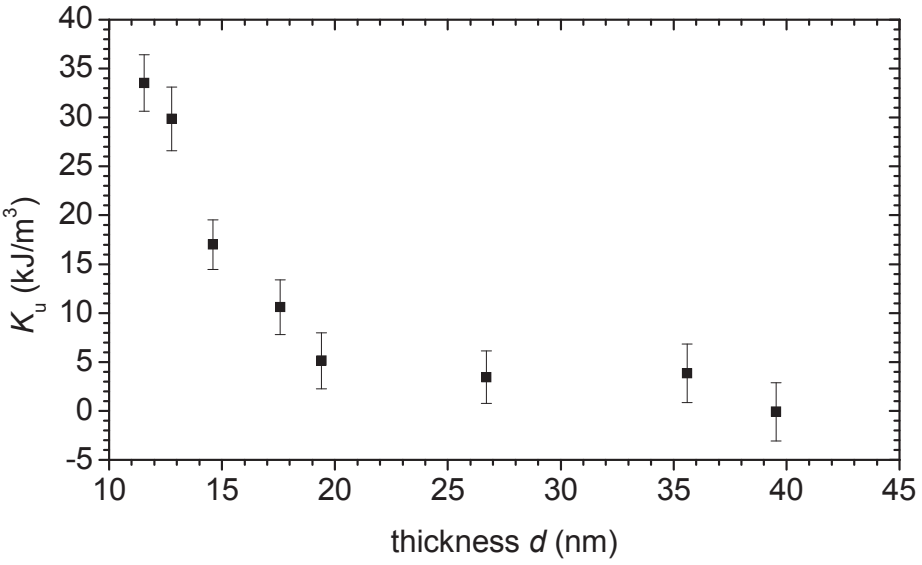

Figure 4.23. The uniaxial magnetocrystalline anisotropy for MBE samples extracted from the H_{C2} in Fig. 4.22 using Eq. (4.1).

An interesting question to address is the origin of K_u. A uniaxial MCA is expected based on the trigonal distortion of the films. By assuming that K_u is of purely magnetostatic origin, the effective magnetoelastic shear stress $B_{2,\text{eff}}$ was calculated, from Eq. (1.30), as shown in Fig. 4.24. $B_{2,\text{eff}}$ is found to be dependent on strain, as found in other thin films [57]. Others have used a phenomenological model to describe the dependence of $B_{2,\text{eff}}$ on strain,

$$B_{2,eff}(\varepsilon) = B_2 + D_2(\varepsilon_\perp - \varepsilon_\parallel), \tag{4.2}$$

for small values of strain. The data in Fig. 4.24 clearly does not follow a simple linear relationship. However, for comparison with the literature and with theory a linear fit was made to a subset of data points [57]. To determine which points to include, multiple fits were performed, each time increasing the number of points in the fit and using the reduced χ^2 per degree of freedom as a test of the model. The two samples with the highest strain were neglected, since these two points were more than 3 σ from the fit when these points were excluded and produced a poor χ^2 / DOF when included in the fit. The remaining 6 data points produced a fit with a χ^2 / DOF = 4.8, which is high due to the two data points that are about 3 σ from the fit. The 14.6 nm and 26.7 nm samples were each considered for possible exclusion from the fit. In Fig. 4.24, two fits are presented which show either a 14.6 nm or a 26.7 nm sample removed from the fit. When the 14.6 nm data point was removed from the fit, the parameters B_2 = 0.3 ± 2.4 MJ/m^3 and D_2 = 118 ± 234 MJ/m^3 with a χ^2 / DOF = 1.57 were determined, as shown by the solid line. In the second case a 26.7 nm sample was removed which had a high strain, due to the high purity of the sample, the parameters B_2 = 2.56 ± 0.83 MJ/m^3 and D_2 = 385 ± 65 MJ/m^3 with a χ^2 / DOF = 0.51 was found, as shown by the dashed line. In both cases the parameters are comparable to the magnitude of the magnetoelastic stress coefficients B_1 = -3 MJ/m^3 and D_1 = 1000 MJ/m^3 reported for Fe on W[100] by Sander *et al*. [57]. The samples with the highest strain deviate from the linear fit. However, a similar behaviour has been observed in other thin films when the strains are greater than $\simeq 1\%$ [57]. No values for B_2 for MnSi have been found in the literature. However, for an isotropic medium, $2B_2$ is equal to the magnetoelastic stress,

B_1. [86] An analysis of the magnetostriction data reported by Fawcett *et al*. [87], with the correction to the scale in their plot of the low-field magnetostriction data pointed out by Franus-Muir *et al*. [88] led to a value of $B_1 \simeq 1\ \mathrm{MJ/m^3}$ for bulk MnSi at low temperature. The value for B_2 for bulk crystals is smaller than the value extracted for the strained thin

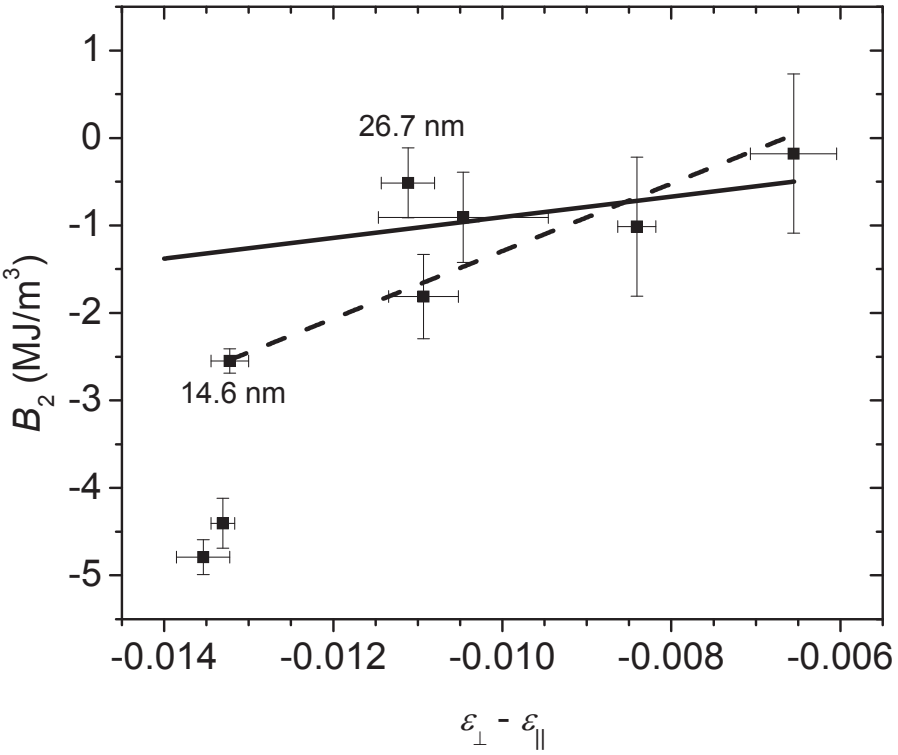

Figure 4.24. $B_{2,eff}$ for MBE samples, extracted from K_u in Fig. 4.23 as a function of the difference between the out-of-plane and in-plane strain $\varepsilon_\perp - \varepsilon_{||}$ with ± 1σ error bars. The solid line is a fit to the data with Eq. (4.2) neglecting 2 samples with the highest strains and a 14.6 nm sample. The dashed line is a fit to the data with Eq. (4.2) neglecting 2 samples with the highest strain and a 26.7-nm sample.

film. However, the magnetoelastic properties of thin films are known to be significantly different than bulk [57].

The DFT calculated value $B_2^{\mathrm{DFT}} = 2.6\ \mathrm{MJ/m^3}$ reported by Rößler and Bogdanov [58] is in reasonable agreement with the experimental value, which supports the conclusions that the K_u is of magnetoelastic origin. In addition, the calculations predict that an in-plane tensile strain will produce an easy-plane anisotropy ($K_u > 0$), which is also in agreement with the experimental results.

The effective stiffness of the conical phase, K_0, was calculated by adding Eq. (1.16) and Eq. (1.17), and by neglecting the small anisotropic exchange term:

$$K_0 = \frac{M_{\mathrm{sat}}}{6}\left(\mu_0 H_{\mathrm{C2}}^{[111]} + 2\mu_0 H_{\mathrm{C2}}^{[1\text{-}10]} - \mu_0 M_{\mathrm{sat}} + \frac{2K_m}{M_{\mathrm{sat}}}\right). \tag{4.3}$$

From K_0, the spinwave stiffness A was obtained, as shown in Fig. 4.25. The spinwave stiffness is nearly constant over the range 11 nm – 40 nm in MnSi thickness, with an average value of A = 0.45 ± 0.01 meV nm^2, compared to the bulk value $A \simeq 0.50$ meV nm^2 [30, 31, 37]. This is consistent with a nearly constant T_C shown in Fig. 4.8 over a thickness range of d = 10 – 40 nm. From Eq. (1.8), a value of SD_0 = 0.22 ± 0.01 meV nm is found if the small anisotropic exchange interaction term is neglected, which is larger than the bulk value of 0.18 meV nm. However, $SD_0/(\mu_{\mathrm{film}}\ a_{\mathrm{MnSi}})$ = 1.06 ± 0.3 meV/μ_B is within error limits with values of 1.15 ± 0.1 meV/μ_B found in $Mn_{1-x}Fe_xSi$ and $Fe_xCo_{1-x}Si$ B20 alloys [40, 89]. This analysis shows that the increase in moment, the decrease in A and the increase in D_0 all contribute to the observed reduction in wavelength $2\pi / Q$.

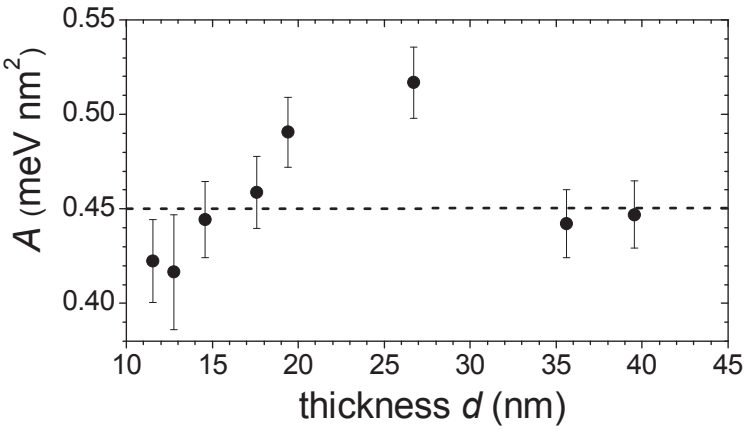

Figure 4.25. The spinwave stiffness A as a function of thickness is calculated from $H_{C2}[111]$ and $H_{C2}[1\,\bar{1}\,0]$ in Fig. 4.22. The average spinwave stiffness $A = 0.45 \pm 0.01$ meV nm^2 is shown by the dashed line.

In order to understand the magnetic structure during reorientation and the origin of H_α and H_β, a series of PNR measurements at 1 mT, 0.3 T, 0.5 T, 0.6 T and 0.8 T were performed, with an experimental geometry as shown in Fig. 4.26, on the 20-nm Si / 26.7-nm MnSi / Si (111) sample, as shown in Fig. 4.28 – Fig. 4.31 and Fig. 4.34. The NG-1 reflectometer was used in order to determine a depth profile of the magnetization

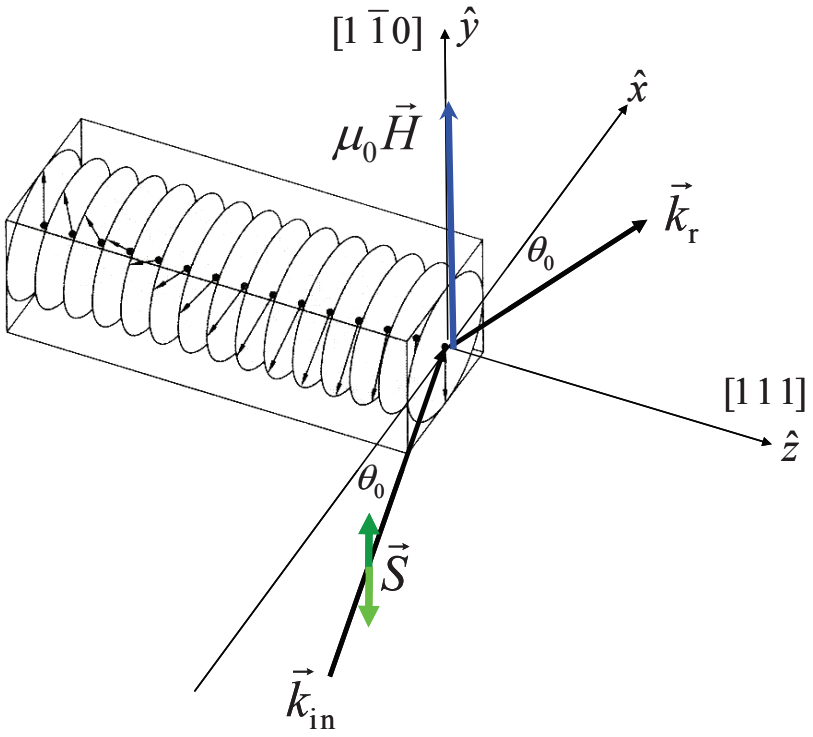

Figure 4.26. Schematic diagram showing the experimental geometry of a PNR measurement of a 20 nm Si/26.7 nm MnSi/ Si (111) film.

for a range of applied magnetic fields. The quantization axis of the neutron spin is set by the field applied along the in-plane MnSi [1 $\bar{1}$ 0] direction, which is labelled the *x*-axis, while the film normal points along the *z*-axis. The sample is field cooled to 7 K in an in-plane field $\mu_0 H_{app}$ = 0.8 T.

All four scattering cross-sections R(+ +), R(– –), R(+ –), and R(– +) were measured. However, only a small spin-flip (SF) signal was observed in this orientation. If a single chiral domain exists on the film, a peak would be observed in one of the SF channels since SF is sensitive to the perpendicular component of the magnetization. Since only a small SF-signal was observed, this indicated that there is nearly complete

cancellation of the perpendicular component of the magnetization due to the nearly equal amounts of left- and right-handed domains [90].

XRR measurements were performed to determine the chemical structure of the thin film shown in Fig. 4.27. From the x-ray scattering length density (SLD) profile, A film thickness of 26.7 nm was determined, as shown in Table 4.3. As seen in the inset in Fig. 4.27, the sharp interfaces indicated small interfacial roughness less than 0.5 nm at the MnSi/Si (111) interface and less than 0.8 nm at the MnSi/amorphous Si cap interface.

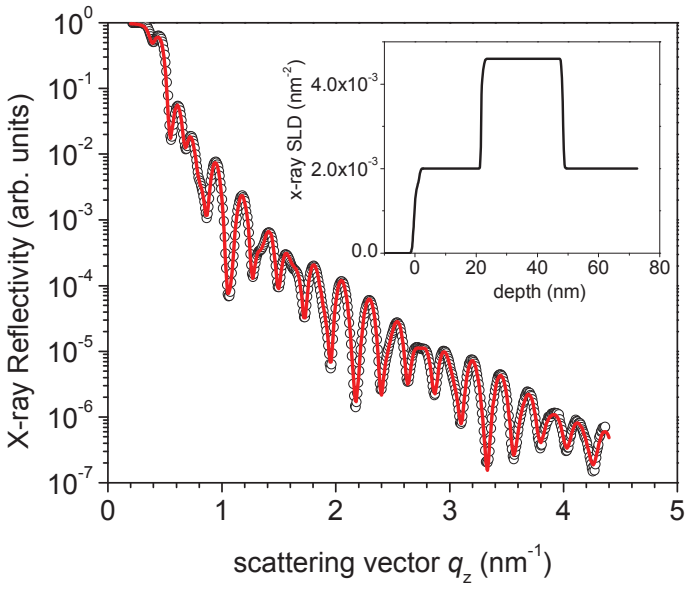

Figure 4.27. XRR measurement of a 20-nm Si / 26.7-nm MnSi / Si(111) film. The solid line corresponds to the fit to the data. The inset shows the x-ray SLD used to fit the data.

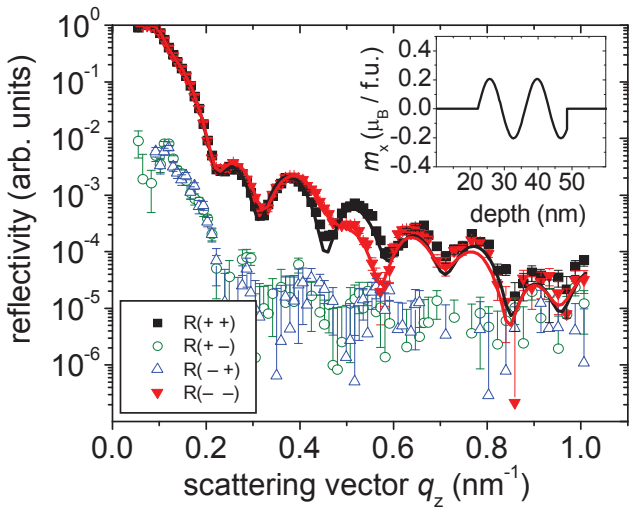

Figure 4.28. PNR measurement with ± 1 σ error bars of 20-nm Si / 26.7-nm MnSi / Si(111) film. The sample was field-cooled to T = 7 K in an applied field of $\mu_0 H_{app}$ = 1 mT. The solid lines show a fit to the data. The experimental geometry is shown in Fig. 4.26. The inset shows the magnetic moment distribution with respect to film depth.

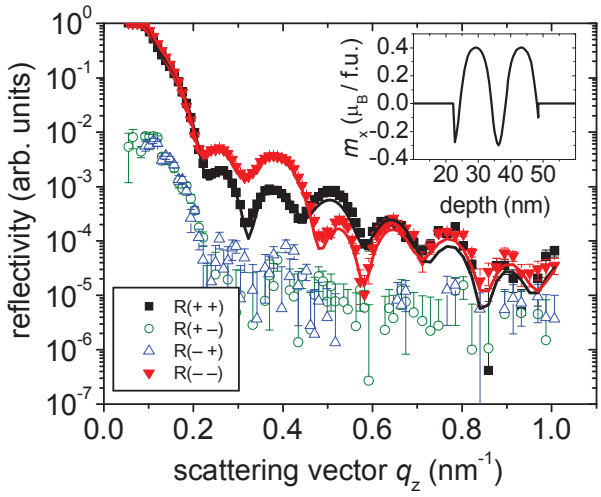

Figure 4.29. PNR measurement with ± 1 σ error bars of 20-nm Si / 26.7-nm MnSi / Si(111) film. The sample was measured at T = 7 K in an applied field of $\mu_0 H_{app}$ = 0.3 T. The solid lines show a fit to the data. The experimental geometry is shown in Fig. 4.26. The inset shows the magnetic moment distribution with respect to film depth.

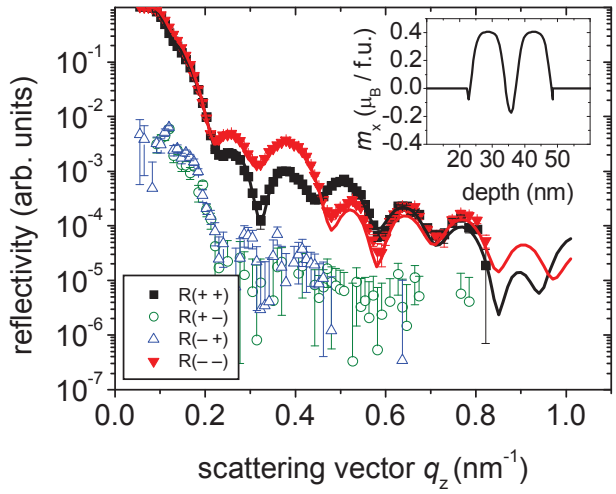

Figure 4.30. PNR measurement with ± 1 σ error bars of 20-nm Si / 26.7-nm MnSi / Si(111) film. The sample was measured at T = 7 K in an applied field of $\mu_0 H_{app}$ = 0.5 T. The solid lines show a fit to the data. The experimental geometry is shown in Fig. 4.26. The inset shows the magnetic moment distribution with respect to film depth.

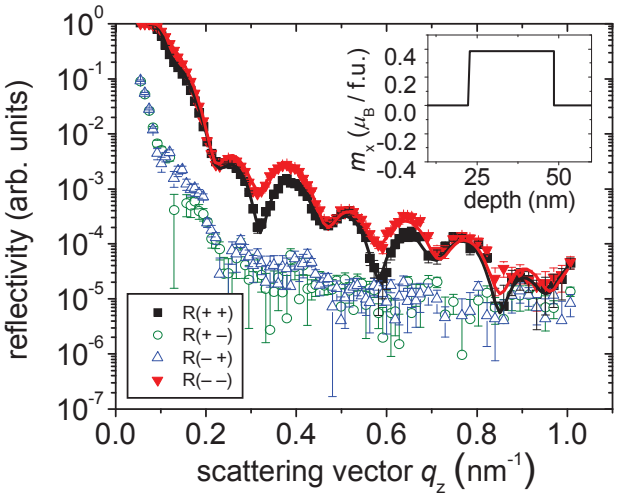

Figure 4.31. PNR measurement with ± 1 σ error bars of 20-nm Si / 26.7-nm MnSi / Si(111) film. The sample was measured at T = 7 K in an applied field of $\mu_0 H_{app}$ = 0.8 T. The solid lines show a fit to the data. The experimental geometry is shown in Fig. 4.26. The inset shows the magnetic moment distribution with respect to film depth.

X-ray diffraction measurements shown in Fig. 2.6 were also performed on the film. Fits to the Kiessig oscillations measured about the MnSi (111) peak agreed with the thickness determined from the XRR fit. Plan view TEM images of this sample showed evidence of only a small amount (~1.0%) of $MnSi_{1.7}$ precipitates.

Layers	Thickness d (nm)	ρ_m ($\times 10^{28}$ m^{-3})	f' (fm)	f'' (fm)	σ_R (nm)
Si Substrate	0	4.996	14.3	0.325	0.47
MnSi	26.33	8.436	19.4	1.5775	0.76
MnSi + Si	0.38	7.04	18.6	1.38	0.27
Si	20.31	4.996	14.3	0.325	0.68
SiO_2	1.56	1.76	30.39	0.39	0.55
Vacuum	0	0	0	0	0

Table 4.3. Layer parameters used to fit XRR scattering length densities to determine chemical structure of a 20-nm Si / 26.7-nm MnSi / Si(111) film.

The SLD from the fit to the XRR data gave the component of the neutron SLD. The magnetic component served as the fitting parameter for the PNR data. A uniform magnetic SLD is able to fit the spin-polarized neutron data measured in a field of 0.8 T. The moment 0.38 μ_B / Mn extracted from the fit, shown in the inset in Fig. 4.31, is slightly lower than the saturated magnetization of 0.42 ± 0.01 μ_B / Mn for the film. This value is explained by a conical phase with $Q \parallel [1\,\bar{1}\,0]$ where the component of the magnetization in the field direction is given by the cone angle $\alpha = \sin^{-1}(M / M_{sat}) = 65 \pm 1°$. The PNR determined value agrees well with the SQUID measurement of $\alpha = \sin^{-1}(H / H_{C2}[1\,\bar{1}\,0]) = 62 \pm 3°$.

In an applied field of 1 mT oriented in the in-plane $[1\,\bar{1}\,0]$ direction (Fig. 4.28), the Q-vector is pointing in the out-of-plane [111] direction. An oscillatory magnetic SLD profile with a period of $2\pi/Q = 13.9 \pm 0.01$ nm provides a good fit to the data, which is consistent with the out-of-plane measurement [90]. The size of the average in-plane magnetic moment 0.20 μ_B / Mn is smaller than the saturation value due to the presence of domains.

At 0.3 T, the SLD profile shown in Fig. 4.29 displays a distortion to the sinusoidal SLD, which becomes greater at 0.5 T, as shown in Fig. 4.30. A Fourier analysis of the SLD shows that the distortions can be described with the addition of a second harmonic. In order to fit the PNR data obtained at 0.5 T, a model generated using Simulreflec software, consisting of five layers including roughness produced the magnetic SLD shown in Fig. 4.32. Fourier analysis of the SLD shows the presence of a second harmonic, which is not surprising given that in bulk MnSi evidence of higher harmonics were observed when an applied field was oriented in the [110] direction [30, 31] and was predicted by Plumer and Walker [34]. The magnetization is also larger in the direction of the field than in the anti-parallel direction, which produces a net magnetization that agrees with M(H) plotted in Fig. 4.19 (e).

Given that PNR averages the magnetic moments in-plane, and given the fact that PNR is well described by a layered magnetic structure, indicates that the wavefronts of the SDW must be in the plane of the film. One possible magnetic structure that would explain the PNR data is a skewed helix [91], where the helical SDW wavefronts remain perpendicular to the film normal. The component of the magnetic moment along the field

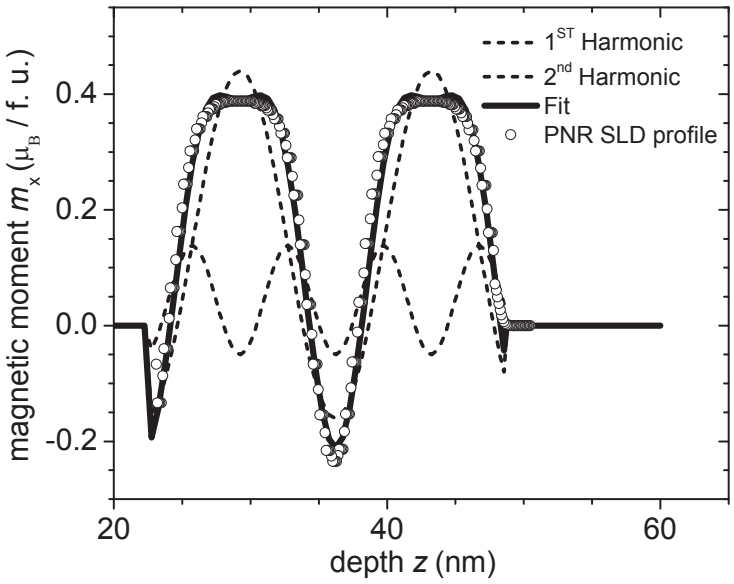

Figure 4.32. PNR SLD profile of a 20 nm Si/26.7 nm MnSi/ Si(111) film. Simulreflec software generated the SLD profile (solid circles) from the PNR data measured at 0.5 T oriented along the $[1\,\bar{1}\,0]$ in-plane direction. The 1st (long dashed line) and 2ND (short dashed line) harmonics are shown. A fit to the data generated from the harmonics is shown by the solid line.

direction is given by:

$$m_x = m_0 \sin(\alpha)\sin(\theta) + m_0 \cos(\alpha)\cos(\theta)\cos(Qz). \tag{4.4}$$

The PNR data in this case would be interpreted by a field-induced rotation, θ, of the propagation vector towards $[1\,\bar{1}\,0]$ together with a canting, α, of the moments towards the propagation vector, as shown in Fig. 4.33. The SLD was fit to a 14-nm harmonic spin-density wave with an amplitude of $\mu_1 = 0.42\mu_B / \mathrm{Mn}$ wave together with a $\mu_2 = 0.12\mu_B / \mathrm{Mn}$ second harmonic. The fit to the SLD is shown in Fig. 4.32.

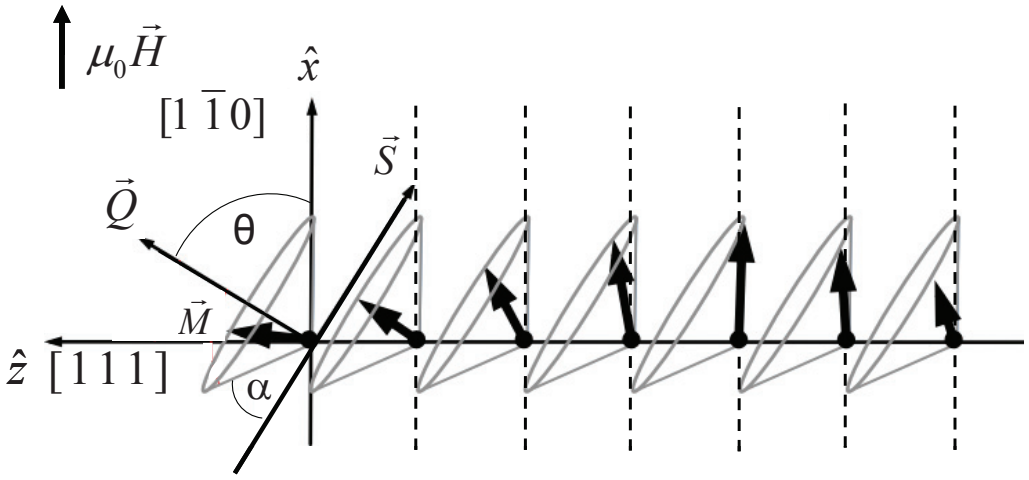

Figure 4.33. Diagram of a skewed conical phase in an in-plane magnetic field, where $\hat{z}$ is the [111] out-plane film direction and $\hat{x}$ is the direction of the applied magnetic field, $\mu_0\vec{H}$. The wavefronts of this phase represented by the dashed lines, remain parallel to the surface while the axis of the cone, $\vec{Q}$, cants in the direction of the field by an angle θ.

However, the model did not fit the PNR data at an applied field immediately above H_{C1} = 0.54 T. At 0.6 T, the reflectivity at low scattering vector drops more quickly than any layered model can produce, as shown in Fig. 4.34. In order to transition between the skewed structures with wavefronts perpendicular to the surface normal, to a conical structure with the wavefronts perpendicular to the in-plane field direction, the wavefront would need to rotate away from the film normal. This would result in off-specular magnetic scattering that would decrease specular reflectivity. However, a skewed conical helix is not a solution to Eq. (1.31).

Rößler and Bogdanov found the magnetic solutions to Eq. (1.31) by direct minimization and testing the stability of the solutions. They have found the four magnetic phases shown in Fig. 1.7, and determined the phase diagram shown in Fig. 4.35 [58].

However, there may be other interactions, e.g., surface anisotropies, or perhaps the strain induced changes that modify the phase diagram. These unknown interactions may stabilize the skewed conical phase.

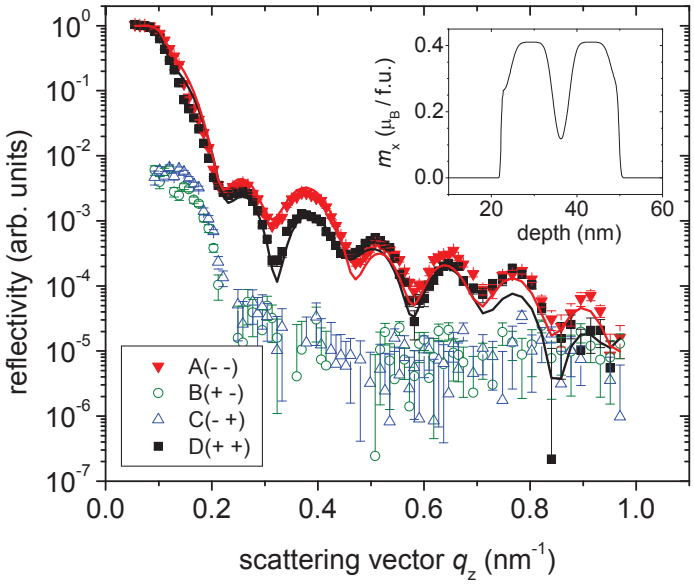

Figure 4.34. PNR measurement with ± 1 σ error bars of 20 nm Si/ 26.7 nm MnSi/ Si(111) film. The sample was measured at T = 7 K in an applied field of $\mu_0 H$ = 0.6 T. The solid lines show a fit to the data. The experimental geometry is shown Fig. 4.26. The inset shows the magnetic moment distribution with respect to film depth.

This phase diagram shows the possible magnetic modulations in an almost isotropic chiral magnet with an easy plane anisotropy, which include a helicoidal phase, a conical phase and a skyrmion lattice. Around a triple point, all three structures can exist simultaneously. Superimposed on this graph are the experimental values of the critical field $H_{C2}^{[1\text{–}10]}$ and H_α. Although there is good agreement between experiment and theory

at the critical field $H_{C2}^{[1\bar{1}0]}$, as shown in Fig. 4.35, the magnetic behaviour at the field H_α cannot be explained by this model. Fig. 4.35 shows the measured critical fields cross all three magnetic phases predicted by Eq. (1.31) for a film with a uniaxial anisotropy, but H_α does not correspond to any of the predicted transition lines. Based on the experimental observations, it is not possible to answer the question of which magnetic structures are responsible for the anomalous field-driven evolution in the experiments.

Further theoretical and experimental work needs to be performed in order to explain the complex magnetic behaviour observed in the MnSi thin films. Since Eq. (1.31) does not account for cubic anisotropy, ferromagnetic resonance should be performed in order to determine whether the cubic anisotropy is negligible. In addition, surface anisotropy should be determined from a complete FMR study to determine if such anisotropies are affecting the magnetic structure. Furthermore, since the Dzyaloshinskii-Moriya interaction results from spin-orbit interaction, these studies raise the question whether a trigonal distortion will break the invariance of the DM interaction that would introduce additional corrections to the model. Lorentz microscopy and spin-polarized STM imaging are also important in order to discriminate between the different magnetic phases and to understand the magnetic phase diagram, shown in Fig. 4.35. Eq. (1.31) also does not take into account the finite size of the film, which may stabilize skyrmions and explain H_β. If skyrmions exactly fit into the film, they are more stable [92].

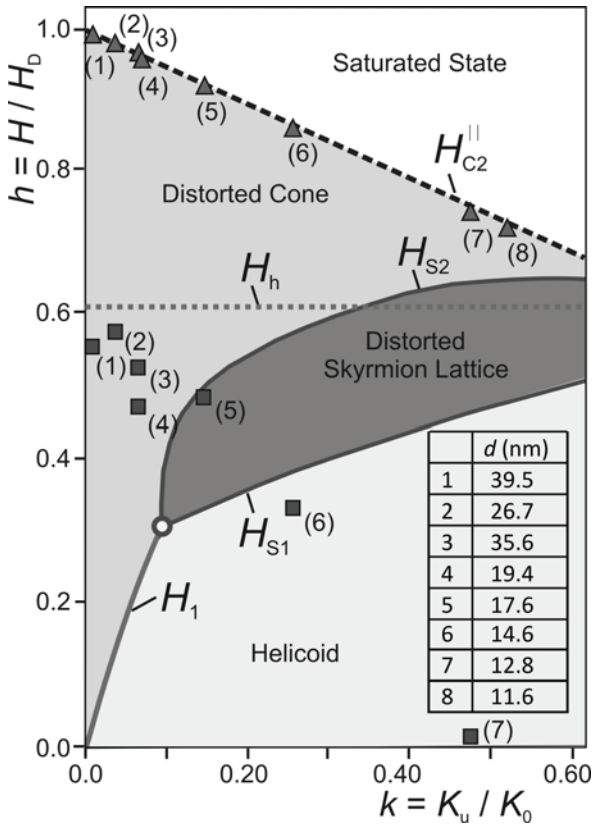

Figure 4.35. Low anisotropy range of the magnetic phase diagram in reduced variables for uniaxial anisotropy $K = K_u / K_0$ and applied magnetic field $H = H / H_D$ for the model described by Eq. (1.34) with an in-plane magnetic field ($H_D = 2K_0 / M_{sat}$ is the saturation field for a bulk cubic helimagnet with K_u = 0. (Eq. (1.16)). [58] The helical and skyrmionic states are indicated by different shades of grey. Solid lines designate the first-order transitions: H_1 represents the transition between helicoid and distorted cone. The dashed line indicates the critical field $H_{C2}^{[1-10]}$ (Eq. (1.17)) for the distorted cone phase. Triangles and squares show experimental values of critical fields $H_{C2}^{[1-10]}$ and H_α, respectively, for MnSi films of different thickness, *d*. (Courtesy of Dr. U. K. Rößler and Prof. A. N. Bogdanov, Leibniz Institute for Solid State and Materials Research)

Chapter 5 - Conclusion

Epitaxial MnSi (111) thin films were grown on Si(111) substrates by the methods of SPE and MBE and careful control of the annealing temperature produced precipitate-free SPE films. However, as the films increased in thickness, the interface roughness at the film boundaries also increased and direct evidence of the helical nature of the magnetic properties of the film were not observed. In the case of MBE grown samples, there was a significant improvement at the MnSi film interfaces, which was observed by the increased amplitude of the Kiessig fringes in both the XRR and XRD data. PNR measurements were able to provide direct evidence of the helical nature for the MnSi(111) films. Although MBE growth generated $MnSi_{1.7}$ precipitates that were observed in many of the samples, the low magnetic moment of the $MnSi_{1.7}$ precipitates did not affect the magnetic measurements of the samples significantly.

Evidence of a correlation between the crystalline structure and the magnetic properties of the MnSi(111) thin films was shown. The lattice mismatch between epitaxial MnSi(111) thin films and the Si(111) substrate induces a biaxial stress on the film that causes a volume expansion of the MnSi lattice. The MBE thin films were found to have a higher volume strain and T_C than SPE films of a similar thickness. The presence of $MnSi_{1.7}$ precipitates in the MBE grown films was not observed to affect the enhanced T_C in the films. Both SPE (for films less than 9 nm) and MBE (for films less than 11 nm) grown samples displayed a similar drop in T_C and κ / c_{44} with decreasing thickness that could not be explained by finite-size scaling arguments. The strong correlation between T_C and κ / c_{44} suggests that their anomalous behaviour has a common origin. Interstitial

defects could explain both the observed changes in elastic and the magnetic properties of the film.

With the higher interface quality in the MBE samples, PNR and SQUID measurements of MnSi(111) thin films show clear evidence of helical magnetic order with the propagation vector $\vec{Q}$ oriented along the [111] direction in zero field with a constant wavelength of $2\pi/Q = 13.9 \pm 0.1$ nm in the thickness range $d = 7 - 40$ nm. TEM observations of structural inversion domains that occur in the thin films with equal probability imply the existence of left and right-handed magnetic chiral domains with equal sample coverage. The glassy behaviour that was observed can be attributed to the frustration between the magnetic chiral domains.

PNR and SQUID measurements of MnSi thin films performed in an in-plane magnetic field show a complex magnetic behaviour. In-plane tensile strain in MnSi(111) films produced an easy-plane uniaxial anisotropy, which is shown to be due to a magnetoelastic effect. Experimental results combined with theoretical results described by a Dzyaloshinskii model [56] reveals the existence of numerous magnetic modulated states that are either metastable or do not exist in bulk MnSi. A change in the value of the uniaxial anisotropy changes the type of magnetization process found and the experimental data presented gives a clear indication for such processes in the MnSi films. In order to explore the complex anisotropic structure in the MnSi(111) thin films under epitaxial strain, ferromagnetic resonance measurements need to be performed. Lorentz microscopy and spin-polarized STM imaging are also important characterization techniques that could be used to discriminate between the different chirally modulated states and to understand the magnetic phase diagram. Since the simple model presented in

this thesis cannot explain the magnetic behaviour observed in the MnSi(111) thin films, greater understanding of the additional interactions that affect the magnetic order will be necessary in order to model the epitaxially strained MnSi(111) thin films, which could include higher-order anisotropies and surface effects.

However, this thesis demonstrates that MnSi thin films are an interesting system where modulated chiral magnetic states can be studied. Given that these films are grown epitaxially on insulating Si wafers, they open the opportunity to investigate spin-dependent transport in chiral magnetic heterostructures.

References

[1] G. Binasch, P. Grünberg, F. Saurenbach, and W. Zinn "Enhanced magnetoresistance in layered magnetic structures with antiferromagnetic interlayer exchange" *Phys. Rev. B*, **39**, 4828 (1989)

[2] M. N. Baibich, J. M. Broto, A. Fert, F. Nguyen , Van Dau, F. Petrof, P. Eitenne, G. Creuzet, A. Friederich, and J. Chazelas, "Giant Magnetoresistance of (001)Fe/(001)Cr Magnetic Superlattices", *Phys. Rev. Lett.*, **61**, 2472 (1988)

[3] L. Berger, "Emission of spin waves by a magnetic multilayer traversed by a current", *Phys. Rev. B,* **54**, 9353 (1996)

[4] J. C. Slonczewski, "Current-driven excitation of magnetic multilayers", *J.Magn. Magn. Mat.,* **159,** L1 (1996)

[5] M. Tsoi, R. E. Fontana, and S. S. P. Parkin, "Magnetic domain wall motion triggered by an electric current", *Appl. Phys. Lett.*, **83**, 2617 (2003)

[6] E. B. Myers, D. C. Ralph, J. A. Katine, R. N. Louie, and R. A. Buhrman, "Current-Induced Switching of Domains in Magnetic Multilayer Devices", *Science*, **285**, 867 (1999)

[7] J. Grollier, P. Boulenc, V. Cros, A. Hamzić, A. Vaurès, A. Fert, and G. Faini, "Switching a spin valve back and forth by current-induced domain wall motion", *Appl. Phys. Lett.*, **83**, 509 (2003)

[8] R. O'Handley, *Modern Magnetic Materials Principles and Applications*, (John Wiley & Sons, INC., New York, 2000)

[9] I. N. Krivorotov, N. C. Emley, J. C. Sankey, S. I. Kiselev, D. C. Ralph, and R. A. Buhrman, "Time-Domain Measurements of Nanomagnet Dynamics Driven by Spin-Transfer Torques", *Science*, **307**, 228 (2005)

[10] S. I. Kiselev, J. C. Sankey, I. N. Krivorotov, N. C. Emley, R. J. Schoelkopf, R. A. Buhrman, and D. C. Ralph, "Microwave oscillations of a nanomagnet driven by a spin-polarized current", *Nature*, **425**, 380 (2003)

[11] J. Heurich, J. König, and A. H. MacDonald, "Persistent spin currents in helimagnets", *Phys. Rev. B,* **68**, 064406 (2003)

[12] O. Wessely, B. Skubic, and L. Nordström, "Current Driven Magnetization Dynamics in Helical Spin Density Waves", *Phys. Rev. Lett.*, **96**, 256601 (2006)

[13] O. Wessely, B. Skubic, and L. Nordström, "Spin-transfer torque in helical spin-density waves", *Phys. Rev. B,* **79**, 104433 (2009)

[14] F. Jonietz, S. Mühlbauer, C. Pfleiderer, A. Neubauer, W. Münzer, A. Bauer, T. Adams, R. Georgii, P. Böni, R. A. Duine, K. Everschor, M. Garst, and A. Rosch, "Spin Transfer Torques in MnSi at Ultralow Current Densities", *Science*, **330**, 1648 (2010)

[15] C. Pfleiderer, and A. Rosch, "Condensed-matter physics: Single skyrmions spotted", *Nature*, **465**, 880 (2010)

[16] X. Z. Yu, Y. Onose, N. Kanazawa, J. H. Park, J. H. Han, Y. Matsui, N. Nagaosa, and Y. Tokura, "Real-space observation of a two-dimensional skyrmion crystal", *Nature*, **465**, 901 (2010)

[17] M. Lee, W. Kang, Y. Onose, Y. Tokura, and N. P. Ong, "Unusual Hall Effect Anomaly in MnSi under Pressure", *Phys. Rev. Lett.,* **102**, 186601 (2009)

[18] S. Mühlbauer, B. Binz, F. Jonietz, C. Pfleiderer, A. Rosch, A. Neubauer, R. Georgii, and P. Böni, "Skyrmion Lattice in a Chiral Magnet", *Science,* **323**, 915 (2009)

[19] A. Neubauer, C. Pfleiderer, B. Binz, A. Rosch, R. Ritz, P. G.Niklowitz, and P. Böni, "Topological Hall Effect in the A Phase of MnSi", *Phys. Rev. Lett*., **102**, 186602 (2009)

[20] J. E. Jørgensen, and S. E. Rasmussen, "Refinement of the Structure of MnSi by Powder Diffraction", *Powder Diffraction*, **6**, 194 (1991)

[21] T. Jeong, and W. E. Pickett, "Implications of the B20 crystal structure for the magnetoelectronic structure of MnSi", *Phys. Rev. B,* **70**, 075114 (2004)

[22] C. Kittel, *Introduction to Solid State Physics*, 7th Edition, (John Wiley & Sons, Inc. , New York 1996)

[23] M. Hortamani, P. Kratzer, and M. Scheffler, "Density-functional study of Mn monosilicide on the Si (111) surface: Film formation versus island nucleation", *Phys. Rev. B*, **76**, 235426 (2007)

[24] S. Higashi, P. Kocan, and H. Tochihara, "Reactive epitaxial growth of MnSi ultrathin films on Si(111) by Mn deposition", *Phys. Rev. B*, **79**, 205312 (2009)

[25] D. Bloch, J. Voiron, V. Jaccarino, and J. H. Wernick, "The High Field – High Pressure Properties of MnSi", *Phys. Lett. A* **51**, 259 (1975)

[26] Y. Ishikawa, and M. Arai, "Magnetic Phase Diagram of MnSi near Critical Temperature Studied by Neutron Small Angle Scattering", *J. Phys. Soc. Jpn*. **53**, 2726 (1984)

[27] C. Pfleiderer, D. Reznik, L. Pintschovius, H. v. Löhneysen, M. Garst, and A. Rosch, "Partial order in the non-Fermi-liquid phase of MnSi", *Nature*, **427**, 227 (2004)

[28] B. Fåk, R. A. Sadykov, J. Flouquet, and G. Lapertot, "Pressure dependence of the magnetic structure of the itinerant electron magnet MnSi", *J. Phys: Condens. Matter*, **17**, 1635 (2005)

[29] Y. Ishikawa, and K. Tajima, "Helical Spin Structure in Manganese Silicide MnSi", *Solid State Communications*, **19**, 525 (1976)

[30] S. V. Grigoriev, S. V. Maleyev, A. I. Okorokov, Yu. O. Chetverikov, P. Böni, R. Georgii, D. Lamago, H. Eckerlebe, and K. Pranzas, "Magnetic structure of MnSi under an applied field probed by polarized small-angle neutron scattering", *Phys. Rev. B,* **74**, 214414 (2006)

[31] Y. Ishikawa, G. Shirane, and J.A. Tarvin, "Magnetic excitations in the weak itinerant ferromagnet MnSi", *Phys. Rev. B,* **16**, 4956 (1977)

[32] C. Thessieu, C. Pfleiderer, A. N. Stepanov, and J. Flouquet, "Field dependence of the magnetic quantum phase transition in MnSi", *J. Phys.: Condens. Matter,* **9**, 6677 (1997)

[33] C. Pfleiderer, A. Neubauer, S. Mühlbauer, F. Jonietz, M. Janoschek, S. Legl, R. Ritz, W. Münzer, C. Franz, P. G. Niklowitz, T. Keller, R. Georgii, P. Böni, B. Binz, and A. Rosch, "Quantum order in the chiral magnet MnSi", J. *Phys.: Condens. Matter,* **21**, 164215 (2009)

[34] M. L. Plumer, and M. B. Walker, "Wavevector and spin reorientation in MnSi", *J. Phys. C: Solid State Phys*., **14**, 4689 (1981)

[35] K. Koyama, T. Goto, T. Kanomata, and R. Note, "Observation of an itinerant metamagnetic transition in MnSi under high pressure", *Phys. Rev. B* **62**, 986 (2000)

[36] P. A. Hansen, "Magnetic Anisotropy and Related Matters Studied by Neutron Diffraction", *Risø Report*, No. 360 (thesis) Risø National Laboratory, Gjellerup, Copenhagen (1977)

[37] P. Bak, and M. H. Jensen, "Theory of helical magnetic structures and phase transitions in MnSi and FeGe", *J. Phys. C: Solid State Phys.*, **13**, L881 (1980)

[38] S. V. Maleyev, "Cubic magnets with Dzyaloshinskii-Moriya interaction at low temperature", *Phys. Rev. B*, **73**, 174402 (2006)

[39] S. Demishev, A. Semeno, A. Bogach,V. Glushkov, N. Sluchanko, N. Samarin, and A. Chernobrovkin. "Is MnSi an Itinerant Electron Magnet? Results of ESR Experiments", *JETP Letters*, **93**, 213 (2011)

[40] S. V. Grigoriev, V. A. Dyadkin, E. V. Moskvin, D. Lamago,T. Wolf, H. Eckerlebe, and S. V. Maleyev, "Helical spin structure of $Mn_{1-y}Fe_ySi$ under a magnetic field: Small angle neutron diffraction study", *Phys. Rev. B,* **79**, 144417 (2009)

[41] C. Pfleiderer, S. R. Julian, and G. G. Lonzarich, "Non-Fermi-liquid nature of the normal state of itinerant-electron ferromagnets", *Nature*, **414**, 427 (2001)

[42] Y. J. Uemura, T. Goko, I. M. Gat-Malureanu, J. P. Carlo, P. L. Russo, A. T. Savici, A. Aczel, G. J. MacDougall, J. A. Rodriguez, G. M. Luke, S. R. Dunsiger, A. McCollam, J. Arai, C. Pfleiderer, P. Böni, and K. Yoshimura, "Phase separation and suppression of critical dynamics at quantum phase transitions of MnSi and (Sr1−xCax)RuO3", *Nat. Phys.,* **3**, 29 (2007)

[43] M.M.R. Evans, J.C. Glueckstein, and J. Nogami, "Epitaxial growth of manganese on silicon: Volmer-Weber growth on the Si (111) surface", *Phys. Rev. B* **53** 4000 (1996)

[44] S. M. Shivaprasad, C. Anandan, S. G. Azatyan, Y. L. Gavriljuk, and V. G. Lifshits, "The formation of Mn/Si (111) interface at room and high temperatures", *Surf. Sci.* **382** 258 (1997)

[45] T. Nagao, S. Ohuchi, Y. Matsuoka, and S. Hasegawa, "Morphology of ultrathin manganese silicide on Si (111)", *Surf. Sci.* **419** 134 (1999)

[46] Q. Zhang, M. Tanaka, M. Takeguchi, and K. Furuya, "Analytical UHV transmission electron microscopy studies of electronic structure changes between as-deposited Mn and Mn silicide on Si(111) surface", *Surf. Sci*. **507–510,** 453 (2002)

[47] A. Kumar, M. Tallarida, M. Hansmann, U. Starke, and K. Horn, "Thin manganese films on Si (111)-(7 × 7): electronic structure and strain in silicide formation", *J. Phys. D: Appl. Phys.* **37**, 1083 (2004)

[48] E. Magnano, E. Carleschi, A. Nicolaou, T. Pardini, M. Zangrando, and F. Parmigiani, "Growth of manganese silicide films by co-deposition of Mn and Si on Si(111): A spectroscopic and morphological investigation", *Surf. Sci*. **600**, 3932 (2006)

[49] J. Hirvonen Grytzelius, H. M. Zhang, and L. S. O. Johansson, "Surface electronic structure of Mn/Si(111) - $\sqrt{3}\times\sqrt{3}$ " , *Phys*. *Rev*. *B,* **78**, 155406 (2008)

[50] S. Higashi, Y. Ikedo, P. Kocan, and H. Tochihara, "Epitaxially grown flat MnSi ultrathin film on Si(111)", *Appl. Phys. Lett*. **93**, 013104 (2008)

[51] S. G. Azatyan, O.A. Utas, N.V. Denisov, A.V. Zotov, and A.A. Saranin, "Variable termination of MnSi/Si(111) $\sqrt{3}\times\sqrt{3}$ films and its effect on surface properties", *Surf. Sci.,* **605***,* 289, (2011)

[52] K. Schwinge, J. J. Paggel, and P. Fumagalli, "Mosaic superstructure in manganese silicide on Si (111)-($\sqrt{3}\times\sqrt{3}$): Bi-α", *Surf. Sci*. **601** 810 (2007)

[53] E. Magnano, F. Bondino, C. Cepek, F. Parmigiani, and M. C. Mozzati, "Ferromagnetic and ordered MnSi(111) epitaxial layers", *Appl. Phys. Lett*. **96**, 152503 (2010)

[54] A. B. Butenko, A. A. Leonov, U. K. Rößler, and A. N. Bogdanov, "Stabilization of skyrmion textures by uniaxial distortions in noncentrosymmetric cubic helimagnets", *Phys. Rev. B,* **82**, 052403 (2010)

[55] E. Weschke, H. Ott, E. Schierle, C. Schüßler-Langeheine, D. V. Vyalikh, G. Kaindl, V. Leiner, M. Ay, T. Schmitte, H. Zabel, and P. J. Jensen, "Finite-Size Effect on Magnetic Ordering Temperatures in Long-Period Antiferromagnets: Holmium Thin Films*", Phys. Rev. Lett*. **93**, 157204 (2004)

[56] S. Chikazumi, *Physics of Magnetism*, (John Wiley & Sons, New York, 1964)

[57] D. Sander, "The correlation between mechanical stress and magnetic anisotropy in ultrathin films", *Rep. Prog. Phys*. **62** 809 (1999)

[58] E. A. Karhu, U. K. Rößler, A. N. Bogdanov, S. Kahwaji, B. J. Kirby, H. Fritzsche, M. D. Robertson, C. F. Majkrzak, and T. L. Monchesky, "Chiral modulations and reorientation effects in MnSi thin films" (submitted to *Phys. Rev. B*, (2011))

[59] Y. C. Lian, and L. J. Chen, "Localized epitaxial growth of $MnSi_{1.7}$ on silicon", *Appl. Phys. Lett.* **48**, 359 (1986)

[60] G. Ctistis, U. Deffke, J.J. Paggel, and P. Fumagalli, "Growth and structural properties of Mn films on Si (111) – $\sqrt{3}\times\sqrt{3}$): Bi", *J. Magn. Magn. Mater.* **240,** 420 (2002)

[61] A. S. Arrott, Introduction to Reflection High Energy Electron Diffraction (RHEED). In J.A.C. Bland and B. Heinrich (Eds.) *Ultrathin Magnetic Structures* (Springer, Berlin, New York, 2005)

[62] B.D. Cullity, S.R. Stock, *Elements of X-ray Diffraction 3rd Edition*, (Prentice Hall, Upper Saddle River, New Jersey, 2001)

[63] A. Boulle, R. Guinebretière, and A. Dauger, "X-ray diffraction from epitaxial thin films: an analytical expression of the line profiles accounting for microstructure", *Z. Kristallogr. Suppl*., **23** 123 (2006)

[64] J. Daillant, and A. Gibaud, *X-ray and Neutron Reflectivity: Principles and Applications*, (Springer, New York 1999)

[65] E. Chason, and T. M. Mayer, "Thin Film and Surface Characterization by Specular X-Ray Reflectivity", *Critical Reviews in Solid State und Materials Sciences*, **22**(1), 1 (1997)

[66] Simulreflec: http://www-lb.cea.fr/prism/programs/simulreflec/simulreflec.html

[67] Predel, B.: *Mn-Si (Manganese-Silicon)*. Madelung, O. (ed.). Springer Materials - The Landolt-Börnstein Database (http://www.springermaterials.com).

[68] M. Eizenberg, and K. N. Tu, "Formation and Schottky behavior of manganese silicides on n-type silicon", *J. Appl. Phys.*, **53**, 6885 (1982)

[69] M. D. Robertson, M. Burns, and T. Morrison, "The Preparation of Semiconductor TEM Specimens by Low-Angle Polishing", *Micros. Soc. Can. Bull.*, **34**, 19 (2006)

[70] E. Karhu, S. Kahwaji, T. L. Monchesky, C. Parsons, M. D. Robertson, and C. Maunders, "Helical magnetic order in MnSi thin films", *Phys. Rev. B*, **82**, 184417 (2010)

[71] S. M. Stishov, A. E. Petrova, S. Khasanov, G. K. Panova, A. A. Shikov, J. C. Lashley, D. Wu, and T. A. Lograsso, "Experimental study of the magnetic phase transition in the MnSi itinerant helimagnet", *J. Exp. Theor. Phys.*, **106**, 888 (2008)

[72] H. Ogi, M. Fujii, N. Nakamura, T. Shagawa, and M. Hirao, "Resonance acoustic-phonon spectroscopy for studying elasticity of ultrathin films", *Appl. Phys. Lett.*, **90**, 191906 (2007)

[73] P. H. Dederichs, C. Lehmann, and A. Scholz, "Change of elastic constants due to interstitials", *Z. Phys*. *B*, **20**, 155 (1975).

[74] F. Huang, M. T. Kief, G. J. Mankey, and R. F. Willis, "Magnetism in the few-monolayers limit: A surface magneto-optic Kerr-effect study of the magnetic behavior of ultrathin films of Co, Ni, and Co-Ni alloys on Cu(100) and Cu(111)", *Phys. Rev. B*, **49**, 3962 (1994)

[75] R. Zhang, and R. F. Willis, "Thickness-Dependent Curie Temperatures of Ultrathin Magnetic Films: Effect of the Range of Spin-Spin Interactions", *Phys. Rev. Lett.*, **86**, 2665 (2001)

[76] J. S. Jiang, and C. L. Chien, "Magnetization and finite - size effects in Gd/W multilayers", *J. Appl. Phys.*, **79**, 5615 (1996)

[77] C. G. Duan, R. F. Sabiryanov, J. J. Liu, W. N. Mei, P. A. Dowben, and J. R. Hardy, "Strain Induced Half-Metal to Semiconductor Transition in GdN", *Phys. Rev. Lett.*, **94**, 237201 (2005)

[78] C. Pfleiderer, G. J. McMullan, S. R. Julian, and G. G. Lonzarich, "Magnetic quantum phase transition in MnSi under hydrostatic pressure", *Phys. Rev. B*, **55**, 8330 (1997)

[79] S. Yu. Dan'kov, A. M. Tishin, V. K. Pecharsky, and K. A. Gschneidner, Jr., "Magnetic phase transitions and the magnetothermal properties of gadolinium", *Phys. Rev. B*, **57**, 3478 (1998)

[80] K. Makoshi, and T. Moriya, "Theory of Helical Spin Structure in Itinerant Electron Systems. II"*, J. Phys. Soc. Jpn.*, **44,** 80 (1978)

[81] R. P. Erickson, and D. L. Mills, "Thermodynamics of thin ferromagnetic films in the presence of anisotropy and dipolar coupling", *Phys. Rev. B*, **44**, 11825 (1991)

[82] M. Ishida, Y. Endoh, S. Mitsuda, Y. Ishikawa, and M. Tanaka, "Crystal Chirality and Helicity of the Helical Spin Density Wave in MnSi. II. Polarized Neutron Diffraction", *J. Phys. Soc. Jpn.*, **54**, 2975 (1985)

[83] A. Sulpice, U. Gottlieb, M. Affronte, and O. Laborde, "Magnetic and electronic properties of Mn_4Si_7", *J. Magn. Magn. Mater.*, **272-276**, 519 (2004)

[84] G. P. Felcher, W. Lohstroh, H. Fritzsche, M. Münzenberg, H. Maletta, and W. Felsch, "Imprinting magnetic structures", *Appl. Phys. Lett.*, **72**, 2894 (1998)

[85] Reflpak reference P.A. Kienzle, K.V. O'Donovan, J.F. Ankner, N.F. Berk, and C.F. Majkrzak; http://www.ncnr.nist.gov/reflpak. 2000-2006

[86] S. V. Maleyev, "Magneto-elastic interaction in cubic helimagnets with B20 structure", *J. Phys.*: *Condens*. *Mat*., **21**, 146001 (2009)

[87] E. Fawcett, J. P. Maita, and J. H. Wernick, "Magnetoelastic and Thermal Properties of MnSi", *Int. J. Magn*., **1**, 29 (1970).

[88] E. Franus-Muir, M. L. Plumer, and E. Fawcett, "Magnetostriction in the spin-density-wave phase of MnSi", *J. Phys.C*, **17**, 1107 (1984).

[89] S. V. Grigoriev, S. V. Maleyev, V. A. Dyadkin, D. Menzel, J. Schoenes, and H. Eckerlebe, "Principal interactions in the magnetic system $Fe_{1-x}Co_xSi$: Magnetic structure and critical temperature by neutron diffraction and SQUID measurements", *Phys. Rev. B*, **76**, 092407 (2007).

[90] E. A. Karhu, S. Kahwaji, M. D. Robertson, H. Fritzsche, B. J. Kirby, C. F. Majkrzak, and T. L. Monchesky, "Helical magnetic order in MnSi thin films", *Phys. Rev. B*, **84**, 060404(R) (2011)

[91] Y. A. Izyumov, “ Modulated, or long-periodic, magnetic structures of crystals”, *Sov. Phys. Usp*., **27** 845 (1984)

[92] U. K. Rößler (private communication), (2011)

Appendix A1 – Demagnetizing Field

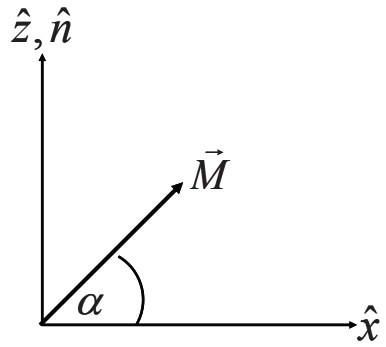

Figure A1.1. The magnetization, $\vec{M}$, with respect to angle.

For a thin film with a surface normal, $\hat{n}$, as shown in Fig. A1.1, the demagnetizing field is determined by,

$$\vec{H}_{\text{Demag}} = -\vec{M} \cdot \hat{n} = M_{\text{sat}} \sin(\alpha). \tag{A1.1}$$

The energy density of the demagnetizing field in the out-of-plane [111] direction is,

$$w_{\text{Demag}}^{[111]} = -\frac{\mu_0}{2} \vec{H}_{\text{Demag}} \cdot \vec{M} = \frac{\mu_0 M_{\text{sat}}^2}{2} \sin^2(\alpha). \tag{A1.2}$$

Appendix A2 - Magnetostatic Energy Calculation

For a helical magnet with a *Q*-vector oriented in the *x*-direction, as shown in Fig. A2.1, the magnetic surface charge on the top of the MnSi thin film is,

$$\sigma^{top} = M \cos(Qx)\cos(\alpha), \tag{A2.1}$$

and on the bottom of the film is,

$$\sigma^{bottom} = -M \cos(Qx)\cos(\alpha). \tag{A2.2}$$

.

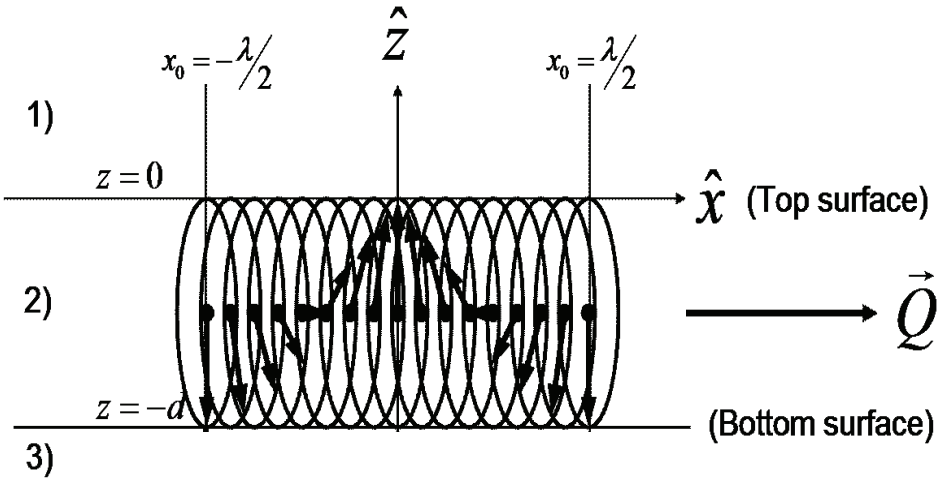

Figure A2.1. Diagram of the orientation of the magnetic moments in a MnSi thin film with $\vec{Q}$ oriented in the plane of the film.

The magnetic scalar potential $\phi(x,z)$ can be found for the top surface shown in Fig. A2.2 using a solution of the form,

$$\phi_1^{top}(x,z) = A_1 \cos(kx) e^{-kz}, \qquad (z>0), \tag{A2.3}$$

in region (1) and,

$$\phi_2^{top}(x,z) = A_2 \cos(kx) e^{+kz}, \qquad (z<0), \tag{A2.4}$$

in region (2). The boundary condition $\phi_1^{top}(z=0^+) = \phi_2^{top}(z=0^-)$, gives $A_1 = A_2$. The other boundary condition $H_1^{top} \cdot \hat{n}|_{z=0^+} - H_2^{top} \cdot \hat{n}|_{z=0^-} = \sigma^{top}$ gives,

$$kA_1 \cos(kx) + kA_2 \cos(kx) = M \cos(Qx)\cos(\alpha). \tag{A2.5}$$

From these boundary conditions, $k = Q$, and $A_1 = A_2 = A = \frac{M\cos(\alpha)}{2Q}$. The solution for region (1) is,

$$\phi_1^{top}(x,z) = \frac{M\cos(\alpha)}{2Q}\cos(Qx)e^{-Qz}, \qquad (z>0), \tag{A2.6}$$

and for region (2) is,

$$\phi_2^{top}(x,z) = \frac{M\cos(\alpha)}{2Q}\cos(Qx)e^{Qz}, \qquad (z<0). \tag{A2.7}$$

Similarly for the bottom surface,

$$\phi_2^{bottom}(x,z) = -\frac{M\cos(\alpha)}{2Q}\cos(Qx)e^{-Q(z+d)}, \qquad (z>-d). \tag{A2.8}$$

The total magnetic potential at the top surface z = 0 is therefore

$$\phi^{top}(x) = \frac{M\cos(\alpha)}{2Q}\cos(Qx)\left(1-e^{-Qd}\right). \tag{A2.9}$$

and on the bottom surface (z = -d)

$$\phi^{bottom}(x) = \frac{M\cos(\alpha)}{2Q}\cos(Qx)\left(e^{-Qd}-1\right). \tag{A2.10}$$

Combining Eq. A2.1, A2.2, A2.9 and A2.10 and the boundary conditions from Fig. A2.2, the magnetostatic energy density can then be found by integrating the surface integral. As α increases, the surface charges decrease as sin(α). Therefore, w_m becomes,

$$w_{\mathrm{m}} = \frac{\mu_0}{2}\oint \phi(x)\sigma(x)\,da\,\frac{1}{\lambda L_y d} \tag{A2.11}$$

$$= \frac{\mu_0}{2}\int_0^{L_y}\int_{-\frac{\lambda}{2}}^{\frac{\lambda}{2}} \left(\phi^{top}\sigma^{top} + \phi^{bottom}\sigma^{bottom}\right)\,dx\,dy\left[\frac{1}{\lambda L_y d}\right]$$

$$= \frac{\mu_0 M^2 \cos^2(\alpha)}{4Qd}\left(1-e^{-Qd}\right),$$

where L_{y} is an arbitrary length term in the *y*-direction. w_{m} can be expressed as an effective uniaxial anisotropy $K_{\mathrm{m}}\cos^2(\alpha)$, where,

$$K_m = \frac{\mu_0 M^2}{2Qd}\left(1-e^{-Qd}\right). \tag{A2.12}$$